Electron diffraction and controlled molecules

Dissertation

zur Erlangung des Doktorgrades
an der Fakultät für Mathematik, Informatik und Naturwissenschaften,
Fachbereich Physik
der Universität Hamburg

vorgelegt von

Nele Lotte Marie Müller

aus Saarbrücken

Hamburg
2016

Gutachter der Dissertation:	Prof. Dr. Jochen Küpper Prof. Dr. Henry N. Chapman
Zusammensetzung der Prüfungskommission:	Prof. Dr. Jochen Küpper Prof. Dr. Henry N. Chapman Prof. Dr. Daniela Pfannkuche Prof. Dr. Robin Santra Prof. Dr. Henning Moritz
Datum der Disputation:	14. Juli 2016
Vorsitzender des Prüfungsausschusses:	Prof. Dr. Daniela Pfannkuche
Vorsitzender des Promotionsausschusses:	Prof. Dr. Peter H. Hauschildt
Dekan der Fakultät für Mathematik, Informatik und Naturwissenschaften:	Prof. Dr. Heinrich Graener

Eidesstattliche Versicherung

Hiermit versichere ich an Eides statt, dass ich die Inanspruchnahme fremder Hilfen aufgeführt habe, sowie, dass ich die wörtlich oder inhaltlich aus anderen Quellen entnommenen Stellen als solche kenntlich gemacht habe. Weiterhin versichere ich an Eides statt, dass ich die Dissertation selbst verfasst und keine anderen als die angegebenen Hilfsmittel benutzt habe.

Nele Müller

Abstract

The incentive of this work is to investigate the structure and intrinsic dynamics of molecules in the gas-phase by coherent electron diffraction. Time-resolved electron diffraction allows for recording of structural changes on the atomic scale. Controlling the molecules' spatial orientation increases the amount of information that can be retrieved from electron diffraction patterns.
This thesis includes some basics of electron diffraction theory and the according simulations to predict diffraction patterns. The simulations were used to compare different molecules and to illustrate the advantage of spatially controlled molecules as samples.
A controlled-molecules setup that operated at a kHz repetition rate is presented. The gas-phase molecules were prepared in cold, supersonic beams and could be quantum state selected by means of electric deflection. These samples were strongly aligned by intense picosecond laser pulses and could be mixed-field oriented. It was shown how the selection of low-rotational-energy states enhanced both alignment and orientation.
Within this work a dc electron source was developed according to the requirements of diffraction experiments on samples of controlled molecules. The electron gun was able to produce a million of electrons per pulse with a pulse duration of tens of picoseconds. The focusing electrodes were arranged in a configuration similar to a velocity-map-imaging spectrometer for the photo-cathode. The spectrometer was used to characterize the electron pulse in combination with electron trajectory simulations. The signal-to-noise of the setup was examined and significantly improved for the planned electron diffraction experiments on controlled gas-phase molecules. Diffraction data from a thin polycrystalline aluminum sample was recorded to test the electron gun with regard to coherence and resolution. Electron diffraction off gaseous molecular and atomic samples from a non-supersonic gas nozzle was used to ensure agreement between diffraction simulations and experiments.
The final setup combined the electron gun and the controlled-molecules apparatus. Major steps were taken toward electron diffraction off controlled gas-phase molecules: The candidate molecule 2,5-diiodobenzonitrile was aligned. Its deflection allowed for improvement of background subtraction and for selection of low rotational quantum states. Spatial imaging in combination with electron impact ionization allowed for monitoring the spatial overlap between alignment laser and the electron beam. The remaining steps toward electron diffraction of state-selected and aligned molecules are discussed in the outlook of this thesis.

Zusammenfassung

Das Ziel dieser Arbeit ist es, molekulare Strukturen und Dynamiken in der Gasphase mithilfe von zeitaufgelöster Elektronenstreuung zu untersuchen. Der Informationsgehalt der Streubilder kann sich erhöhen, wenn die Moleküle im Raum orientiert werden.
Zu Beginn dieser Arbeit werden theoretische Grundlagen der Elektronenstreuung diskutiert. Darauf basierende Simulationen erlaubten die Vorhersage von Streubildern. Dabei wurden verschiedene Moleküle verglichen und die Vorteile räumlicher Ausrichtung verdeutlicht.
In der dann präsentierten Apparatur konnten Moleküle in Gasphase bei einer experimentellen Rate von 1 kHz kontrolliert werden. Durch Überschallexpansion gekühlte Molekülstrahlen wurden mithilfe elektrischer Felder abgelenkt, was die Selektion nach Quantenzuständen ermöglichte. Die Ausrichtung der Moleküle erfolgte durch einen intensiven Pikosekundenlaser und die Orientierung wurde mithilfe gemischter Feldern erreicht. Die Auswahl von Molekülen in niedrigen Rotationszuständen verbesserte den Grad der Ausrichtung und der Orientierung.
Die im Rahmen dieser Arbeit entwickelte Elektronenkanone war an die Anforderungen der Streuexperimente an kontrollierten Molekülen angepasst. Die Quelle erzeugte Pulse mit einer Million Elektronen bei einer Pulsdauer von mehreren zehn Pikosekunden. Die Fokussierelektroden der Kanone dienten zugleich als „Velocity-Map-Imaging“-Spektrometer für die von der Kathode emittierten Elektronen. Dieses wurde in Kombination mit Simulationen von Elektronentrajektorien genutzt, um den Aufbau zu charakterisieren. Das Signal-Rausch-Verhältnis wurde untersucht und deutlich verbessert. Streuexperimente an dünner Aluminium-Folie dienten als Test für Kohärenz und Auflösung. Darüber hinaus wurden die Elektronen an atomaren und molekularen Gasen gestreut, die aus einer nicht-supersonischen Quelle stammten. Damit konnte die Übereinstimmung von Streusimulationen mit Experimenten gezeigt werden.
Der finale Aufbau vereinte die Elektronenquelle mit der Molekülstrahlapparatur für kontrollierte Moleküle. 2,5-Diiodobenzonitril Moleküle wurden ausgerichtet. Ablenkung der Moleküle erleichterte einerseits den Hintergrundabzug und diente andererseits der Auswahl niedriger Rotationszustände. Unter Ausnutzung der räumlichen Abbildung von Ionen konnte der Überlapp zwischen Elektronenstrahl und Ausrichtungslaser überprüft werden. Die noch ausstehenden Schritte für Elektronenstreuung an kontrollierten Molekülen werden im Ausblick dieser Arbeit diskutiert.

Contents

1 Introduction

1.1 Learning from nature

A distinct capability of human kind is to study nature and reproduce its capabilities in a controlled way. This process might have started out with observing a bush fire, spark one for cooking until the elaborate control of combustion for todays energy production and transportation. Over the centuries, both, the observation and the control of nature, have evolved immensely. Today's challenges in resource management, climate change and health care demand that we develop our capabilities even further. One important step is to view nature not as a static, isolated system, but to include dynamic changes in a system's structure and understand details of complex systems. Only then is control and reproduction of nature's capabilities possible.
A corner stone of this understanding is the question how molecules undergo structural changes. This is the basis of dynamic processes as they a happen in plants, our body or the earth's atmosphere. The structure of a system defines its function. The effect of molecules in medication on our body is a prominent example. Different structural isomers can vary in their effect on the human body, for example concerning smell [1] or harmfulness [2]. This structure is not static, but changes dynamically. Hence, in order to understand functioning to the full, it is necessary to follow the dynamic process. An example would be the understanding of photo-synthesis. Plants and bacteria are capable of an amazing energy transfer efficiency of over 90%, which is far from the one realized in our energy power industry [3]. An essential step of its understanding is to unravel details in structure and dynamics of these systems, including effects of (de)coherence and environment [4].
The understanding of structural changes in complex systems can be reached by approaching it once from the side of complexity, e.g. directly working with biological samples and from the other side starting out with a well-controlled isolated system. This work focusses on the latter, where molecules in the gas-phase are studied to learn about their pure and fundamental properties without environment or restrictive surroundings. The isomerization of stilbene upon illumination by UV light is an example for such fundamental type of dynamics (Figure 1.1). Each electronic state of the molecule possesses a potential energy surface, which can exhibit different (local) energetic minima. The goal is to study in detail along which pathways on the corrugated potential energy surface the molecule changes from one isomer structure to another one. Having a fundamental comprehension of such a dynamic process can allow the identification of relevant stages in functioning of molecules

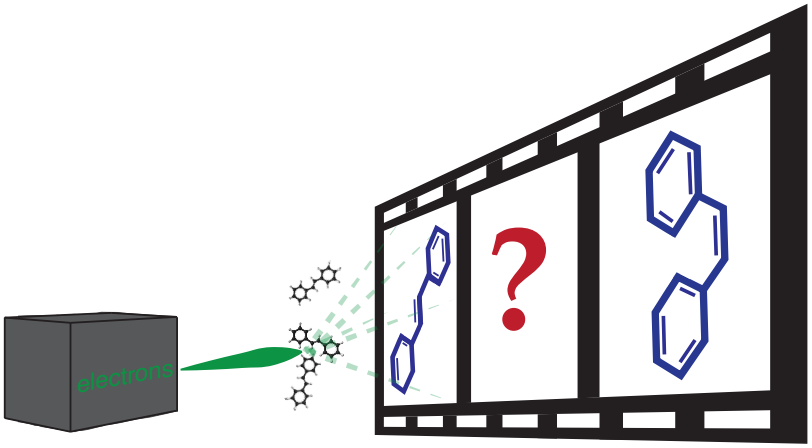

Figure 1.1: Illustration of the molecular movie. Electron diffraction is used to study the isomerization of stilbene in a time-resolved way.

and materials. After imaging the dynamics, the next step is to understand how these changes can be controlled with external parameters. In the end we have to combine the treatment of complex systems that biologists and chemists are capable of, with the fundamental understanding of quantum mechanics and quantum control during structural dynamics that physicists and physical chemists bring along.
Studying structural dynamics on the molecular and atomic level demands special imaging techniques that are capable of resolving tiny structures on the scale of Ångström (10^{-10} m) that change their configuration on an ultrashort time scale. Typical timescales are attoseconds (10^{-18} s) to femtoseconds (10^{-15} s) for electrons, femtoseconds to picoseconds (10^{-12} s) for nuclei up to milliseconds (10^{-3} s) for larger systems. For the investigation of dynamics these structures and their changes need to be controlled. To record a so-called molecular movie in a pump-probe scheme, the system has to prepared in a well-defined state and dynamics have to be triggered in a controlled way.

1.2 Imaging nature by diffraction experiments

Imaging structural dynamics of molecules means to be able to follow nuclei and electron distributions as they change their configuration with time. Since the 17th century, conventional light microscopy has proven to reveal the structures of cells and bacteria with huge impact on our understanding of life. But microscopy is limited in resolution by the wavelength employed (Abbe limit), although recent developments started to breach this barrier [5]. Electron microscopy [6] allows to resolve atomic structure in a lab-scale apparatus, as electron energies of tens of keV, which are regulary employed in electron sources, already generate electrons with wavelengths on the order of Ångström. Over the last decades many more imaging approaches have been developed. Spectroscopy over a

large variety of wavelengths was employed for structure determination [7, 8]. Since the development of short-pulsed lasers, temporal resolution on the order of 10^{-15} s can be achieved by laser-based imaging techniques. In combination with transmission electron microscopes this can allow for investigation of ultrafast dynamics [9]. Furthermore, lasers can be used to ionize the molecule and retrieve information from the ionized fragments and photo-electrons [10–13]. Moreover, laser-based sources producing ultrashort pulses of x-rays or electrons allow for diffractive imaging with spatial resolution on the order of Ångström and time-resolutions of tens of femtoseconds. These properties enable the recording of so-called molecular movies, which trace the structural dynamics at the atomic level.

Static Bragg diffraction is a well established tool for the investigation of solid state samples using electrons [14] or x-rays [15, 16]. Electron diffraction together with quantum chemistry has furthermore been widely used for gas-phase structure-determination in chemistry [17]. For the last two decades many developments have focused on time-resolved experiments [18–23]. X-ray and electron diffraction serve as complementary approaches. X-ray radiation interacts with the electrons in the molecule, which experience a quiver motion due to the instantaneous electric field of the x-ray pulse. In contrast, the electron scattering is sensitive to both, the nuclei and to the electrons within the molecule, as Coulomb forces determine the interaction. Cross sections are significantly larger for electrons, but the number of electrons per probe pulse is limited by Coulomb repulsion between the electrons. The Coulomb interaction also limits the time-resolution and coherence that is achievable with bright electron sources. Electron diffraction exhibits a smaller cross section in inelastic scattering and hence unwanted damage of molecules [24]. X-ray sources for diffraction experiments require large scale facilities or techniques as laser-driven plasma sources [25]. Electron guns can be set-up as table-top experiments. Recently, larger electron source facilities have been developed to use relativistic electrons [26, 27], while many groups focus on reducing the size of x-ray sources [28]. The named differences show that both approaches have advantages and disadvantages when studying molecules. The choice in source depends on the system that is studied and the desired observables. The low density of gas-phase samples requires sources of large-cross-section particles or photon pulses with large brightness, while still ensuring atomic resolution. As electron sources can meet these requirements even in table-top setups, electron diffraction was chosen as imaging tool for this work.

When molecules are imaged by diffraction, the recorded pattern is a 2D-projection of the probability density of the outgoing wave. The phase information and hence information on the 3D structure of the molecule is not recorded in conventional diffraction. Information on the 3D-structure can be achieved by phase-retrieval algorithms, which was shown for single particle imaging or in crystals [29, 30]. Recently, it has been proven, that using the incoherent sum of scattering due to imperfections in crystals, one can retrieve the information on the 3D-structure of macromolecules without prior theoretical knowledge of the molecule [31].

Many molecules cannot be crystallized or it is desired to study them without the boundary

conditions of a solid-state structure. For an ensemble of gas-phase molecules retrieval of phase and hence of 3D-structure is possible, if the molecule's orientation can be controlled to allow for holographic and tomographic methods. The retrieval of information on the 3D structure of molecules by diffraction imaging of an aligned ensemble was proposed theoretically [23, 32–35] and was demonstrated experimentally for x-ray [36, 37] as well as for electron diffraction [38, 39].

1.3 Controlling nature at the quantum level

Within a gas-phase sample of molecules, many different quantum states and structural conformers can be populated and different cluster sizes can occur. Moreover, molecules in field-free space have no preferred orientation, but are isotropically distributed. Imaging an ensemble of molecules, for example by diffraction, would result in an averaged image of various states and orientations. One possibility to avoid this loss of information due to averaging is imaging of single particles, if enough signal can be achieved [23, 29]. Considering the currently available source brightness and the molecular cross sections, the achieved signal strengths are too low to image single small molecules and even large ones are difficult, for now. In order to enhance the information that can be gathered from an ensemble of molecules a well-defined state or structure can be selected by electrostatic deflection and the spatial orientation can be controlled, too. Both methods allow to control the molecules on a quantum level enabled by short-pulsed, intense lasers and electric field design.

Similar to the work by Otto Stern [40], a method was developed to separate molecules according to their quantum state [41–43], shape [44–46] and size [47]. Molecules that exhibit a dipole moment are deflected in strong inhomogeneous electric fields. The force originates from the Stark effect and depends on the applied field gradient, on the molecular mass and the effective dipole moment. Similar to light of different wavelengths that passes a prism, the molecules separate according to their dipole-moment-to-mass ratio. The spatial separation yields the possibility to select molecules and hence generate pure samples for imaging experiments [48].

In alignment and orientation of molecules, the molecular frame is fixed to the laboratory's coordinate system. This allows for the retrieval of 3D information about the molecule by diffractive imaging as discussed in section 1.2. Alignment or orientation can be achieved by strong-field laser alignment and mixed-field orientation [49–53]. A strong degree of alignment, which is advantageous for 3D-structure reconstruction, is achieved for molecular samples with low rotational temperature (around 1 K) [54]. Such molecular samples are provided in cold supersonic molecular beams. Then, state-selection further allows for the investigation of samples in low rotational energy states or for small molecules even in the rotational ground state [41, 42].

1.4 Outline of this thesis

The main milestones of this project were, firstly, to control the molecules, secondly, to design and build a suited electron gun, which produced high numbers of electrons without loosing essential properties like coherence. Finally, the task was to combine the electron gun with the controlled molecules setup, ensuring the necessary signal-to-noise level from the dilute sample.

In chapter 2 the theory of gas-phase electron diffraction is discussed and electron diffraction simulations are described. From various possible models, the Mott-formula in first Born approximation with the independent atom model were used for the computational implementation. Simulations allowed to identify the candidate molecule 2,5-diiodobenzonitrile for diffraction experiments. The corresponding signal-to-noise estimations were used to predict necessary experimental parameters like electron number per pulse, measurement time and limitations by background gas. The simulations also illustrated how the contrast of diffraction patterns would be increased for aligned molecules. Not only did the simulations provide insight into necessary experimental parameters, but they were also used for the analysis of diffraction data obtained from the experiment.

Molecular control and its experimental realization is discussed in chapter 3. From a cold beam of molecules, samples of pure quantum state were generated. Separating the different states in space by electrostatic deflection allowed for state selection. The molecules in low rotational energy states were ideal candidates for spatial control through laser-alignment and mixed-field orientation. The first section describes the concepts of generating and imaging samples of controlled molecules, while the second section presents the according experiments. The apparatus produced these sample of state-selected and strongly aligned molecules at kHz-repetition rates, which was highly advantageous for electron diffraction experiments on dilute samples by increasing the statistics in comparison to former controlled molecules setups.

From diffraction simulations and the known experimental parameters of the controlled molecules apparatus, requirements for the electron source were deduced. The development of the according dc electron source is presented in chapter 4. It starts with the generation of ultrashort electron pulses and their properties. Some preliminary tests are discussed that dealt with the generation of high electron numbers from metal cathodes. Then, the electron gun's final setup is described. Its characterization was performed in comparison of measurements with particle trajectory simulations. The electron pulses were examined concerning their electron numbers, beam sizes, coherence, and pulse duration. In perspective of the electron diffraction experiments on dilute samples of controlled molecules the experimental background was minimized.

The steps that were undertaken for the combination of electron diffraction with controlled molecules are presented in chapter 5. The design implemented the developed electron source with the controlled molecules apparatus and included characterization and overlap tools. Diffraction experiments were performed on atomic and isotropic molecular gases from a test gas nozzle. The experimental data was compared with simulations of chapter 2

to allow for the bond length determination of the molecule sulfur-hexafluoride. As a first sample of controlled molecules, 2,5-diiodobenzonitrile was deflected and aligned. The spatial overlap between electron beam, molecular beam and laser was monitored with the aid of electron impact ionization. First diffraction data was recorded, but had not exceeded noise level, yet.
In chapter 6 the possible continuation of the presented experiments is elaborated, which leads to electron diffraction experiment on controlled molecules. The chapter includes further consideration of possible setup improvements and adaptations of simulation models. In the end an outlook on time-resolved experiments is provided.

2 Calculation of electron diffraction patterns for controlled gas-phase molecules

Electron diffraction serves as a tool for structure determination of molecules in the gas-phase. This chapter starts with the basic theory of electron diffraction and continues with an elaboration of how electron diffraction patterns are calculated within this thesis. The theory is implemented in a simulation code, which is then used to calculate diffraction patterns for prototypical gas-phase molecules. The last section considers background by atomic scattering, alignment of molecules and experimental parameters like overlap. These simulations serve as the foundation for feasibility tests and analysis of experiments in chapter 5.

2.1 Theoretical concepts of gas-phase electron diffraction

When an electron approaches a molecule, Coulomb forces determine the interaction. Electrons scatter off charge densities (electrons and nuclei) within the molecule. In one case, the electron will not loose energy but only change the direction of its momentum. This is called elastic scattering. In the other case, the electron energy is changed during the scattering process as the electron excites the molecule. The process is then called inelastic scattering.
Describing the electrons in the wave picture, formulas for the resulting intensities can be deduced. The coherently overlapped scattered waves from different atoms within the molecule interfere and the resulting diffraction pattern can be recorded. The intensity distribution encodes the molecular structure, if experimental conditions such as distance from scattering point to detector and electron energy are well-defined. Thus, it is possible to retrieve information on the molecular structure by analyzing the angular distribution of an electron diffraction pattern as described in the following.

2.1.1 Electron scattering off a rigid molecule

This section summarizes a theoretical description of electron diffraction based on the treatment in references 17 and 55, where more details can be found. The incoming

electrons are described by a plane wave traveling in z-direction

$$\Psi_0 = ae^{ik_0 z} \tag{2.1}$$

with a normalizing factor a, the absolute value of the wave vector $k_0 = 2\pi/\lambda$ and wavelength λ. Including relativistic effects, the De-Broglie-wavelength is given as

$$\lambda = \frac{h}{\sqrt{2m_e eU}\sqrt{1 + eU/2m_e c^2}} \tag{2.2}$$

with the kinetic energy $E = eU$, the electron charge e, the applied acceleration voltage U, the electron mass m_e, and the Planck constant h. The plane wave approach assumes the electron beam to be infinite in extent in both space and time. For a more realistic treatment, the incoming electrons would be treated as wave packet [56, 57]. The plane wave approach taken here is reasonable for the dimension of the wave packet being much larger than the size of the scatterer. For the deduction used here, the electron wave packet was assumed to be much larger than the screened Coulomb potential of a neutral atom or molecule [57].
In order to calculate the molecular diffraction pattern, the molecule is treated in the independent atom model. The scattering potential of each atom is first calculated assuming a spherical potential. With these assumptions the electron that is elastically scattered off one atom A_n emerges as a spherical wave. One can write the amplitude of the wave scattered by the atom as

$$\Psi'_n = Ka\frac{e^{ik_0 R}}{R} f_n(\vartheta)\, e^{i(\mathbf{k_0}-\mathbf{k'})\mathbf{r_n}} \tag{2.3}$$

with the constant $K = 8\pi^2 m_e e^2/h^2$, the distance between scattering center and observation point R, the atomic position vector $\mathbf{r_n}$, the scattered wave vector $\mathbf{k'}$ and the scattering angle ϑ with respect to z. The so-called scattering amplitude $f_n(\vartheta)$ depends on the interaction potential, so on the specific atom the electron scatters off. For scattering off a molecule a coherent sum is formed over all N atoms in the molecule:

$$\Psi' = \sum_{n=1}^{N} \Psi'_n \tag{2.4}$$

The independent atom model approach does not include effects of chemical binding on the electron density distribution.
The scattering intensity can be calculated from the electron current density

$$\mathbf{j} = \frac{he}{4\pi m_e i}(\Psi_n^* \nabla \Psi_n - \Psi_n \nabla \Psi_n^*) \tag{2.5}$$

of the incoming ($\mathbf{j}_0$) and the scattered ($\mathbf{j'}$) electrons [58]:

$$\mathbf{I} = I_0\,(\mathbf{j'}/\mathbf{j}_0) \tag{2.6}$$

Disregarding multiple scattering the resulting intensity is calculated from equation 2.6 to be

$$I(s) = \frac{K^2 I_0}{R^2} \sum_{n=1}^{N} \sum_{m=1}^{N} f_n(s) f_m^*(s) e^{i\mathbf{s}\mathbf{r}_{nm}} \tag{2.7}$$

with the distance $\mathbf{r}_{nm} = \mathbf{r}_n - \mathbf{r}_m$ between two atoms A_n and A_m. Here it was used that the distance between atoms $r_{nm} \ll R$. The scattering intensity is given as a function of the absolute value of the difference of wave-vectors,

$$|\mathbf{s}| = |\mathbf{k_0} - \mathbf{k}'| = 2k_0 \sin(\vartheta/2) = \frac{4\pi}{\lambda} \sin(\vartheta/2). \tag{2.8}$$

The definition of s varies in the literature. Often $s_x = \frac{1}{\lambda}\sin(\vartheta_x)$ with $\vartheta/2 = \vartheta_x$ is used in x-ray diffraction and also in some electron diffraction literature.
The intensity can be split in scattering off individual atoms, denoted as atomic scattering intensity I_a which does not depend on the interatomic distances, and interference terms between two atoms, denoted as molecular scattering intensity I_m:

$$I(s) = I_a(s) + I_m(s) \tag{2.9}$$

$$I_a(s) = \frac{K^2 I_0}{R^2} \sum_{n=1}^{N} |f_n(s)|^2 \tag{2.10}$$

$$I_m(s) = \frac{K^2 I_0}{R^2} \sum_{n=1}^{N} \sum_{\substack{m=1 \\ m\neq n}}^{N} f_n(s) f_m^*(s) e^{i\mathbf{s}\mathbf{r}_{nm}} \tag{2.11}$$

The so-called scattering cross section of an atom $(I_a/I_0)R^2$ is an essential quantity for electron diffraction experiments, as it quantifies the probability of an electron being scattered off an atom.
$I_m(s)$ is the molecular elastic electron scattering intensity of a rigid molecule with one fixed spatial orientation. In usual gas phase experiments the spatial orientation of the molecules is isotropic. Then the integral over the different orientations can be calculated and the molecular intensity becomes

$$I_m(s) = \frac{K^2 I_0}{R^2} \sum_{n=1}^{N} \sum_{\substack{m=1 \\ m\neq n}}^{N} f_n(s) f_m^*(s) \frac{\sin(s r_{nm})}{s r_{nm}} \tag{2.12}$$

Within this work diffraction patterns were calculated for isotropic and for aligned samples of molecules. In the case of the latter equation 2.12 is not applicable.
The information of the molecular structure is encoded in $I_m(s)$. In order to calculate the scattering intensities various models for $f_n(s)$ can be used. Starting from very crude approximations using Z/s^2 as scattering factor

$$I_m = \frac{K^2 I_0}{R^2} \sum_{n=1}^{N} \sum_{\substack{m=1 \\ m\neq n}}^{N} \frac{Z_n Z_m}{s^4} e^{i\mathbf{s}\mathbf{r}_{nm}}, \tag{2.13}$$

which corresponds to the Z dependence in Rutherford scattering.
In first Born approximation, the Mott formula

$$I_m = \frac{K^2 I_0}{R^2} \sum_{n=1}^{N} \sum_{\substack{m=1 \\ m \neq n}}^{N} \frac{Z_n - F_n(s)}{s^2} \frac{Z_m - F_m(s)}{s^2} e^{i\mathbf{s}\mathbf{r}_{nm}} \tag{2.14}$$

can be used to calculate the scattering amplitudes. It includes scattering from the nuclei and deduces the scattering of electrons from the x-ray scattering amplitudes $F_n(s)$. Here the atomic scattering factors are real and include no phase-dependence. This approximation is only valid for small Z and high energies [57]. Otherwise phase-shifts have to be included. A more accurate description employs complex atomic scattering amplitudes provided by the partial waves method:

$$I_m = \frac{K^2 I_0}{R^2} \sum_{n=1}^{N} \sum_{\substack{m=1 \\ m \neq n}}^{N} |f_n(s)||f_m(s)| \cos\Big(\eta_n(s) - \eta_m(s)\Big) e^{i(\mathbf{s}\mathbf{r}_{nm})} \tag{2.15}$$

Different atoms create different phase shifts. The effects due to phase shifts become more important with increasing differences in atomic numbers. Calculations using the Born approximation without phase-shifts were, for example, not able to reproduce diffraction data of uranium hexafluoride [59]. For all models, the electron scattering amplitudes quickly drop with increasing s. In the course of this work equation 2.14 was employed as this approach allows for a parametrization of the scattering amplitudes $f_m(s)$, which facilitates simulations of diffractions patterns.
For comparison with the total intensity retrieved in the experiment, inelastic scattering also has to be considered. Within the examined s-regime inelastic scattering is on the same order of magnitude as elastic scattering and its relative contribution to the total scattering increases with decreasing s. The inelastic scattering of an atom S_n is usually added to the part of the scattering intensity that does not depend on the interatomic distances, the incoherent part [17]. This is an approximation as coherent effects of inelastic scattering could appear, if the energy loss of inelastically scattered waves are the same and if they scatter off the same object state [60, 61]. Including S_n as incoherent, the background intensity is given by the sum of atomic and inelastic scattering:

$$I_b(s) = \frac{K^2 I_0}{R^2} \sum_{n=1}^{N} (|f_n(s)|^2 + S_n) \tag{2.16}$$

The inelastic scattering factors S_n can be calculated from the corresponding atomic x-ray inelastic scattering factors S_x by

$$S_n = \frac{4 S_x}{a_0^2 s^4} \tag{2.17}$$

where a_0 is the Bohr radius.
There are limitations to the theory that was used for the simulations presented below. The first Born approximation that was used to calculate the atomic scattering amplitudes,

becomes less appropriate with higher Z and low electron energies [57, 62]. As an example, the inaccuracy for the bond length determination of uranium hexafluoride amounts to 7% [63]. The above derivation of the scattering factors is not time-dependent. For a full treatment one would have to consider the electrons as wave packet and include internal motions of the molecule [17, 55]. Moreover, the independent atom model was used, which only approximates the structure of the molecule. Chemical binding effects would need to be included for a more accurate description. For the calculations of the inelastic scattering, a simple model was used, in which the inelastic scattering did not depend on the energy of the electrons. Relativistic effects were not included in the calculation of inelastic scattering factors, which could be important for the small s regime ($s < 3 \cdot 10^{10}/\,\mathrm{m}$) [64]. For 40 keV electrons the total relativistic effects due to coulombic electron-electron correlation can amount to upwards of 15% of the nonrelativistic results [64, 65]. In order take into account a transformation between the lab frame and the center-of-mass system the Bethe modification could be used [66]. In summary, the employed modeling decreases in quality for small s and large Z and it only includes a static picture of the molecule. Depending on the electron energy and the atoms within the molecule the inaccuracy level is expected to range from a few % to over 10%.

2.2 Computational implementation

In order to predict experimental diffraction patterns and also to analyze the recorded scattering data, a code was developed within the Controlled Molecule Imaging group for the simulation of x-ray and electron diffraction patterns. The program, called CMIdiffract, allows for the calculation of diffraction patterns of single atoms, molecules and ensembles of molecules. For a certain degree of spatial alignment (chapter 3) a distribution of the molecules' orientation within an ensemble is determined. The code adds the individual diffraction patterns for all the molecules according to this distribution. The code was originally developed for x-ray diffraction [36, 37, 67] and has been extended to electrons within this thesis as described in the following. The employed formulas and parts of the code are provided to illustrate their implementation into CMIdiffract.
The atomic scattering amplitudes were determined according to equation 2.14 as

$$f_n(s) = \frac{Z_n - F_n(s)}{s^2}, \tag{2.18}$$

where $F_n(s)$ are the x-ray scattering amplitudes. $f_n(s)$ was approximated by a sum of G Gaussians [68]:

$$f_n(s_x) = \sum_{g=1}^{G} a_g e^{-b_g s_x^2} \tag{2.19}$$

This allowed for a parametrization of $f_n(s_x)$ for values of $s_x < 2 \cdot 10^{10}/\mathrm{m}$ (or $s < 8\pi \cdot 10^{10}/\mathrm{m}$) using tables for a_m and b_m [68], where s_x was in units of $10^{10}/\mathrm{m}$. The electron scattering

amplitudes were then used to calculate the sum over all the atoms within the molecule.

$$I(s) = I_a(s) + I_m(s) = \frac{K^2 I_0}{R^2}\Big(\sum_{n=1}^{N} |f_n(s)|^2 + \sum_{n=1}^{N}\sum_{\substack{m=1 \\ m\neq n}}^{N} f_n(s) f_m^*(s) e^{i\mathbf{s}\mathbf{r}_{nm}}\Big) \tag{2.20}$$

```
for i in range(n_atoms):      # sum over all atoms in the molecule
  for idx in range(5):
        fi = fi + 1e-10*data_ab[idx+2+(self.atomic_number[i])*12]
    *np.exp(-data_ab[idx+7+(self.atomic_number[i])*12]
    *(self.s/(4*np.pi*1e10))**2)
  # calculation of scattering factor of i th atom in SI
  for j in range(n_atoms):
    for idx in range(5):
      fj = fj + 1e-10*data_ab[idx+2+(self.atomic_number[j])*12]
      *np.exp(-data_ab[idx+7+(self.atomic_number[j])*12]
      *(self.s/(4*np.pi*1e10))**2)
    # calculation of scattering factor of j th atom in SI
```

If the simulated ensemble was isotropic the calculation was simplified by equation 2.12. In this case no summation over the individual diffraction patterns was necessary.

```
fifj=fi*fj
if i == j:
  atomic = atomic + fifj
  # atomic scattering intensity without constant
else:
  rij = np.linalg.norm(r[i]-r[j])
  molecular = molecular+ fifj*(np.sin(self.s*rij)/(self.s*rij))
  # molecular scattering intensity
  # without constant in isotropic case
```

For an aligned sample the diffraction patterns of each molecule were summed up incoherently. In first Born approximation and using spherical scattering potentials, the $f_n(s)$ are real [56] and, therefore, $I_m(s)$ can be written as:

$$I_m(s) = \frac{K^2 I_0}{R^2}\Big(\sum_{n=1}^{N}\sum_{\substack{m=1 \\ n\neq m}}^{N} f_n(s) f_m(s) \cos[\mathbf{s}\mathbf{r}_{nm}]\Big) \tag{2.21}$$

```
molecular = molecular + fifj*np.cos(self.qx*(r[i,0]-r[j,0]) +
self.qy*(r[i,1]-r[j,1]) +self.qz*(r[i,2]-r[j,2]))
# molecular scattering intensity in general case
```

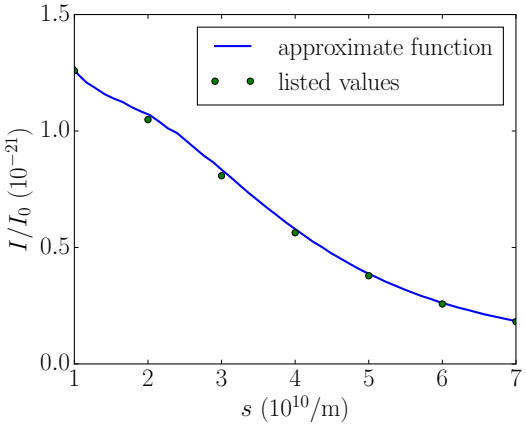

Figure 2.1: The radial sum of the normalized intensity I/I_0 for argon is compared for listed values and for an approximate function. See text for details.

Moreover, in contrast to the approach in [67], inelastic scattering has been implemented according to equation 2.17. S_x was obtained from tabulated values [69]. A logistic function

$$S_x(s) = a\frac{1}{1 + d \cdot e^{-b(s \cdot f + c)}} + e \tag{2.22}$$

with adapted parameters (a, b, c, d, e, f) for the individual atoms was used to approximate the provided values. This approach was only valid for the restricted s-regime that was typically reached in the diffraction experiments performed within the framework of this thesis. The S_x values from the table [69] and the corresponding values obtained from the function in the code are compared in Figure 2.1. The scattering intensity for argon was calculated using both approaches and plotted as radial sum as a function of s. The agreement was sufficient and the approximate function was used throughout this thesis.

```
def func(x,a,b,c,d,e,f): #parametrized logistic function
  return a*1/(1+d*np.exp(-b*(x*f+c)))+e
# read in Si (inelastic scattering factor for x-rays)
# and adapt for different s definition
Si = func(self.s,data_inel[self.atomic_number[i]-1,1],
data_inel[self.atomic_number[i]-1,2],
data_inel[self.atomic_number[i]-1,3],
data_inel[self.atomic_number[i]-1,4],
data_inel[self.atomic_number[i]-1,5],
data_inel[self.atomic_number[i]-1,6]/(4*np.pi))
for i in range(n_atoms):      # sum over all atoms in the molecule
  for j in range(n_atoms):
    if i == j:
      inelastic = inelastic+(4*Si/(a0**2*self.s**4))
```

The resulting background scattering intensity was then calculated by equation 2.16. For simulation of the total intensity on the detector the solid angle for the detector pixels and the distance to the detector were taken into account.

```
total = (molecular + atomic+inelastic)*const.K**2/self.z**2
#total scattering intensity with Hargittai constant
self.intensity = (total * solid_angle* photons *
molbeam_density* molbeam_width * self.z**2)
# Calculate intensity on detector per pixel with
# number of electrons, molecular beam density and width
```

In electron diffraction, it is convenient to provide the so-called modified scattering intensity instead of the total intensity in order to compensate for the steep decrease of the total intensity with s. Theoretically, the modified scattering intensity is

$$M(s) = \frac{I_m(s)}{I_a(s)} \tag{2.23}$$

or

$$sM(s) = s\frac{I_m(s)}{I_a(s)} \tag{2.24}$$

In comparison to experiments, I_b from equation 2.16 was usually considered instead of I_a, as atomic and inelastic scattering cannot be distinguished in the experiment:

$$sM(s) = s\frac{I_{\text{total}}(s) - I_b(s)}{I_b(s)} \tag{2.25}$$

The modified scattering intensity oscillates around the zero-line, as shown in Figure 2.2 d. It is used as starting point for structure determination, for example the reconstruction of nuclei distances within the molecule. In order to examine the feasibility of diffraction experiments and analyze the recorded data for structure determination the presented code was used to calculate diffraction patterns of prototypical atoms and molecules. The information that is gained from diffraction patterns can be enhanced by controlling the molecules' orientation in space as described in the following section.

2.3 Simulations for prototypical molecules

Simulations of electron diffraction patterns were used for the determination of feasible experiments, including the choice of molecular samples. The total scattering intensity was provided by simulation, which corresponded to the measured intensity in the experiment. This included experimental settings as distance from the interaction point to the detector (180 mm), the detector size (diameter $\approx$ 42 mm) and the according solid angle per pixel. The electron energies 15 keV ($\lambda \approx 10$ pm and $s < 7 \cdot 10^{10}$/m on detector) and 25 keV ($\lambda \approx 7.8$ pm and $s < 9 \cdot 10^{10}$/m on detector) were chosen in correspondence to the respective

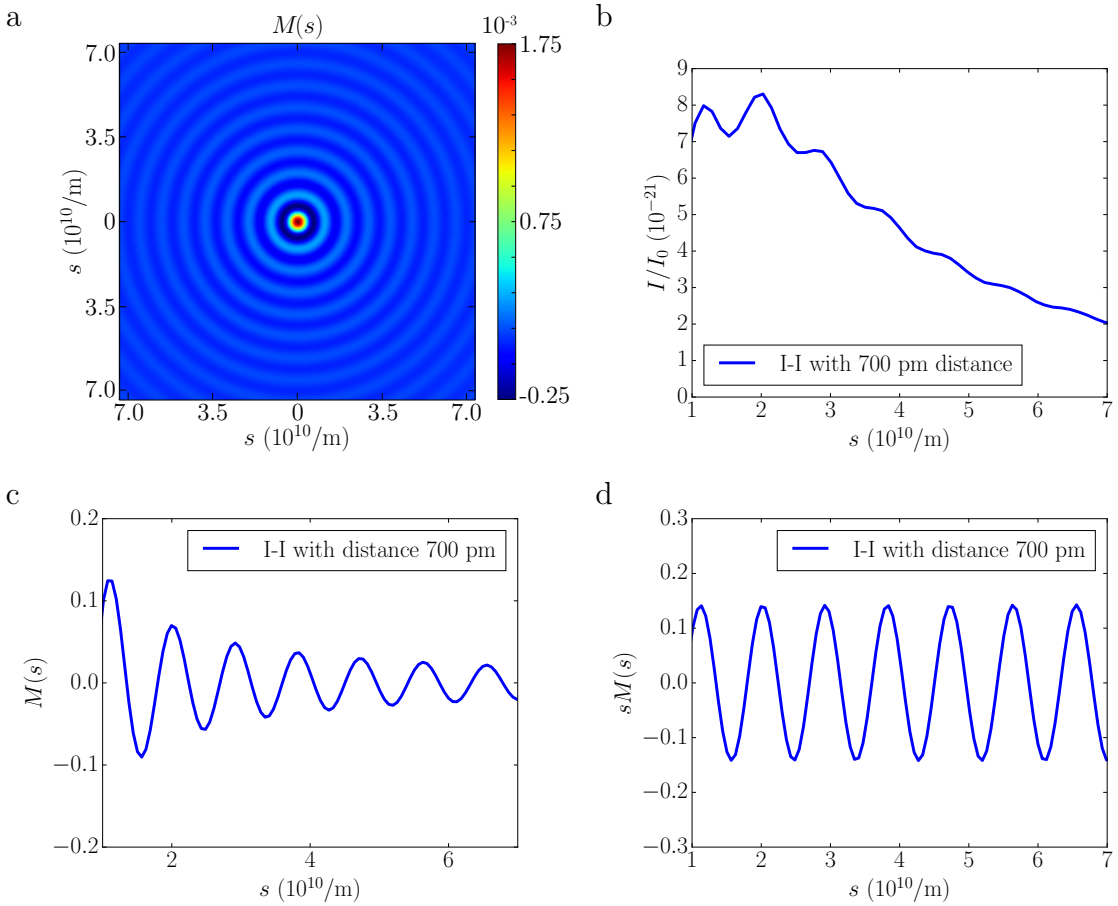

Figure 2.2: The electron diffraction signal off two iodine atoms with a distance of 700 pm is plotted as modified scattering intensity on the detector (a), radial plot of the total scattering intensity (b) and the modified scattering intensity (c). The modified scattering intensity can be multiplied by s to achieve a convenient radial plot oscillating around the zero-line (d).

experiments in chapter 5. The modified scattering intensity, from which the molecular structure can be deduced, was extracted from the simulations as well.

The comparatively low density of controlled-molecule samples (chapter 3) poses a signal-to-noise challenge to diffraction experiments. In first benchmark experiments molecules with large molecular scattering intensities $I_m(s)$ are preferred in order to compensate for the low sample density. As the scattering amplitude increases with the atomic number Z (equation 2.13), molecules containing heavy atoms are favorable. In the following the simulated electron diffraction patterns for several atomic and molecular examples are given.

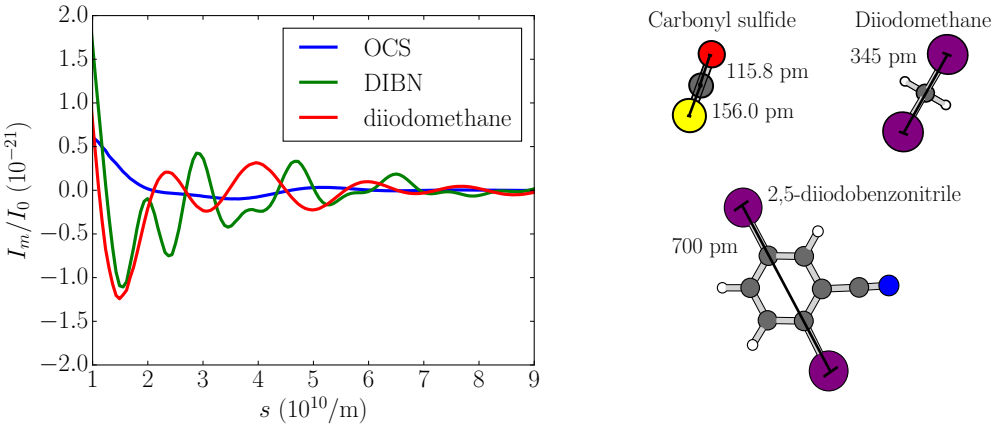

Figure 2.3: The molecular scattering intensity is shown in comparison for carbonyl sulfide, diiodomethane and 2,5- diiodobenzonitrile. The molecular structures and some relevant bond lengths are depicted

2.3.1 Choice of sample molecule

Iodine, with atomic number $Z = 53$, has a high scattering cross section and is a common as well as chemically convenient substituent in molecules. For illustration of a simple diffraction pattern, the scattering simulation for two iodine atoms with a distance of 700 pm is depicted in Figure 2.2. The distance is the same as the two iodine atoms have in 2,5-diiodobenzonitrile, which is discussed below as a candidate for diffraction experiments. The image in Figure 2.2 a shows the modified scattering intensity $M(s)$ for a typical s-regime achieved in the experiments within this thesis. The total intensity per incoming intensity, I/I_0, is given as radial sum[1] plotted in Figure 2.2 b. The molecular structure is only visible as small oscillation on top of the overall decrease due to the atomic and inelastic scattering intensities I_b. For illustration of the scattering due to the molecular structure, Figure 2.2 c and d show the radial plot of the modified scattering intensity in both definitions $M(s)$ and $sM(s)$. The multiplication by s in $sM(s)$ leads to a convenient oscillation of the signal around the zero-line. From the distance of two maxima within Figure 2.2 d, which is $\Delta s \approx 0.9 \cdot 10^{10}/\mathrm{m}$, the distance r of the two atoms can be deduced by $r = \frac{2\pi}{\Delta s} \approx 700\,\mathrm{pm}$.

For more complicated molecules than diatomics, the diffraction patterns need a more elaborate analysis [17, 70]. The approach within this thesis for isotropic samples is to simulate $sM(s)$ and then compare the simulated radial plot to radial plots created from experimental data.

In order to find a molecule for controlled molecule experiments, several candidates were considered (Figure 2.3), which exhibit a dipole moment that allows for electrostatic

[1] Radial plots of simulations were performed corresponding to experimental analysis. The signal of each pixel was assigned to a radius. The sum for each radius is then plotted after binning. For the plots the detector radius was transformed to s.

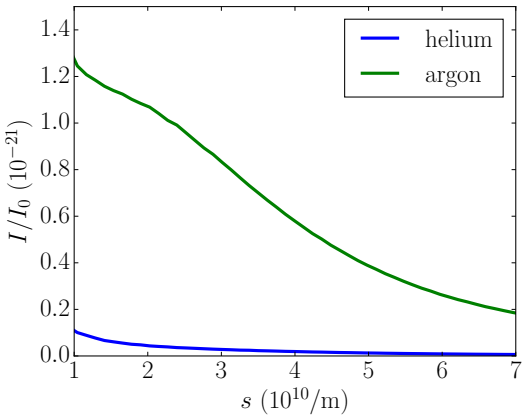

Figure 2.4: The total scattering intensity is shown for helium and argon.

deflection and a polarizability anisotropy, which is utilized for spatial alignment by intense laser light. Details on deflection and alignment are discussed in chapter 3. With respect to the feasibility of electron diffraction experiments the absolute molecular scattering intensity has to be larger than the noise level of the background. For comparison, Figure 2.3 depicts the molecular scattering intensity normalized to the incoming intensity, $I_m(s)/I_0$, for carbon sulfur oxide (OCS), 2,5-diiodobenzonitrile (DIBN), and diiodomethane. Due to the high Z of iodine, the two molecules with iodine atoms show oscillations with larger amplitude in the molecular scattering intensity, $I_m(s)/I_0$, from which the molecular structure can be calculated. The structure of DIBN is favorable as it shows more local minima and maxima for low s ($10^{10}/\mathrm{m} < s < 3 \cdot 10^{10}/\mathrm{m}$), where the diffraction signal is higher. Moreover, this would allow for a comparison with x-ray diffraction experiments performed on the same molecule [36]. Therefore, DIBN was chosen as candidate for benchmark diffraction experiments.

2.3.2 Signal-to-noise for experimental conditions

Considering DIBN as a sample molecule, simulations were performed for realistic experimental conditions. These were used to predict the expected signal-to-noise ratio. For molecular beam experiments, the noise was estimated, which originates from statistical variations of the background scattering off the atomic gases that the molecules are seeded in (see chapter 3 for details on molecular beams). Therefore, the scattering off DIBN and the background scattering due to seeding gas was simulated. In Figure 2.4 scattering intensities of helium and argon are compared. Argon scatters significantly more than helium due to its higher atomic number Z. Therefore, helium is preferred as seeding gas for diffraction experiment.
In experiments in subsection 5.4.1 the helium density in the direct beam at the interaction point was estimated to be $n_{\mathrm{helium}} = 1.5(5) \times 10^{12}/\mathrm{cm}^3$. For optimal experimental conditions the molecular density for an undeflected sample can be on the order of

$n \approx 10^9$ molecules/cm^3 (section 3.2). Without deflection the amount of helium was therefore estimated to be 2000 times higher than the amount of the sample molecule. This corresponded to a seed ratio in the valve of 50 mbar DIBN in 100 bar helium, assuming that the ratio of sample to seed gas does not change during molecular beam propagation. Depending on the molecule, the ratio of helium to sample can be higher, but the value of 2000 for optimal experimental conditions is assumed here.
A sample of deflected DIBN molecules has a reduced molecular density of typically $n \approx 10^8$ molecules/cm^3 at the interaction point (see chapter 3 and reference 36), which is used for the estimations in the following. The expected scattering signal S can be calculated by

$$S = \frac{I}{I_0} N_e \, n \, l \, r \, t \tag{2.26}$$

with the electron number per pulse N_e, the interaction region length l, the repetition rate r and the experimental averaging time t. For an estimation the following parameters were assumed: $l = 100\,\mu\text{m}$, $r = 500\,\text{Hz}$, and an averaging time $t = 12$ hours, which is a reasonable time for all experimental parts to be stable. An extension of this time would be possible by averaging over several runs.
Using I/I_0 from simulations for DIBN and helium the number of necessary electrons per pulse were estimated. The aim is that the molecular scattering signal becomes larger than the noise due to background scattering I_b, which in the here discussed case mostly consists of scattering off helium. The radial plots of the diffraction signal are depicted in Figure 2.5, for $N_e = 10^6$ electrons per pulse and the parameters above. They show that this number of electrons would be a reasonable starting point, as described in the following.
At first, the ratio of 2000 between helium and DIBN is assumed. In the total scattering intensity (Figure 2.5 a) almost no modulation is visible. In order to analyze the diffraction pattern, $M(s)$ was calculated with I_b as in equation 2.25. The experimental $M(s)$ could then be compared to the corresponding simulations. In contrast to equation 2.25 only helium gas is used as background here, as it can be measured separately from DIBN under similar experimental conditions (chapter 5). This variation of the modified scattering intensity $M'(s) = (I_{\text{total}} - I_{\text{helium}})/I_{\text{helium}} = I_{\text{DIBN}}/I_{\text{helium}}$ is depicted in Figure 2.5 b. Its modulations could be assigned to the molecule DIBN. The oscillations are not around the zero line as the helium intensity was subtracted and not the full background including the atomic contributions of DIBN. For small s the errors originating from statistical noise of the total signal were smaller than the modulations. Considering the size of the statistical errors plotted in Figure 2.5 b, the experimental conditions listed above should be aimed for as a minimum within the experiment to allow for a signal modulation amplitude that is detectable in comparison to the error bars. $N_e = 10^6$ electrons per pulse are the starting point for the design of the electron gun in chapter 4. In subsection 4.4.1 further experimental background sources are discussed. They include rest gas scattering and a background signal originating from the apparatus.
A possible experimental improvement would be to reduce the amount of helium in relation to the molecular density. This is possible by separating the molecule from helium with the

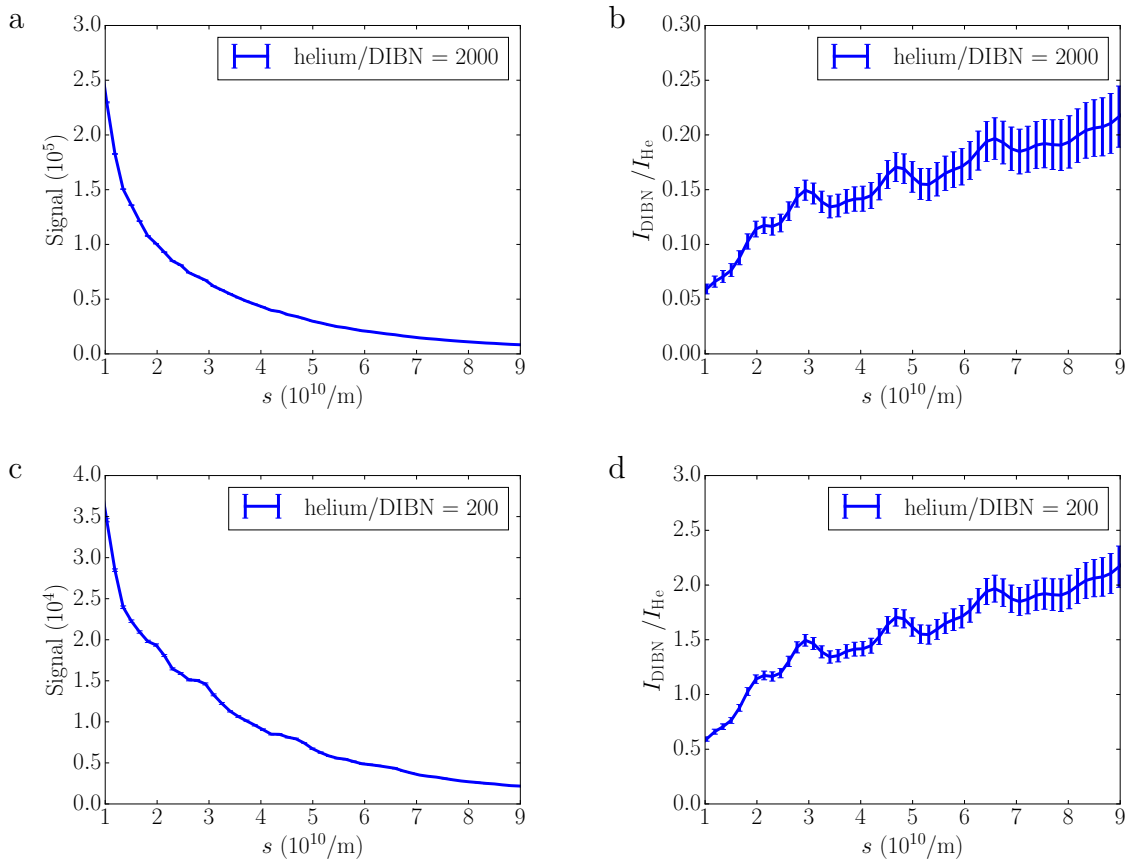

Figure 2.5: The total scattering intensity of DIBN seeded in helium is shown (a, c). Information on the molecular scattering can be derived by subtracting the total intensity for only helium from the total signal (b, d). In (c, d) the amount of helium in relation to DIBN is 10 times smaller than in (a, b).

aid of electrostatic deflection (chapter 5). A reduction of the ratio by a factor of 10 would lead to the intensity shown in Figure 2.5 c, where the signal modulations due to DIBN become visible in the total intensity signal. Accordingly, the radial plot of $I_{\mathrm{DIBN}}/I_{\mathrm{helium}}$ in Figure 2.5 d shows a higher signal-to-noise ratio. Now the modulations are clearly larger than the noise due to I_b. It was concluded that the helium reduction assumed in the simulation of Figure 2.5 d should be aimed for in the experiment.

2.3.3 Simulation for aligned molecules

Advantages of spatial alignment in electron diffraction experiments are illustrated within this section for the example of DIBN. As discussed in section 2.2 the diffraction patterns were calculated for an ensemble of differently oriented molecules. Their distribution of

orientations was determined from the degree of alignment $\langle\cos^2\theta_{2D}\rangle$.[2] Then, the diffraction patterns of the differently oriented molecules were summed incoherently to give the ensemble-averaged signal.
Simulated diffraction patterns of an isotropic sample and two differently well aligned samples are depicted in Figure 2.6. The molecules' most polarizable axis, which is under a small angle of 7.8 ° with respect to the I-I axis [67], was aligned in the direction corresponding to the vertical dimension in the depicted 2D-images. The color scale was kept the same within each column to facilitate a comparison. The left column shows the total scattering intensity normalized on the incoming intensity, while the right column depicts the modified scattering intensity. For an isotropic sample, no structure was visible in the intensity image (a), but only in the modified scattering intensity (b). In contrast, for the aligned samples (c,d: $\langle\cos^2\theta_{2D}\rangle = 0.8$ and e,f: $\langle\cos^2\theta_{2D}\rangle = 0.9$), the structure already appeared in the total intensity and the modified scattering intensity showed locally increased contrast. The anisotropy increased for a higher degree of alignment.
The modulations along the alignment axis exhibited a larger amplitude compared to the those in perpendicular direction. This would facilitate experiments with low density, as the contrast was enhanced in parts of the detected image. In order to analyze diffraction patterns of aligned molecules, one would not form the radial sum for all angles, but compare different sectors of the diffraction pattern or compare the overall pattern. The anisotropy in the diffraction pattern could be used to examine the molecular structure [71]. It would allow to extract 3D information using a genetic algorithm [38]: A point spread function could be used to map scattering from a perfectly aligned sample to a distribution of partially aligned molecules for different projections of the molecule (supplementary materials of reference 38). From measured diffraction patterns at different alignment settings the diffraction pattern for perfect alignment could then be reconstructed [38]. A diffraction pattern for perfect alignment allows to retrieve the 3D-structure [34, 38, 39]. This reconstruction becomes important when 3D-information of a molecule is desired and only the constituent atoms are known, for example for the determination of a transition structure during structural changes of a molecule [38]. Moreover, when approaching experiments with large, biological relevant molecules, alignment of molecules combined with diffraction is a promising tool for structure determination [33].
In the experiment presented in chapter 5 not all of the imaged molecules would be aligned. In the setup the electron beam and the laser are both perpendicular to the molecular beam. A schematic view is depicted in Figure 2.7 a. From the beam dimensions at the interaction point one can calculate the ratio of aligned to not-aligned molecules in the volume that is probed by the electron beam.
For a molecular beam size of 1 mm, a laser focus size of 100 µm and an electron beam spot size of 500 µm only 1% of the probed molecules would be aligned. The corresponding modified scattering intensity is shown in Figure 2.7 b for a degree of alignment of $\langle\cos^2\theta_{2D}\rangle = 0.9$. Increase in contrast and anisotropy were not visible anymore. Increasing the percentage

[2] $\langle\cos^2\theta_{2D}\rangle$ describes the degree of alignment, see chapter 3. A value of $\langle\cos^2\theta_{2D}\rangle = 0.5$ would be isotropic and $\langle\cos^2\theta_{2D}\rangle = 1$ would be perfectly aligned.

of aligned molecules to 10 % would yield the diffraction pattern in Figure 2.7 c, which showed small anisotropy indicated by the asymmetry of the central peak. The increase in contrast would be negligible. With larger fractions of aligned molecules the positive effects of alignment were retrieved as depicted in Figure 2.7 for 25 % (d), 36 % (e) and 50 % (f). These simulations imply that the overlap of electron beam and laser should guarantee a minimum of 10% of aligned molecules within the probed sample. This could, for example, be achieved by reducing the electron beam size to the laser focus size of 100 µm, while not changing the molecular beam size of 1 mm. Reducing the molecular beam width would improve the ratio further towards some 10% as discussed in chapter 6. Full temporal overlap is assumed in these estimations as alignment laser pulse durations for adiabatic alignment are typically on the order of 100 ps (chapter 3), while the electron gun discussed in chapter 4 produces electron pulses with a simulated pulse duration of 60 ps.
Comparing the 2D images of the modified scattering intensity in the case of $\langle\cos^2\theta_{2D}\rangle = 0.8$ and full overlap (Figure 2.6 d) with improved alignment $\langle\cos^2\theta_{2D}\rangle = 0.9$ and 50% overlap (Figure 2.7 f), one finds that the expected contrast would be very similar. The two images show small differences in the distribution of signal: The region with increased contrast along the vertical axis is more narrow in Figure 2.7 f due to the better degree of alignment. Moreover, there is less signal oscillation in horizontal direction in Figure 2.6 d due to the lack of scattering off the isotropic sample, which is present in Figure 2.7 f. Despite these small differences the two images are very comparable concerning contrast and degree of anisotropy.
For experiments both – overlap and degree of alignment – have to be considered with respect to contrast and anisotropy in the diffraction pattern. Furthermore, properties of the electron beam have an effect on the contrast of the diffraction pattern. The electron beam has a finite spot size on the detector and could be only partially coherent compared to the sample size. Both effects would lead to further reduction of the signal modulation amplitude and therefore, decrease the contrast. These effects were studied experimentally as well as in simulation and are discussed in chapter 4.

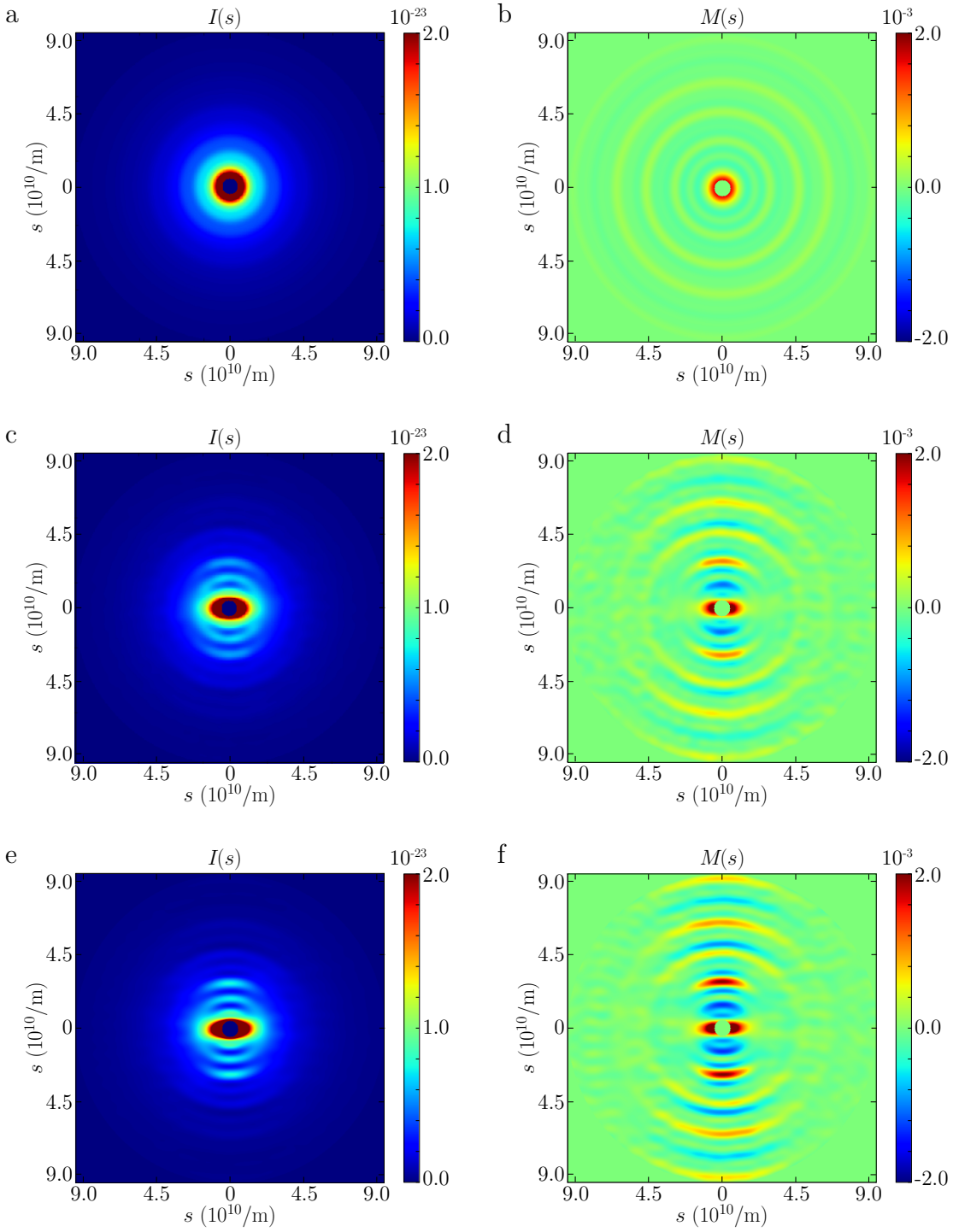

Figure 2.6: The total scattering intensity and the modified scattering intensity on the detector is shown for DIBN for different degrees of alignment: isotropic sample (a,b), aligned with $\langle \cos^2 \theta_{2D} \rangle = 0.8$ (c,d) and aligned with $\langle \cos^2 \theta_{2D} \rangle = 0.9$ (e,f).

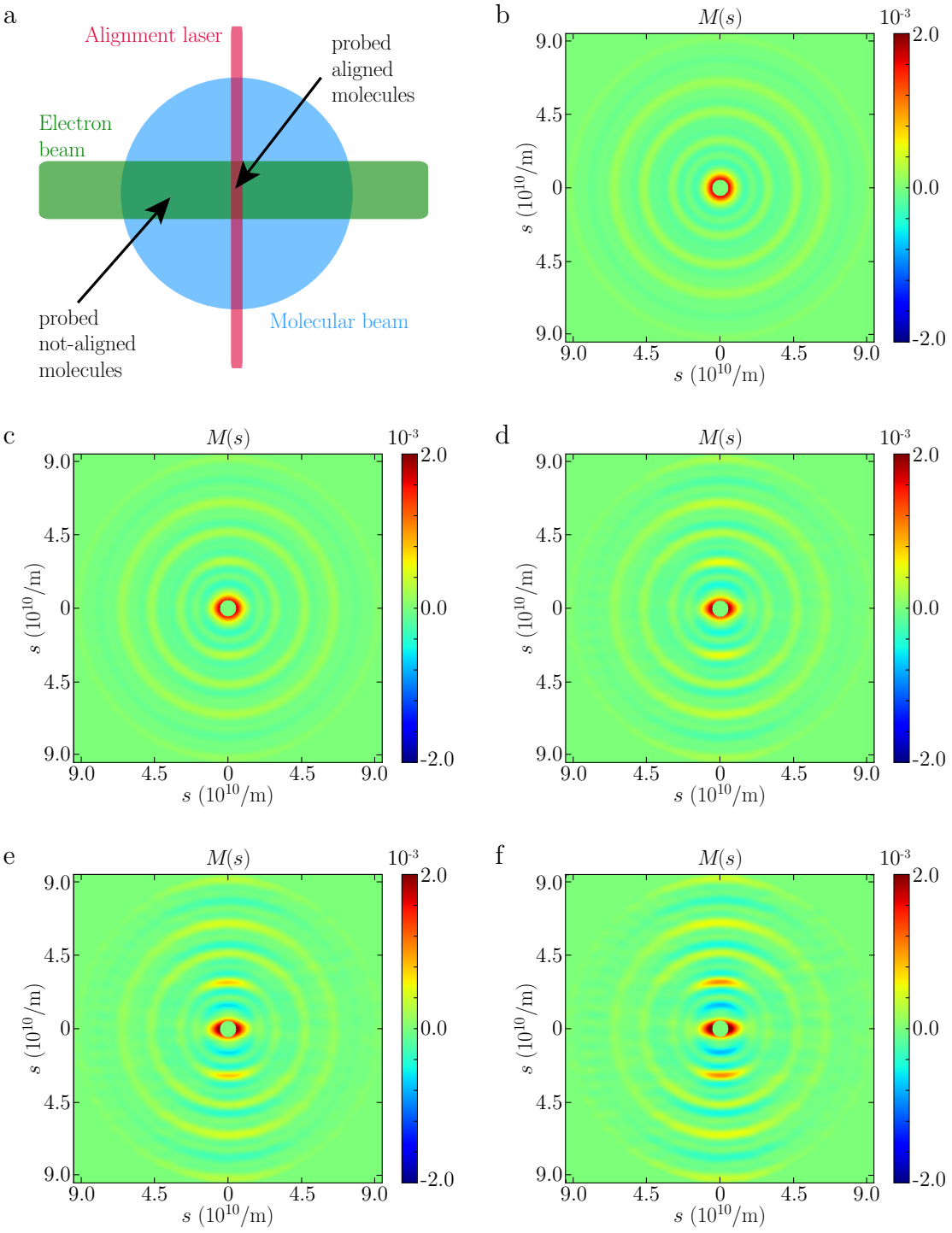

Figure 2.7: The scheme in (a) depicts the fraction of aligned molecules that are probed for a diffraction experiment with laser, electron beam and molecular beam perpendicular to each other. The modified scattering intensity is depicted for 1 % (b), 10 % (c), 25 % (d), 36 % (e) and 50 % (f) aligned molecules with $\langle \cos^2 \theta_{2D} \rangle = 0.9$. The color scale is kept constant for illustration.

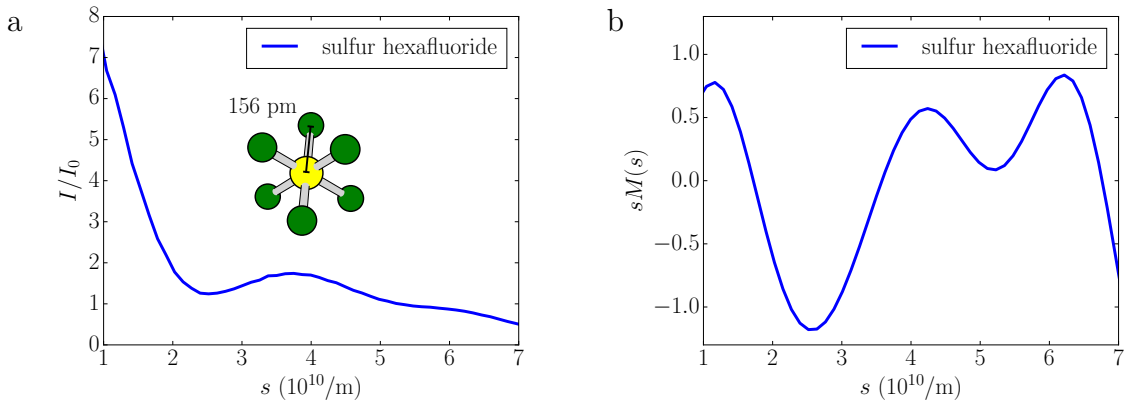

Figure 2.8: The total scattering intensity (a) and modified scattering intensity (b) for sulfur hexafluoride. The inset in (a) depicts the molecular structure.

2.3.4 Simulation of a calibration molecule

In the course of commissioning the setup for electron diffraction off controlled gas-phase molecules, the electron source was tested on calibration gases (section 5.2). It was considered convenient to perform scattering experiments on a molecule that shows high contrast in the diffraction pattern without the need of alignment. A typical calibration molecule that fulfills these requirements, is sulfur hexafluoride (SF_6). Figure 2.8 a depicts the scattering intensity relative to the incoming intensity for SF_6. For structure determination, the modified scattering intensity $sM(s)$ was deduced from the simulations (Figure 2.8 b). With six identical bonds, the contribution of the molecular scattering was large enough to be visible in the total intensity. This was advantageous for benchmark experiments, which were performed to test the electron source setup and to compare the simulations with the experimental data (chapter 5). During these tests the S-F bond length of SF_6 was determined by comparison of simulation and experiment. The corresponding analysis is discussed in section 5.2.

3 Control of gas-phase molecules for experiments on structural dynamics

This chapter treats two types of molecular control that are employed to improve imaging experiments in the gas-phase. As discussed in chapter 2, alignment of molecules enhances the information that can be gained from diffraction patterns. Moreover, strong inhomogeneous electric fields allow for separation and hence selection of quantum states, structural conformers and cluster sizes of molecules according to their effective dipole moment [48, 72].
The first section of this chapter gives an overview of the fundamental concepts of alignment, orientation, and of state-selection by electrostatic deflection. The setup and operational modes of a velocity map imaging spectrometer are introduced. This type of spectrometer was used to image the spatial orientation of molecules and for characterization measurements in chapter 4 and chapter 5. The second section elaborates how spatial control and state-selection were employed experimentally. The experimental setup provided a beam of strongly aligned and oriented molecules at high repetition rates. The selection of molecules in low-rotational energy states improved the spatial control.

3.1 Generation and imaging of controlled molecules

3.1.1 Basics of alignment and orientation

The spatial orientation of molecules in the gas-phase can be controlled by application of electric fields. Figure 3.1 a depicts an ensemble of iodobenzene molecules for the isotropic and spatially controlled cases. One or all axes of a molecule can be fixed to the laboratory frame. This is called 1D-alignment or 3D-alignment, respectively. Figure 3.1 a (center) shows an example of 1D-alignment. The molecules' orientation in space still exhibits an up-down symmetry. This symmetry can be broken, which yields a so-called 1D-orientation of the molecules as depicted in Figure 3.1 a (right). 3D-orientation would mean that the molecular frame is fully fixed to the laboratory frame. Theory of alignment and orientation are discussed in detail elsewhere [49, 73–76] and the concepts are summarized in the following.
If the molecules exhibit an anisotropy in their polarizability, strong, non-resonant, alternating electric (ac) fields can be employed to create a sample of aligned molecules. The

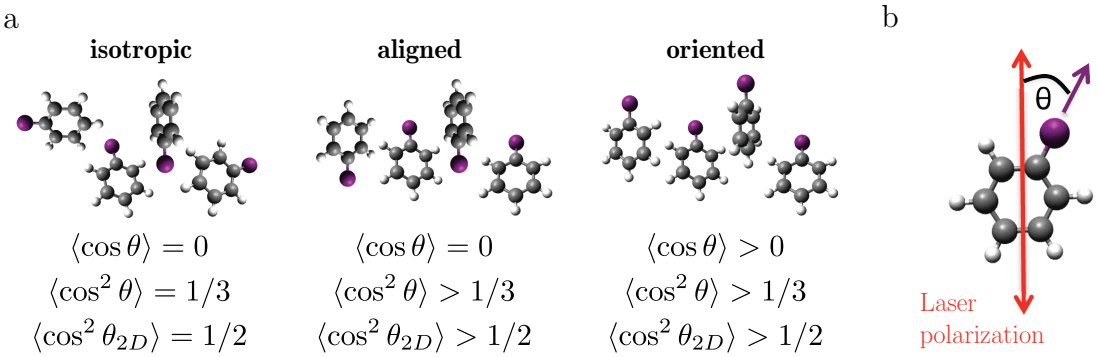

Figure 3.1: Ensembles of gas-phase molecules like iodobenzene can be isotropic, aligned along one axis, or oriented in space (a). The angle θ describes the angle between the molecule's most polarizable axis and the laser polarization (b). The expectation values describe the degree of alignment and orientation (a).

laser induces a dipole moment in the molecule and the interaction between this dipole moment and the laser field leads to a lower energy of the system for the molecule being aligned along the polarization axis of the laser. In the case of 1D-alignment the ac field E_L is generated by an intense, non-resonant, linearly polarized laser. For the used laser frequencies, the laser's electric field oscillation is much faster than the rotational period of the molecule. The coupling of the molecule's dipole moment to the field vanishes. In second order, the time-averaged squared electric field E_L^2 of the laser induces a dipole moment within the molecule if the molecule exhibits an anisotropy in the polarizability. For an asymmetric top like iodobenzene this means that the diagonal elements of the polarizability tensor, the principal polarizabilities α_{xx}, α_{yy} and α_{zz} in the molecular fixed frame are not the same. For iodobenzene the polarizability along the C-I bond (indicated by the violet arrow in Figure 3.1 b) is the largest. The interaction term in the Hamiltonian for a molecule in the time-averaged laser field reads

$$H_{int} = -\frac{1}{4}(E_L^2 \sin^2\theta(\alpha_{xx}\cos^2\chi + \alpha_{yy}\sin^2\chi) + \cos^2\theta\alpha_{zz}) \tag{3.1}$$

θ is the angle between the laser polarization and the most polarizable axis of the molecule as depicted in Figure 3.1 b. The molecule can still exhibit a motion in the azimuthal angle of rotation χ about the body-fixed z-axis. The eigenstates of the Hamiltonian of a molecule in the laser field are so-called pendular states, which are a coherent superposition of field-free eigenstates of the molecule. Molecules in pendular states exhibit a confinement of the molecular-fixed axes to the laboratory-frame. Here, the molecule's most polarizable axis is locked to the polarization axis of the laser as depicted in Figure 3.1 b. In order to quantify the degree of alignment one specifies the expectation value $\langle\cos^2\theta\rangle$. In our experiment its 2D-projection $\langle\cos^2\theta_{2D}\rangle$ onto the detector was measured.
In order to fix the molecular frame in 3D to the laboratory coordinate system an elliptically polarized laser can be used. For 3D alignment the most polarizable axis of the molecules

is aligned to the long axis of the polarization ellipse and the second most polarizable to the short axis [77, 78]. Within the framework of this thesis 1D alignment was used. The diffraction pattern of the candidate molecule DIBN is mainly determined by the iodine atoms (chapter 2). Their spatial orientation is fixed by 1D-alignment alone as the most polarizable axis is close to the I-I axis [67].

Throughout this thesis, adiabatic alignment was used, which implies a slow increase of the laser intensity compared to the rotational period of the molecule. In this case the system transfers from a free-rotor eigenstate into the corresponding eigenstate of the field-dressed Hamiltonian (equation 3.1). The molecules are aligned for the duration of the laser pulse and when the laser is switched off, the system returns to the same free-rotor state as before.

Spatial orientation of molecules in the gas-phase can also be reached by strong electrostatic (dc) fields. The interaction potential of a polar molecule with the dipole moment μ in a dc field $\mathbf{E}$ is given by the linear Stark effect

$$H_{\text{stark}} = -\mu\mathbf{E} = -\mu E\cos(\theta). \tag{3.2}$$

θ is the angle between μ and $\mathbf{E}$. The energy is minimized, if the molecule's dipole is oriented along the electric field axis. This is the so-called brute-force orientation. Necessary field strengths for significant orientation are on the order of $30 - 100\,\text{kV/cm}$ depending on the sample molecule [76, 79]. Orientation can also be achieved by combining ac and dc electric fields for so-called mixed-field orientation [75]. For an aligned molecule, the system's energy is minimal for two angles – the molecule pointing upward and downward along the polarization axis. The static electric field then further decreases the energy of the system for one of the two minima and breaks the up-down symmetry in alignment. This is possible with field strengths two orders of magnitude lower than for brute force orientation [50]. The degree of orientation is quantified by $\langle\cos\theta\rangle$. The measured 2D projection is $\langle\cos\theta_{2D}\rangle$. Combining an elliptically polarized laser with a static electric field yields 3D orientation [78]. The adiabaticity of orientation does not only depend on the duration of the laser pulse, but also on the applied field strength and the resulting coupling of states [53, 80].

Values for the degree of alignment and orientation are given in Figure 3.1. For a sample of molecules that is aligned or oriented in n dimensions, the expectation values are between the isotropic value, which is given by $1/n$, and 1, which corresponds to perfect alignment or orientation, respectively. The degree of alignment and orientation depends on the laser intensity, laser duration, the populated rotational states, and in the case of orientation on the applied static-field strength. Selecting the low-rotational-energy states improves the degree of alignment and orientation. This can be realized by separating the molecular states by electrostatic deflection [50, 51, 72, 81] as discussed in the next section.

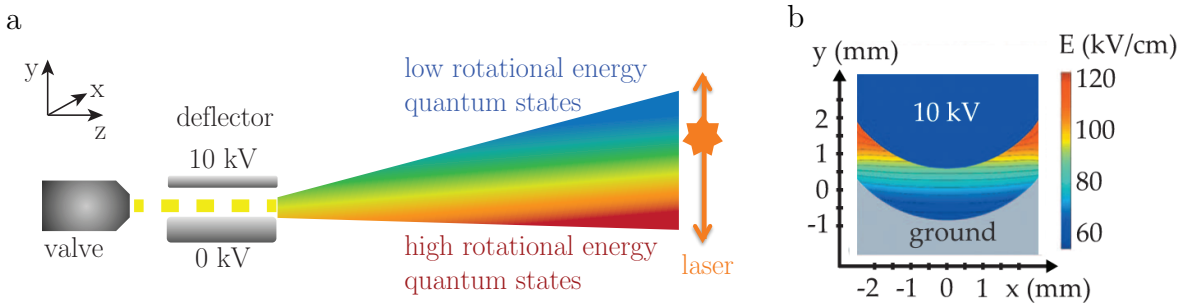

Figure 3.2: A beam of cold iodobenzene molecules passes the strong, inhomogeneous electric field of a deflector. Molecules in low rotational energy quantum states are deflected more. A laser can be scanned along the molecular beam to study the effect (a). A cross section of the electric field norm within the deflector is depicted (b). Figure (b) is from reference 35.

3.1.2 Concepts of electrostatic deflection

Quantum-state selection is possible by electrostatic deflection, which exploits the permanent dipole moment of the molecule [72]. The basic scheme is depicted in Figure 3.2 a[1]. A beam of cold, polar molecules passes a strong, inhomogeneous electric field created by the deflector. Due to Stark forces the molecules separate according to their quantum state [82]. Adapting the detection laser position in y dimension allows for selection molecules in low-rotational-energy states [50, 51, 72, 81].
Within this work, the electric field was created by two electrodes as depicted in Figure 3.2 b. A rod with an applied voltage on the order of 10 kV was positioned at a distance of approximately 1.4 mm from a trough on ground potential. An electric field norm was generated that was constant in x-direction but increasing in y [35, 48, 83].
The deflection depends on this electric field gradient and the dipole-moment-to-mass ratio of the molecule at the given field strength. The underlying force originates from the Stark effect (equation 3.2), which can be visualized in so-called Stark-energy maps. The Stark-energy curves for the low-rotational-energy quantum states $1_{00}0$, $1_{01}0$ and $1_{01}1$ of iodobenzene are depicted in Figure 3.3 a. The notation of the states is $J_{K_aK_c}M$ with the rotational quantum number J and the projection of $\mathbf{J}$ onto a space-fixed axis M. K_a and K_c are the projections of $\mathbf{J}$ onto the symmetry axis of the molecule in the prolate and oblate limit. The Stark energies W were calculated as a function of applied electric field E using CMIstark [84]. All depicted states are so-called high field seekers for the applied field strengths (yellow-shaded area in Figure 3.3). Their energy W decreases for higher electric fields. Molecules in these states move towards higher fields, so in positive y direction, when they pass the deflector (Figure 3.2).
The gradient with respect to E is the effective dipole moment μ_{eff} and is shown for the

[1]Due to the chronological development of this thesis, the coordinate system used in this chapter has a different orientation than in the other chapters.

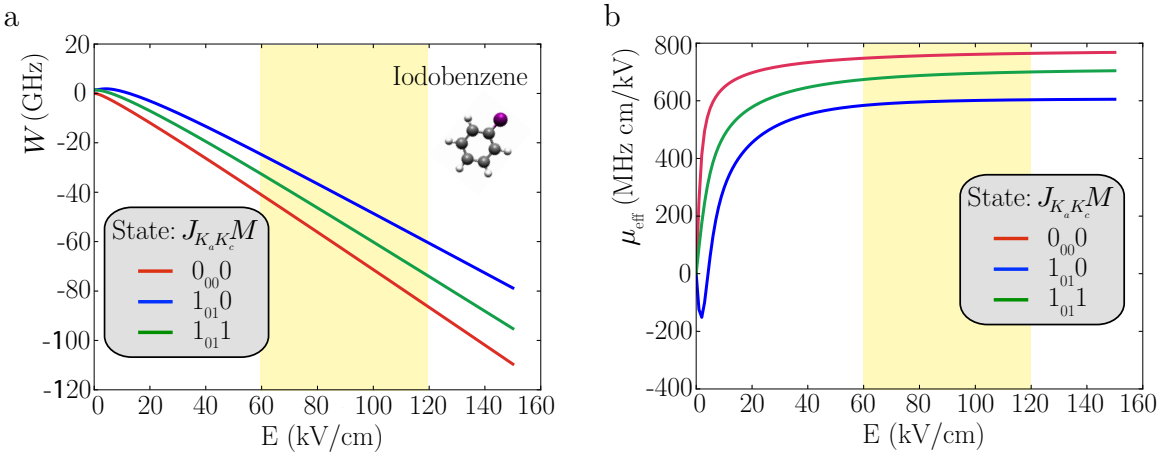

Figure 3.3: The Stark-energy map for iodobenzene (a) depicts the energy of some low rotational energy states as a function of the employed electric field. The corresponding effective dipole moment (b) is the slope of the curves for the corresponding states in the stark map (a). The yellow-shaded area corresponds to the electric field strengths typically applied in the experiment.

same molecular states in Figure 3.3 b. The larger the effective dipole moment, the larger is the force $F_{stark} = -\nabla W$. This implies that the ground state $0_{00}0$ is deflected most. It is to be noted that for adiabatic processes no redistribution of populations takes place. The colder the molecular beam is before deflection, the higher is the population of the ground state. In order to create a sample that contains a large amount of ground state molecules it is therefore crucial to start with a rotationally cold beam. Then, molecules in low rotational quantum states or even in the ground state $J = 0$ can be selected after deflection, which increases the degree of alignment and the orientation in comparison to an undeflected cold molecular beam (section 3.2).

3.1.3 Velocity map imaging spectrometer as tool for controlled molecules experiments

Appropriate inhomogeneous electric field configurations can be used to image the spatial orientation, spatial distribution and momentum distribution of charged particles. A velocity map imaging spectrometer (VMI) [85–88] was used to generate these fields. In the original form, the VMI consists of three round plates with central holes similar to an electrostatic ion lens: one repeller plate, one extractor plate and one on ground potential as shown in Figure 3.4. Ideally the repeller plate has no opening, while the inner hole size increases from extractor to ground plate. The particles that are imaged start between repeller and extractor plate. In Figure 3.4 iodobenzene is ionized and the I^+ ions are detected.
The repeller voltage determines the acceleration of the ions and hence the size of the image on the detector. The ratio between repeller and extractor allows for different operational

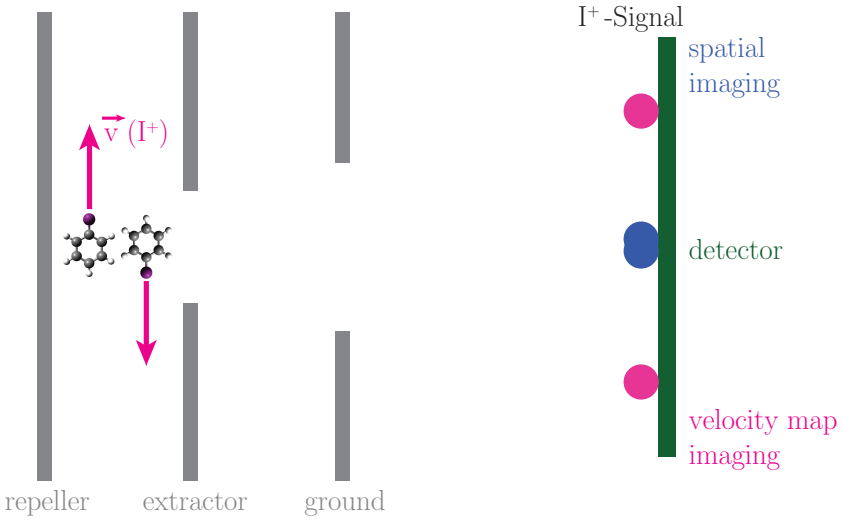

Figure 3.4: A basic velocity map imaging spectrometer [85] consists of three plates: extractor, repeller and ground. The molecule iodobenzene is ionized between repeller and extractor plate. The I^+ ion departs along the C-I bond axis. Its arrival point on the detector depends on the ratio between repeller and extractor voltage. In spatial imaging the spatial distribution of charged particles is mapped on the detector. In velocity map imaging mode the momentum distribution is recorded.

modes. The modes spatial imaging and velocity map imaging are depicted in Figure 3.4. In spatial imaging all particles from one point in the interaction region will arrive at the same point on the detector. In first order this is independent of their momentum distribution. The resulting image on the detector corresponds to the spatial distribution in the interaction region. Calibration can be performed by simulation of electric fields and particle trajectories, for example by the software SIMION. In the experiments a calibration can be achieved by scanning the ionization point in a well-defined way, for example by moving the laser focus position. The other mode is called velocity map imaging, in which the resulting detector image is a Fourier transform of the momentum distribution after ionization. All particles with the same momentum arrive at the same point on the detector independent of the spatial distribution at the interaction point. Calibration can be performed by simulation or to a known momentum distribution, for example ionization channels. Images in both modes are projections of the three-dimensional space onto a two dimensional detector. An inverse Abel transform allows for the retrieval of the three dimensional distribution [85] if the system is cylindrically symmetric and the symmetry axis parallel to the detector surface.

In the experiments throughout this thesis, the velocity map imaging mode was used to determine the spatial orientation of molecules [49, 89]. If a molecule, here iodobenzene, is multiply ionized by strong field ionization, the positive charges within the molecule will lead to Coulomb explosion. If the I-C bond of iodobenzene is broken, the I^+ ion will depart

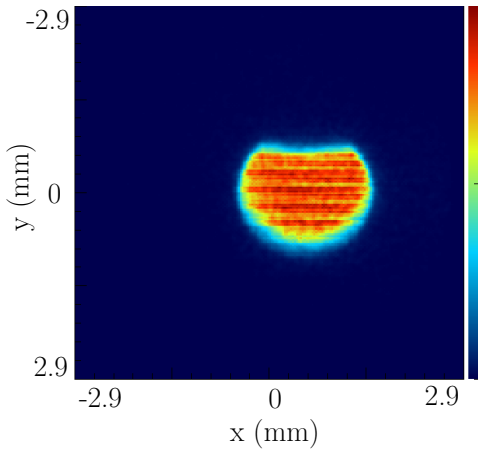

Figure 3.5: A laser ionized molecules and the ion signal is recorded in spatial imaging mode. Measurements for different laser focus positions in y were summed. x and y were calibrated, so that the shown signal corresponded to the molecular beam profile at the interaction point of laser and molecular beam.

the molecule along the bond direction as depicted in Figure 3.4. The velocity depends on the bond strength and on the amount of created charges and the charge distribution within the molecule. In velocity map imaging mode, an isotropic distribution of molecules creates a circular distribution on the detector. For an aligned ensemble an anisotropy will usually appear in the image. From the signal distribution on the detector the degree of alignment and orientation can be determined. For experimental details see section 3.2, especially Figure 3.7.

An example for the usage of spatial imaging within this work is the optimization of the molecular beam pointing through the deflector. An ionization laser was moved along y through the molecular beam as depicted in Figure 3.2 a. Ions were created along the laser focus range in x and mapped onto the detector in spatial imaging mode. The sum of measurements for the various laser positions in y then corresponded to the molecular beam profile as depicted in Figure 3.5. After calibration, the depicted x and y axis corresponded to the dimensions at the interaction point of laser and molecular beam. The alignment of the molecular beam through the skimmer was good, if the profile was symmetric in x. The dip in y corresponded to the rod of the deflector in Figure 3.2, which the molecules hit. Such collisions lead to heating of the molecules. The spatial imaging mode allowed to align the molecular beam with the deflector, which was important in order to minimize the loss and heating of the molecules. Low temperatures of the molecular beam were important for achievement of high degrees of alignment (section 3.2).

3.2 Strongly aligned and oriented molecular samples at a kHz repetition rate[2]

3.2.1 Introduction to experiments with controlled molecules

Aligned and oriented molecules serve as ideal samples to study steric effects in chemical reactions [49, 90] and to image the structure and dynamics of complex molecules directly in the molecular frame, if that is strongly confined, i. e., linked to the laboratory frame of the measurement. This would yield so-called "molecular movies" of the ongoing dynamics, conceivably without prior knowledge on the investigated system.

Bretislav Friedrich has been at the forefront of the development of methods to control complex molecules, including brute force orientation [74, 76], laser alignment [73] and mixed-field orientation [75, 91]. At that time, the degree of alignment and orientation was too weak to image molecular dynamics directly in the molecular frame. However, over the last two decades, the available degree of control has been constantly increased. The combination with rotational-state selection [50, 81] has improved the achievable control dramatically, with the strongest demonstrated degree of alignment so far of $\langle\cos^2\theta_{2D}\rangle > 0.97$ [50]. In addition, recent results on the orientation of molecules in mixed fields show that the adiabaticity and the resulting degree of orientation strongly depend on the applied electric fields, i. e., the laser-pulse duration [80].

Strong laser alignment and mixed-field orientation has been exploited in the recording of molecular frame photoelectron angular distributions of complex molecules [12]. Controlled samples increase the contrast in all direct imaging experiments. They allow the simple averaging of many individual experiments, they simplify the data analysis, and no orientation relationship between patterns from randomly oriented molecules need to be derived numerically [33, 35]. Moreover, they are crucial to various advanced "photography" experiments: Tomographic reconstruction approaches for X-ray [34, 35] or electron diffraction [38, 92] and photoelectron holography experiments of aligned molecules require typically $\langle\cos^2\theta_{2D}\rangle \approx 0.9$ [35, 93].

Such a strong degree of alignment has, so far, only been achieved in adiabatic alignment experiments making use of very cold molecular beams and nanosecond laser pulses at a repetition rate of a few 10 Hz [50, 54]. However, the low repetition rates renders time resolved studies of molecular dynamics, with their generally low count rates, tedious, at least, or even infeasible. Therefore, experimental setups which provide strong alignment at high repetition rates are highly desirable. This requires the production of cold molecular beams of complex molecules and strong laser fields with pulse durations that are comparable or longer than the rotational period of the molecules. The lack of nanosecond lasers with

[2] This section is based on the paper *Strongly aligned and oriented molecular samples at a kHz repetition rate*, S. Trippel, T. Mullins, N.L.M Müller, J. S. Kienitz, K. Długołęcki, J. Küpper, *Molecular physics* **111**(12-13), 1738 (2013).
I have contributed to the setup and commissioning of the presented apparatus and took part in the experiments. I assisted S. Trippel in the data analysis and in writing of the publication.

sufficient pulse energies at kHz repetition rates suggests the use of laser pulses generated by an amplified Ti:Sa laser system. However, the generation of such laser pulses with pulse durations on the order of 1 ns and the required peak intensities of $> 10^{11}$ W/cm^3 is challenging. Moreover, *a priori* it has been unclear whether "heavy" molecules with a rotation time in the order of a few hundred picoseconds (like iodobenzene) can be strongly aligned by a sub-nanosecond, strongly linearly chirped broadband 800 nm laser pulse.
Recently, some relevant molecular beam setups with high repetition rates have been developed and some individual ingredients of the necessary control and detection details have been demonstrated [94–96]. A benchmark experiment demonstrating long-pulse alignment of molecules in a low-pressure continuous beam at 1 kHz repetition rate, probed with short ps x-ray pulses from a synchrotron source, has demonstrated weak alignment of $\langle\cos^2\theta\rangle \approx 0.4$ [97]. Impulsive alignment experiments have been performed, again exploiting continuous molecular beams, with lasers operating at kHz repetition rates [98, 99]. The achieved degree of alignment however is typically also only moderately strong ($\langle\cos^2\theta\rangle \leq 0.85$). This makes these approaches not very well suited for molecular-frame imaging studies of complex molecules. Moreover, in these experiments the alignment typically only persists for short periods of time ($\sim$1 ps), which severely limits the time-window for time-resolved experiments, esp. for large amplitude dynamics, such as conformer interconversion or folding motions.
Here, we present a new experimental setup that provides strongly aligned and oriented samples of state-selected molecules at a repetition rate of 1 kHz. This rate is a good compromise between current table-top laser systems, pulsed molecular beam sources, and high speed camera systems. In addition, it demonstrates a clear pathway for the sample preparation at upcoming light sources with high-repetition rates, such as x-ray free-electron lasers (XFELs), synchrotrons, and laser based high-harmonic generation (HHG) sources. In order to efficiently use these light sources, the capability of high repetition rate adiabatic alignment and orientation is highly desirable. Whereas the availability of synchronized pulses from high-power table-top laser systems is practically an intrinsic feature, XFEL facilities, such as the European XFEL in Hamburg, are actively pursuing the setup of high-repetition rate lasers that meet the requirements set by the current work.

3.2.2 Experimental setup

The schematic of the experimental setup is shown in Figure 3.6. Details will be published in a longer account and only a brief description will be presented here. A pulsed molecular beam is provided by expanding 10 mbar of iodobenzene seeded in 120 bar of helium through an Even-Lavie valve [100] cooled to -20 C°. After passing two skimmers the molecular beam enters an electric deflector, where the molecules are dispersed according to their quantum state [72]. The state selected molecular ensembles are aligned or oriented by laser or mixed dc-electric and laser fields [50, 51, 75, 91], respectively, inside a velocity map imaging spectrometer (VMI) [85]. The angular confinement is probed through strong-field multiple ionization by a short laser pulse followed by Coulomb explosion of the molecule.

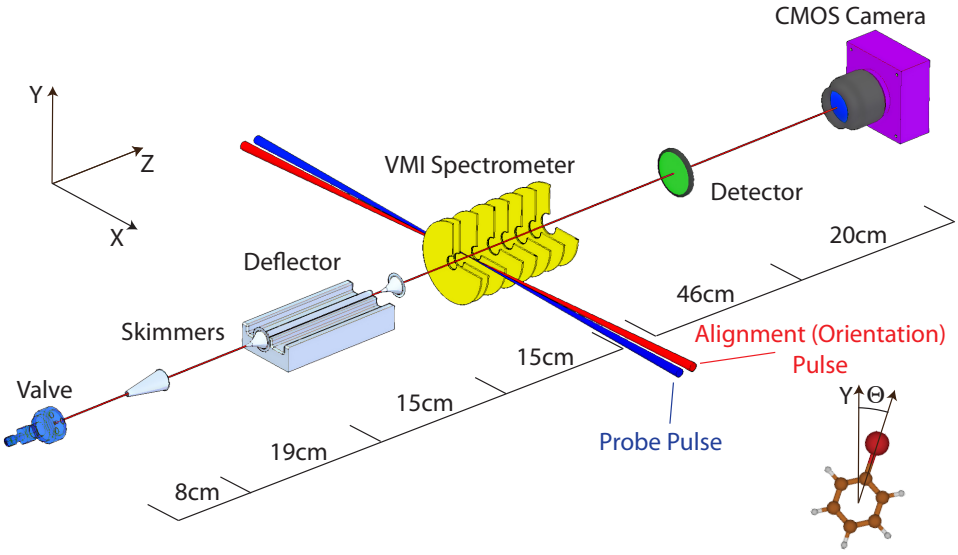

Figure 3.6: Schematic of the experimental setup. The pulsed molecular beam passes two skimmers before it enters the electrostatic deflector where it is dispersed, depending on its quantum states, along the Y-axis. The alignment or orientation laser pulses as well as the probe pulse cross the molecular beam inside of a velocity map imaging spectrometer. The ions are mapped on a position sensitive detector consisting of an MCP and a phosphor screen. The angle θ is defined as the angle between the Y-axis and the most-polarizable axis of the molecule, i. e., the C–I bond axis.

The resulting I^+ ions are velocity mapped onto a 40 mm diameter position sensitive detector (Photonis) consisting of a multi-channel-plate (MCP), a fast phosphor screen (P-46), and a high frame-rate camera. High speed oil-free pumping (4000 l/s for the source and 2000 l/s for deflection and detection chambers, respectively) and optimized operation conditions of the Even-Lavie pulsed valve allow for the generation of dense ($> 10^9$ molecules/cm^3 in the interaction volume) and cold (1 K) molecular beams, whose population distribution is further reduced to some ten rotational states by state-selection [72].

Alignment and ionization laser pulses are provided by an amplified femtosecond laser system (Coherent Legend Elite Duo HE USX NSI) at a repetition rate of 1 kHz. The total output power of the system is larger than 10 W with a bandwidth of ≥ 72 nm centered at 800 nm. Directly behind the amplification stages the laser beam is split into two parts, an alignment (orientation) beam (≈ 9 mJ/pulse) and a probe beam (≈ 1.3 mJ/pulse). The duration of the alignment pulse can be compressed or stretched (negatively chirped) with an external compressor continuously from 40 fs up to 520 ps. The probe beam is compressed to 30 fs using the standard grating based compression setup. Since both beams are produced by the same amplifier system they are inherently synchronized. The two beams are incident on a 60 cm focal length lens parallel to each other with a transverse distance of 10 mm, resulting in field strength of up to 5×10^{11} W/cm^2 and 5×10^{14} W/cm^2 for alignment

and probe pulse, respectively. The foci are overlapped in space and time in the molecular beam and in the center of the velocity map imaging spectrometer. Vertically scanning the lens allows probing different parts of the, typically, quantum state dispersed, molecular beam, i. e., to probe ensembles with varying rotational excitation and correspondingly varying effective dipole moments and effective polarizabilities. This motion is automatized and thus one can completely automatically measure the ion-distribution in the VMI as a function of vertical beam position. From this data, one can determine the molecular beam density, the degree of alignment, and the orientation all at once. A typical scan over the molecular beam at 1 kHz repetition rate takes about 1000 s (*vide infra*).
The imaging system CMOS camera (Optronis CL600x2) is operated at a camera-link-readout- limited resolution of 480 × 480 pixel at sustained 1 kHz repetition rate. This corresponds to a spatial resolution of 80 µm on the phosphor screen. The typical spatial illumination on the camera corresponding to one ion is four pixels. The background corrected camera images are analyzed for every single shot with a centroiding algorithm on a standard PC computer, making use of eight available cores by sequentially distributing the images onto different cores. The coordinates of the ion hits are passed to the main data acquisition system. The single-shot analysis allows high signal rates exploiting the high saturation limit of the detection system.

3.2.3 Results for 1D Alignment and Orientation

Figure 3.7 a) shows the degree of alignment $\langle\cos^2\theta_{2D}\rangle$ [3] as a function of the peak intensity of the alignment pulse; see the inset of Figure 3.6 for a definition of θ. The results are shown for a repetition rate of 1 kHz in solid black (deflector off) and dashed black (deflected beam) as well as for a repetition rate of 100 Hz in solid blue/grey (deflector off) and dashed blue/grey (deflected).
The observed power dependence of the degree of alignment for a cold beam is as expected [54]. For randomly aligned molecules a degree of alignment $\langle\cos^2\theta_{2D}\rangle = 0.5$ is expected. The degree of alignment increases with increasing laser intensity, but is limited by $\langle\cos^2\theta_{2D}\rangle = 1$. The 2D momentum image for I^+ ions for the alignment-field-free case at 1 kHz repetition rate is shown in Figure 3.7 b). The distribution is circularly symmetric as expected for the case of an isotropic sample and the polarization of the probe laser pulse linear and perpendicular to the detector plane. The degree of alignment is given by $\langle\cos^2\theta_{2D}\rangle = 0.5007(5)$. Figure 3.7 c) shows the corresponding ion distribution when the molecules are aligned at 1 kHz repetition rate along the alignment pulse polarization axis, i. e., linear, vertical and parallel to the detector plane. The number of ions is about three ions/pulse and the image has been recorded in less than 10 minutes. The peak laser intensity is 4.2×10^{11} W/cm^2. The degree of alignment determined from the outer

[3] The degree of alignment $\langle\cos^2\theta_{2D}\rangle$ is defined as $\int_0^\pi \int_{v1}^{v2} \cos^2\theta f(\theta, v) d\theta dv$ with $f(\theta, v)$ being the two dimensional ion distribution on the detector. The angle θ is defined as the angle between the polarization of the alignment laser and the projection of the three dimensional ion velocity vector onto the two dimensional detector plane. The velocity is given by $v = \sqrt{v_x^2 + v_y^2}$.

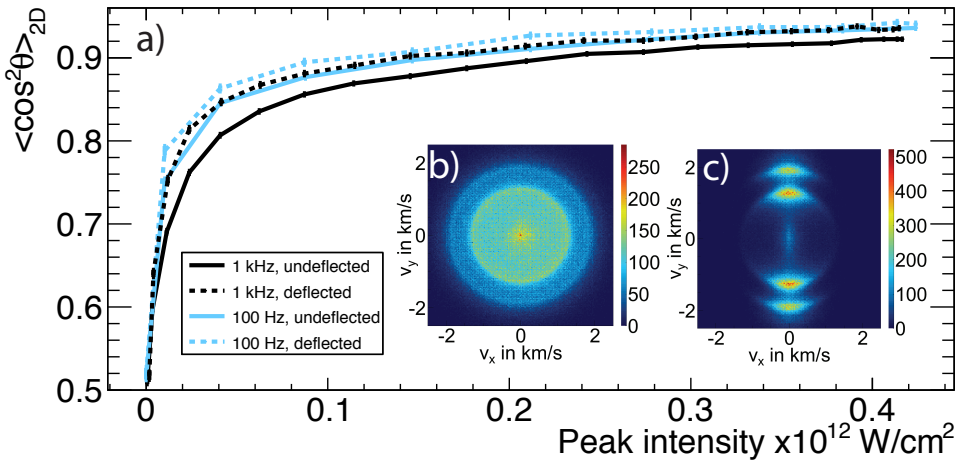

Figure 3.7: (Color online). a) The degree of alignment as a function of the peak intensity of the alignment pulse for a repetition rate of 1 kHz in solid black (deflector off) and dashed black (deflected) as well as for a repetition rate of 100 Hz in solid blue/grey (deflector off) and dashed blue/grey (deflected). The insets show b) the 2D velocity distribution without alignment laser pulse and c) with an alignment pulse with a peak intensity of 0.42×10^{12} W/cm^2 at a repetition rate of 1 kHz in the deflected part of the beam.

structure (between v_1=1.7 km/s and v_2=2.2 km/s) of the two dimensional ion distribution is $\langle\cos^2\theta_{2D}\rangle = 0.935(1)$. The radial structures in the ion images indicate that there are two fragmentation channels present in the Coulomb explosion of iodobenzene: the inner ring corresponds to I^+ recoiling from a singly charged phenyl, whereas the outer ring corresponds to I^+ recoiling from doubly charged phenyl [101]. Using the outer ring for the determination of $\langle\cos^2\theta_{2D}\rangle$ is favorable as it corresponds to the most sudden fragmentation channel and, therefore, to the best axial recoil conditions. The derived value underestimates the degree of alignment since the probe and alignment pulse have perpendicular polarization and, therefore, the least-aligned molecules are ionized with the highest efficiency [54].

A slightly higher degree of alignment is obtained when the valve is operated at 100 Hz repetition rate. The degree of alignment with the deflector off at 100 Hz repetition rate is comparable to the one obtained at 1 kHz repetition rate in the deflected beam. A slight increase of the degree of alignment to $\langle\cos^2\theta_{2D}\rangle = 0.942(1)$ is observed in the deflected part of the beam at 100 Hz repetition rate. In order to investigate the reason for this behavior we have operated the valve at 100 Hz at a higher temperature and leaked helium gas into the chamber. Both, temperature and source chamber pressure, have been adjusted to match the conditions found at 1 kHz repetition rate. Under these conditions we observed a degree of alignment that matches the 1 kHz results. Therefore, the slightly smaller degree of alignment is attributed to a higher valve temperature and a higher background pressure in the source chamber when the valve is operated at 1 kHz. The lower peak intensity of the employed alignment pulse is the reasons for the smaller value of $\langle\cos^2\theta_{2D}\rangle$ compared to previous reported best value obtained using a 20 Hz 10 ns injection seeded Nd:YAG

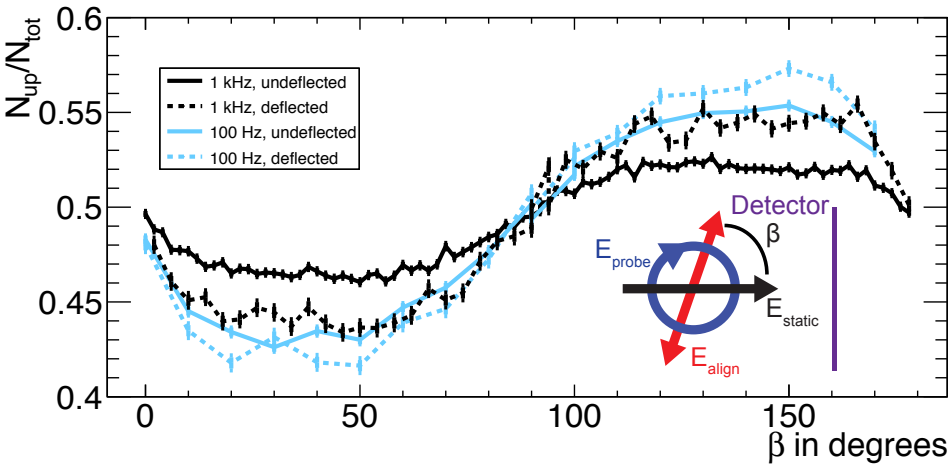

Figure 3.8: (Color online) The ratio N_{up}/N_{tot} as a function of the angle β. The color scheme is as in Figure 3.7 a). The inset shows the definition of the angle β. The typical time scale of one full β-angle scan at 1 kHz is in the order of 1000 s.

laser [50]. Obviously, these experimental limits could be solved by exploiting higher-power lasers and considerably larger vacuum pumps, which have not been available for this study. The pulse length of the alignment pulse is 450 ps. The rotational period of iodobenzene (J-type revival) is 707.7 ps [102, 103]. Thus, the laser pulse length is shorter than the rotational period of iodobenzene, placing this study in the intermediate regime between adiabatic and impulsive alignment – closer to the adiabatic case. The observed degree of alignment clearly indicates comparable control as in previously reported adiabatic alignment experiments [50, 101]. The detailed influence of non-adiabatic effects for the studied system is not clear and a more detailed investigation of the alignment dynamics as a function of the laser pulse duration is in preparation.

Figure 3.8 shows the ratio of ions in the upper half of the detector images divided by the total number of ions N_{up}/N_{tot} as a function of the angle β. The color scheme is as in Figure 3.7a). The angle β is defined as the angle between the polarization of the alignment laser and the static electric field of the VMI spectrometer, $E_{static} = 840$ V/cm, as shown in the inset of Figure 3.8. The probe beam is circularly polarized. The observed dependence of the orientation as a function of the angle beta is as expected from previous low-repetition rate experiments [50, 72]. The molecules are better oriented in the deflected part of the beam, where the population is confined to the energetically lowest, i. e., the most polar, rotational states. In addition we observe better orientation at 100 Hz than at 1 kHz repetition rates. The reason for this is the slightly increased rotational temperature of the 1 kHz molecular beam, as discussed above. In comparison with the orientation for the same molecule obtained using 10 ns alignment-laser pulses [50] we obtain a considerably smaller degree of orientation in the current experiment. This can be attributed to the nonadiabatic mixing of levels in the near-degenerate doubles created by the strong laser field, which has been shown to be more prominent for shorter laser pulses [80]. This

is also in agreement with earlier theoretical studies that have shown that the degree of impulsive orientation, using short laser pulses, is limited by the magnitude of the applied DC electric field [104].

3.2.4 Molecular-beam deflection dependence

In Figure 3.9 the vertical molecular beam profiles (Figure 3.9 c) and the dependence of the degrees of alignment (Figure 3.9 a) and orientation (Figure 3.9 b) on the position in the molecular beam, measured in a single lens scan as described above, are shown. The color scheme of the plots is the same as in Figure 3.7a). The molecular beam profiles and the observed deflection, for an applied deflector voltage of 12 kV, are in good agreement with previous measurements [72]. For the beam with the deflector off, the observed degrees of alignment and orientation are practically constant over the main part of molecular beam profile. Towards the sides, however, the achievable control decreases, which is especially pronounced for the alignment measurement. This demonstrates that the molecular beam is considerably warmer at the sides than in the center. This is attributed to collisions with the rest gas and to interference with mechanical apertures, i. e., skimmers. When applying an inhomogeneous electric field, the molecules are deflected upwards. Moreover, the molecular beam is dispersed according to the molecules' effective dipole moments, or, correspondingly, according to their rotational states. The most polar, lowest-energy rotational states are deflected the most, and this is reflected in the increased degrees of alignment and orientation in the deflected part of the molecular beam. This accounts for the larger contributions of lower quantum states which show a large deflection. In addition, a decrease of the degree of alignment and orientation in regions where the high rotational states remain (right part of the molecular beam profile) is observed. Helium is not present anymore in the deflected part of the molecular beam since its trajectory is not influenced by the electric deflector. As the degree of alignment and orientation is dependent on the position in the dispersed molecular beam, the properties of the beam change as a function of the vertical laser probe position.
This opens up the possibility for advanced multidimensional investigations, i. e., the observation of state-selective dynamics, in the future. It can also be used to increase the understanding of the deflection process of complex molecules, including the investigation of nonadiabatic couplings of rotational states by the "slowly" changing electric fields. Moreover, it enables the study of the nature of ensembles of molecules in a single molecular quantum states in mixed fields, as in a previous study on impulsive alignment and mixed-field orientation of a nearly pure ground state ensemble of OCS [41, 80].

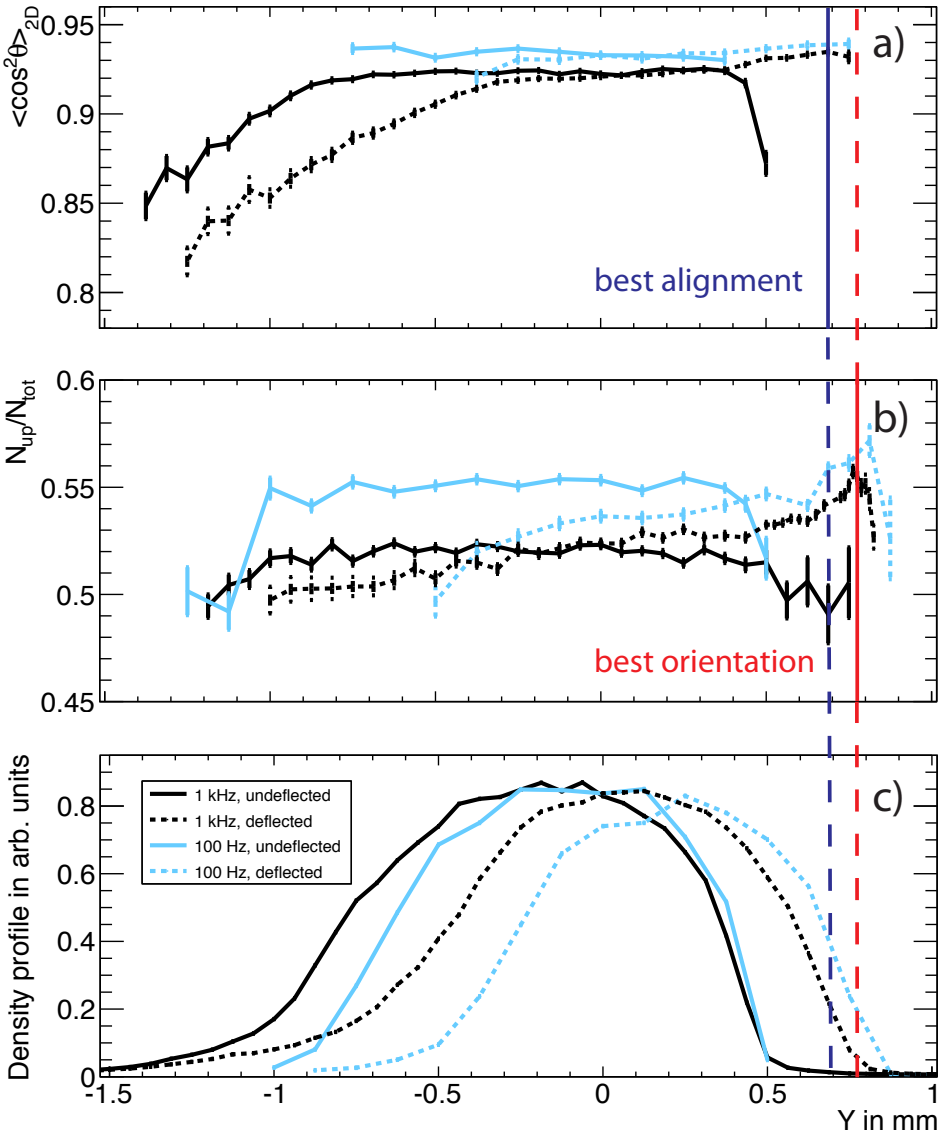

Figure 3.9: (Color online) The degree of alignment (a), the ratio N_{up}/N_{tot} (b) and the molecular beam density (c) as a function of the position in the molecular beam. The color scheme is as in Figure 3.7a). The positions for the best alignment and orientation are marked by vertical lines. The time for the data acquisition at 1 kHz for a single curve is in the order of half an hour.

3.2.5 Conclusions and Outlook for controlled molecules apparatus

In conclusion, a high-repetition-rate experimental molecular physics setup has been developed. It allows the preparation of very strongly aligned and oriented samples of quantum-state-selected cold molecules at a 1 kHz repetition rate. The dependence of the degree of alignment and orientation on the position in the molecular beam has been analyzed. Both parameters are enhanced when probing the state-selected molecules in the deflected part of the beam. A maximum degree of alignment at 1 kHz of $\langle\cos^2\theta_{2D}\rangle = 0.935$ has been obtained for a 450 ps long pulse with a peak intensity of 0.42×10^{12} W/cm^2. The obtained degree of orientation is $N_{up}/N_{tot} = 0.56$. This value is lower than what was demonstrated in previous studies [50], and it is limited by the combination of the applied DC electric field in the VMI spectrometer and the pulse duration of the alignment pulse, in accordance with previous analyses [80, 104].
The pulse duration of our alignment pulse is continuously tunable over a wide range from <50 fs to >500 ps; this will allow the investigation of the influence of this duration on the (non)adiabaticity on the alignment and orientation [80]. Preliminary measurements show that the degree of alignment is increasing when the pulse duration is shortened, due to the stronger peak intensity available in our setup. At the same time, revivals structures start to appear, indicating clear nonadiabatic effects in the alignment dynamics. It is likely that for each molecular sample a trade-off between adiabatic and non-adiabatic driving of the alignment can be found to ensure an optimal degree of alignment and orientation.
The demonstrated strong control over molecules at high repetition rates promises the feasibility of novel investigations of "weak" processes, such as chemical dynamics, using molecular-frame photoelectron angular distributions, photoelectron holography, or X-ray or electron diffraction imaging. For the applied, relatively short, alignment laser pulses, only moderate pulse energies, on the order of 10 mJ are necessary. It is envisioned that such pulses will be available at hundreds of kHz or even MHz repetition rates in the near future. For instance, similar setups are envisioned for the European XFEL, where burst mode lasers with similar pulse energies are under consideration and electric state selectors can be implemented for arbitrary repetition rate molecular beams. This opens up the possibility of performing time resolved dynamics studies using molecular frame photoelectron angular distributions [13] or photoelectron holography [93, 105]. Moreover, the controlled samples serve as ideal targets in x-ray or electron diffraction experiments [35, 38, 92], and they hold great promise toward attosecond and high-harmonic-generation experiments of complex molecules, where the molecular alignment and orientation can be exploited to modulate and enhance the output [106]. Moreover, the state-selection process inherently separates structural isomers [44, 46], which is a necessary ingredient to investigate ultrafast dynamics of structural isomers, such as charge migration in various conformers of glycine [107].

4 Electron source development

This chapter describes the developed electron source for time-resolved diffraction experiments. The first section starts with the theoretical description of the electron generation by photo-emission and provides some expressions for beam properties. In the following section, a basic setup is presented for preliminary tests on photo-emission without electron beam focusing. The third section elaborates on the electron source developed within this work. The requirements of diffraction experiments on controlled gaseous samples are given and the gun's suitability for these experiments is examined. The source featured a velocity-map imaging spectrometer that allowed to characterize the electron pulses in combination with electron trajectory simulations. Electron diffraction off a thin aluminum foil illustrated the coherence and the resolution of the setup. The last section discusses the the operation of the electron gun in perspective of diffraction experiments with controlled molecules. Achievable signal-to-noise ratios with the gun in these experiments is discussed and was significantly improved by background reduction. Moreover, qualitative simulations and experimental data were used to define the focusing voltage settings for experiments on aligned molecules with small interaction volumes.

4.1 Electron pulses and their properties

4.1.1 Electron generation by photo-effect

Generating electrons by light from a cathode is based on the photoelectric effect [108]. A strong electric field can be applied between the cathode and an anode to assist the emission [109]. If a pulsed laser is used the electron beam may be pulsed as well. The emission of electrons from metal surfaces by one-photon process can be described by Spicer's three-step model [110].
In the first step an incident photon can be absorbed by the cathode material, which is determined by reflectivity and absorption properties of the material at the given wavelength and polarization. Then, the excitation of an electron depends on the energy of the photon and the electron. The electron's distribution of occupied states is given by the Fermi-Dirac function. While the electron drifts to the surface it can scatter with other electrons. In the third step the electron overcomes the potential barrier and leaves the cathode material. The potential barrier is lowered due to the applied electric field by the Schottky effect.

The effective work function is given by

$$\phi_{\text{eff}} = \phi_w - \phi_{\text{Schottky}} = \phi_w - e\sqrt{e\frac{e\,F_a}{4\,\pi\,\epsilon_0}} \tag{4.1}$$

with the work function of the material ϕ_w and the applied electric field F_a. The combination of all three steps allows for the calculation of the electrons' angular momentum spread when they exit the cathode. It can be used for beam quality determination as described in the next section [109].
If the energy of the photon is below the electron's binding energy, intense laser light can be used for multi-photon emission. In this case more than one photon have to be absorbed at the same time to provide the electron with enough kinetic energy to escape the material. The emitted charge then scales in a non-linear way with the laser intensity [111, 112].

4.1.2 Coherence

The diffraction theory in chapter 2 assumed perfect coherence of the electron beam. This is not the case in experiments. The transverse coherence length is given by

$$L_c = \frac{\lambda}{2\pi\sigma_\theta} \tag{4.2}$$

with the De Broglie wavelength λ and the root-mean-square (RMS) angular spread in momentum $\sigma_\theta = \sigma_{px}/\sigma_{pz}$ [113, 114]. The transverse coherence length describes the spatial limitations of the coherence that lead to a broadening of the modulations in I_{mol} on the detector [115]. If the coherence length becomes smaller than the imaged structure, the interference terms between different atoms cannot be summed coherently in the scattering intensities (equation 2.14).
The coherence length can be expressed as a function of the transverse normalized emittance of the electron beam $\epsilon_{n,x}$, which is commonly used to describe the transverse beam quality. The product of the emittance in all three dimensions corresponds to the phase-space volume of the electron pulse. At the electron beam's waist, the normalized thermal emittance can be written as

$$\epsilon_{n,x} = \frac{\sigma_x \sigma_{px}}{m_e c} \tag{4.3}$$

with the electron RMS beam size σ_x and the RMS momentum spread in the same dimension σ_{px} [114]. The coherence length can then be expressed as a function of the emittance and the spot size

$$L_{c,x} = \frac{\hbar\,\sigma_x}{m_0\,c\,\epsilon_{n,x}}. \tag{4.4}$$

The coherence length will decrease with decreasing electron beam size for a constant emittance. The lower the emittance, the higher is the electron beam quality. In the here presented experiments, the emittance was defined during the emission of the electrons

at the cathode and by space charge interaction. During free flight the total emittance remains constant. For photo-emission from a metal cathode the normalized emittance is

$$\epsilon_{n,x} = \sigma_x \sqrt{\frac{E_{\text{phot}} - \phi_{\text{eff}}}{3\, m_0\, c^2}} \tag{4.5}$$

with the photon energy E_{phot} and effective work function ϕ_{eff} [109].
A longitudinal emittance and coherence length can be calculated for the electron pulse. Often, the energy spread σ_E within the electron beam is given instead. With energy of the electron the electrons' wavelength changes. This results in a different scattering angle for a constant s. This variation in angle will broaden the diffraction pattern.
The finite coherence length and the energy spread lead to a broadening of the diffraction pattern structures. Partially coherent diffraction patterns still contain information of the molecular structure, but the contrast decreases. If the modulation amplitude in radial plots (for example in Figure 2.5) reduces below the incoherent background, the amount of retrievable information on the molecular structure decreases.

4.2 Preliminary tests on electron generation

According to subsection 2.3.2, $N_e = 10^6$ electrons per pulse would be needed for electron diffraction experiments on controlled molecules samples provided by the apparatus described in section 3.2. A setup for basic tests on electron emission is depicted in Figure 4.1. The aim of these experiments was to determine parameters under which $N_e = 10^6$ to 10^7 electrons could be generated per pulse in a stable way. The setup consisted of a copper cathode and an anode with a hole diameter of 2 mm. The steel electrodes were electro-polished to avoid local field enhancement. The distance between cathode and anode was 14 mm. The maximal cathode voltage was $U_c = -20\,\text{kV}$ and the anode was grounded. It was planned to use an electrostatic lens, which would allow for an extraction field corresponding to $U_c \approx -4\,\text{kV}$ in this basic setup. The probe laser from the apparatus in section 3.2 with a central wavelength of 800 nm was used for generation of electrons by multi-photon emission.
The laser was focused onto the cathode with a spot size of $\sigma_x = 55\,\mu\text{m}$ and $\sigma_y = 22.5\,\mu\text{m}$. Due to an incident angle of $70\,^\circ$ one dimension of the laser spot on the cathode, σ_x, was broadened to $\sigma'_x = 165\,\mu\text{m}$. The pulse duration d_L (FWHM, full-width-half-maximum of the laser pulse duration approximated as gaussian) was adapted by an internal compressor of the laser system and measured by autocorrelation. The electron number was measured by a Faraday cup that was connected to an electrometer (section 4.3).
The aim was to achieve $N_e = 10^6$ electrons emitted per pulse for $U_f \approx -4\,\text{kV}$ without damaging the cathode. The damage threshold for copper is a few $100\,\text{GW/cm}^2$ for sub-ps pulses with 800 nm light [112]. In order to not damage the cathode the intensity was not increased beyond this intensity, but the laser pulse energy was increased by using longer laser pulses at the maximum peak intensity.

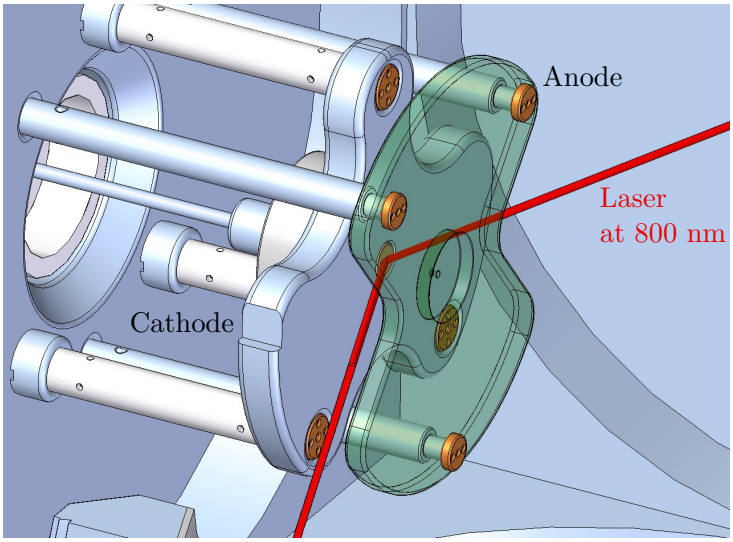

Figure 4.1: Basic setup for experiments on electron generation. A laser with central wavelength of 800 nm was focused on the copper cathode. Voltages up to -20 kV were applied to the cathode, while the anode was grounded.

Measurements were performed at different pulse durations d_L, pulse energies W and cathode voltages U_c. The summary is shown in Table 4.1. The resulting laser peak intensity was calculated by

$$I = \frac{W}{2\,\pi\,\sigma'_x\,\sigma_y\,d_L}. \tag{4.6}$$

For the shortest tested pulse duration of 50 fs the amount of electrons did not exceed 10^6 for $U_c = -4\,\mathrm{kV}$. The number of electrons could not be increased by employing a higher laser intensity as the corresponding intensity of $111\,\mathrm{GW/cm^2}$ was already close to the expected damage threshold. For this intensity, the number of emitted electrons could be increased by applying a stronger extraction field, which lowers the potential barrier by the Schottky effect (equation 4.1) and reduces charge effects [112, 116] (see also subsection 4.4.3). With $U_c = -20\,\mathrm{kV}$ the created electron number was increased by more than a factor of two. For technical reasons the corresponding extraction field was not feasible in combination with the planned electrostatic lens (the final setup is discussed in section 4.3).
A longer laser pulse duration with a similar peak intensity was assumed to increase the electrons per pulse, as the electron beam stretching in longitudinal direction would allow for a longer illumination with the same intensity. The laser power and pulse duration were increased by approximately 4 to keep the peak intensity constant or lower. With $d_L = 200\,\mathrm{fs}$ more electrons could be generated per pulse. Therefore, the approach was assumed to work well. The pulse duration was further increased to $d_L = 5\,\mathrm{ps}$. At $W = 25\,\mu\mathrm{J}$ a severe breakdown between cathode and anode occurred. The cathode was damaged, which could be observed by visual inspection. The polished surface probably suffered from damage by heating from the laser. This lead to a local field enhancement and triggered the breakdown.

d_L (fs)	$W(\mu\mathbf{J})$	I ($\mathbf{GW/cm^2}$)	U_c (kV)	electrons/pulse
50	1.3	111	-20	$1.5 \cdot 10^6$
50	1.3	111	-4	$5 \cdot 10^5$
200	4.2	90	-20	$3 \cdot 10^6$
200	4.2	90	-4	$8 \cdot 10^5$
5000	25	21	-20	breakdown

Table 4.1: Summary of electron emission generated by a laser with central wavelength of 800 nm. With increasing pulse duration d_L the pulse energy W was raised by a similar factor. In this way, the peak intensity I was kept the same. The electron number per pulse could be increased until a breakdown occurred.

In order to ensure the stable production of 10^6 electrons the laser setup was changed to produce laser pulses with a central wavelength of 266 nm. At this wavelength only one photon is necessary to overcome the work function of copper and hence a lower intensity would be sufficient. Moreover, the anode was exchanged with an electrode configuration for acceleration and focusing. The setup and its properties are described in the next section.

4.3 Electron gun for diffraction experiments off controlled molecules[1]

4.3.1 Introduction to electron sources

The first sources for creating electron pulses short enough to study ultrafast processes in molecules or materials were dc electron guns. Here, electrons were created from metallic surfaces by short laser pulses and accelerated in dc electric fields [19, 20], yielding sub-picosecond electron pulses of moderate coherence and brilliance. Radio-frequency cavities allow for temporal compression of electron pulses through phase-space rotation, shortening the pulse duration to below 100 fs with electron numbers of 10^6 per pulse and electron spot sizes below 100 µm [117]. Compact dc guns can achieve comparable properties by increasing the acceleration fields and reducing the path length, during which the electron pulse can expand [113, 118–120]. Ultra-fast-single-electron sources [121] avoid the problem of space charges, but rely on very high repetition rates to achieve sufficient electron fluxes for diffractive imaging experiments. The use of ultra cold atoms as electron sources increases the coherence [122, 123]. Other possible sources for time-resolved electron diffraction are

[1] This section is based on the paper *Electron gun for diffraction experiments off controlled molecules*, N.L.M Müller, S. Trippel, K. Długołęcki, J. Küpper, *Journal of physics B* **48**(24), 244001 (2015).
Together with S. Trippel I planned the apparatus. This included the discussed simulations and calculations. I setup the apparatus, conducted the experiments and performed the data analysis. Together with the other authors, I discussed the results and wrote the published article.

low energy electron setups [124] or laser-induced electron diffraction [125, 126].
If the molecular samples are prepared in the necessary strongly-controlled fashion, their densities are typically on the order of some 10^8 molecules/cm^3 [36, 127]. Assuming Rutherford scattering, for the prototypical molecule 2,5-diiodobenzonitrile an effective cross section on the order of 10^{-15} cm^2 can be derived for our experimental geometry and a beam stop blocking a solid angle of 1.3×10^{-3} sr. To align or orient the molecules, they are typically exposed to laser fields with intensities of 1 TW/cm^2 [49], which can be achieved by focusing the ps-duration mJ-pulse-energy laser beam to 100 µm [128]. For a 500 µm thick molecular beam this results in an interaction volume of about 5×10^{-6} cm^3. The number of molecules in this volume and the given cross section lead to an elastic scattering signal on the detector $S_{elastic}$ of 5×10^{-9} per electron. In order to achieve a diffraction pattern containing some 10^5 scattered electrons on the detector within 24 hours, bright electron sources with 10^9 electrons per second are needed. For experimental repetition rates on the order of 1 kHz [128], this corresponds to 10^6 electrons per shot with an electron beam focus size of approximately 100 µm. The setup presented here produced the necessary electron numbers and allowed for a characterization of the electron beam to ensure, for instance, the required transverse coherence length.

4.3.2 Experimental setup

A schematic of the experimental setup is shown in Figure 4.2. The electrons were photo-emitted from a copper cathode *via* one-photon absorption after irradiation with short UV laser pulses. The pulses were generated by third-harmonic generation (THG) of 30-fs-duration near-infrared pulses from a Ti:Sapphire laser (TSL) system with a repetition rate of 1 kHz. Based on the pulse duration of the near-infrared laser pulse at the THG setup, and the dispersion in subsequent optical elements, we estimated a pulse duration of 370 fs for the UV light. The central wavelength was 265 nm with a spectral width of 4 nm. The light enters and exits the chamber through anti-reflection coated windows. The pulse impinged on the cathode under an angle of $70\,^\circ$ to the surface normal of the cathode. The electrons were accelerated and focused by three electrodes in velocity-map imaging spectrometer (VMI) configuration. The applied potential at the cathode was $U_c = -15$ kV. The voltage on the focusing electrode was varied between $U_f = 0$ kV and -15 kV. The third electrode was kept on ground potential. The asymmetric electrode shape allowed the laser beam to pass and impinge on the cathode. The holes within the electrodes were large enough to avoid clipping of the electron beam. On the one hand this reduced the background signal in diffraction experiments, as there was no electron scattering off the electrodes. On the other hand it allowed for steering the electron beam's position by changing the laser-spot position on the cathode. The voltage on the focusing electrode U_f determined the position of the electron beam focus along the z direction. The electrode configuration allowed to characterize the electron pulse by applying the corresponding voltages for spatial- and velocity-mapping [85, 88, 129]. It is possible to create electric fields that allow to either map the spatial distribution of the electrons at the cathode or their

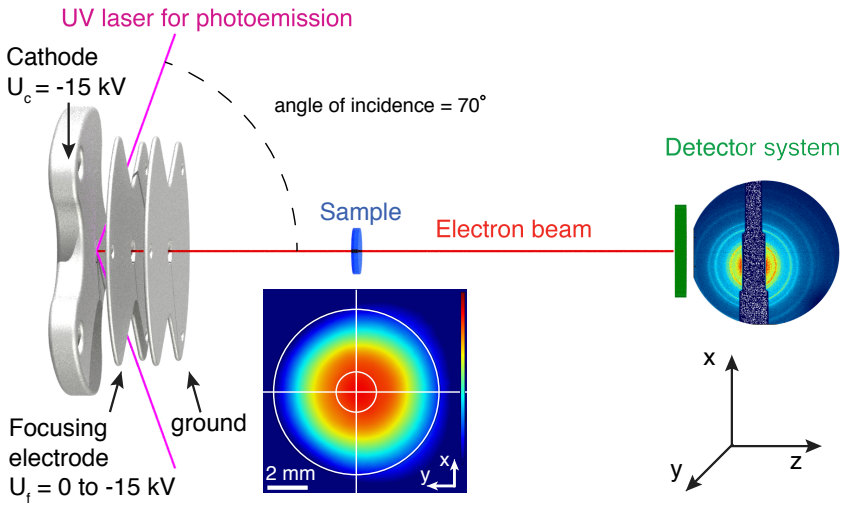

Figure 4.2: Experimental scheme of the electron gun consisting of three electrodes in velocity-map-imaging-spectrometer configuration. After photoemission, the electrons were diffracted of an aluminum sample or were measured by a Faraday cup coupled to an electrometer. A multi-channel-plate detector with phosphor screen and a camera was used for position sensitive detection. The inset at the bottom depicts the potential between cathode and focusing electrode. To highlight the asymmetry the $x = 0$ and $y = 0$ axes as well as centered circles are shown to guide the eye.

respective velocity distribution as a 2D projection onto the detector [85, 88]. The spatial distribution of the electron beam was recorded by a position sensitive detector consisting of a multi-channel-plate (MCP) with a phosphor screen and a CMOS camera (Optronis CamRecord CL600x2). The detection system was read out with a 1 kHz repetition rate, which allowed for single electron counting in the case of a few electrons per pulse. At large electron numbers, the gain of the detector had to be reduced to avoid damage of the MCP. With lower gain single electrons could not be resolved anymore. In order to reduce background from scattered light or other sources the detector can be gated. A Faraday cup connected to an electrometer (Keithley 6514 electrometer) was used to measure the electron number per pulse. To further characterize the electron pulses, we performed diffraction experiments with a thin aluminum foil on a TEM grid, which was introduced into the electron beam path. In this case the direct electron beam was blocked by a copper or aluminum beam block.

4.3.3 Electron gun properties

The electron gun was designed for ultra-high vacuum. Here, the final pressure was 4×10^{-9} mbar using a turbomolecular pump with pumping speed of 300 l/s, limited by outgassing from the cable of the Faraday cup and from PEEK material of the electron-gun insulators. This low pressure is essential when investigating thin gas-phase samples in

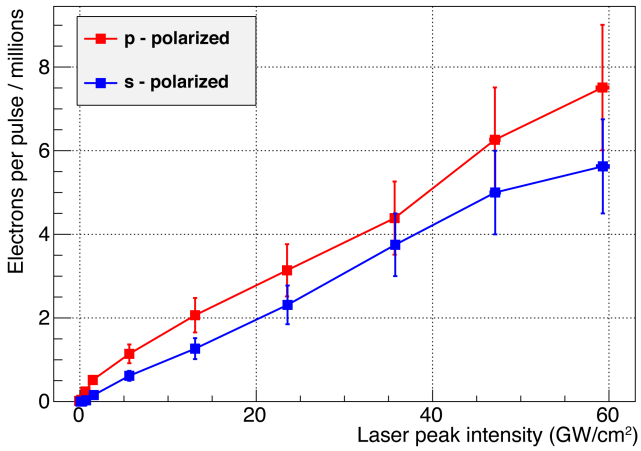

Figure 4.3: Electron number as a function of laser peak intensity for p-polarized (red) and s-polarized (blue) laser light and a central laser wavelength of 265 nm.

order to reduce the scattering by background gas. We expect to achieve pressures of a few 10^{-10} mbar in the final setup when replacing all PEEK insulators by MACOR or alumina. In Figure 4.3 the electron number per pulse is shown for $U_f = -13.2$ kV as a function of the laser pulse intensity for two laser polarizations. This focusing voltage corresponded to the focus of the electron beam being close to the detector surface. The number of electrons increased linearly with the laser power, as expected for a one-photon effect of 265 nm light with a spectral width of 4 nm on copper, which has a work function of 4.7 eV. No saturation was observed. The number of generated electrons depended on the laser polarization: For p-polarization (red curve, field vector in plane of incidence) more electrons were generated than for s-polarization (blue curve, field vector parallel to cathode surface). This is in accord with the reflectivity of copper being higher for s-polarized light than for p-polarized light, which was confirmed by measuring the laser power for both polarizations after the cathode. Up to 8×10^6 electrons per shot could be obtained, which is sufficient for the planned diffraction experiments on dilute gas-phase samples delivered by the controlled-molecules apparatus.

For a full characterization of the electron beam the electron spot size at the detector was measured for various focusing voltages U_f, including those for spatial- and velocity-mapping. In Figure 4.4 a the root-mean-square (RMS) spot size of the electron beam in x and y dimension, σ_x and σ_y, are plotted as a function of U_f. Here, the laser intensity was reduced to less than 10 MW/cm^2 to create approximately five electrons per pulse from the cathode and, therefore, space charge effects were negligible. The spot size decreased with increasing U_f until it reached a focus, at the detector, for about $U_f = -13$ kV. Raising U_f further led to a defocusing of the electron beam, i. e., the focus was placed before the detector. The exact voltage to place the focus onto the detector depends on the initial size of the electron cloud. The electron beam was broadened in x direction due to the large angle of incidence of the laser. Therefore, the foci in x and y dimension had slightly

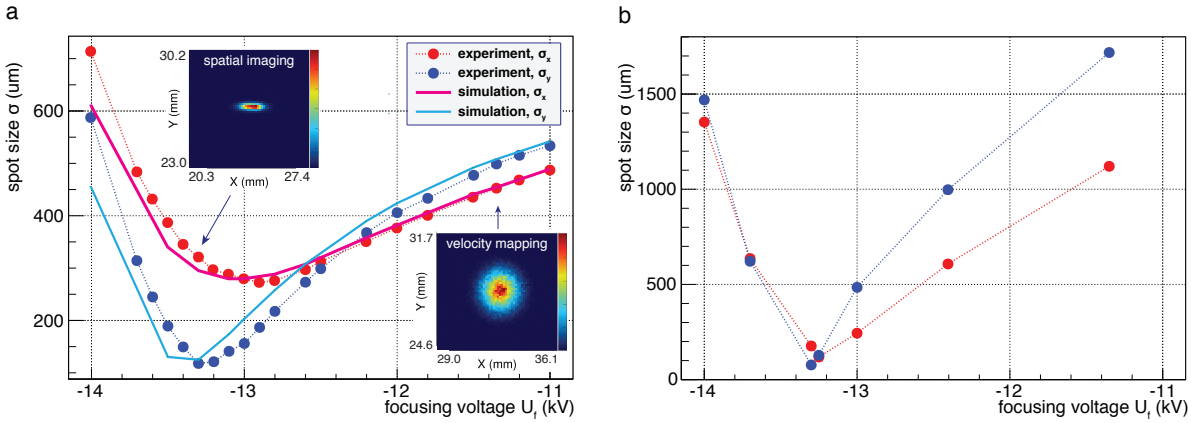

Figure 4.4: Electron spot size on the detector for different focusing voltages for (a) a few and (b) 2×10^5 electrons per pulse. Red and blue dots are experimental results corresponding to x and y directions, respectively. Magenta and cyan lines correspond to corresponding simulations in x and y dimension. The insets in (a) show detector images for spatial (left) and velocity map imaging (right).

different focusing behavior.

In spatial imaging mode, $U_f = -13.3$ kV, the spatial distribution of emitted electrons was mapped onto the detector, which is depicted as inset in Figure 4.4 a. In this case, all electrons, which started from a certain coordinate on the cathode hit a corresponding point on the detector, in first order independent of their momentum [88]. The magnification factor m_s for spatial imaging was calibrated in the experiment by translating the laser-focus spot on the cathode using the focusing lens. From a known displacement of the electron beam on the cathode Δx_C and the corresponding measured displacement of the electrons on the detector Δx_D a magnification factor of $m_s = \Delta x_D / \Delta x_C = 3.9$ was determined. This agreed with the simulated value. For simulations of electric fields and trajectories finite-element methods were used (COMSOL Multiphysics). The inferred RMS sizes of the electron beam at the cathode were $\sigma_x = 85(3)$ µm and $\sigma_y = 31(1)$ µm; values in parenthesis depict one standard deviation. The difference in spread originated from the laser impinging on the cathode under an angle of incidence of 70 °. The angle lead to an effective broadening of the photoemission laser by a factor of approximately three in x direction, while the y dimension was unchanged. Thus, the created electron beam was broader in x direction than in y direction on the cathode, which was confirmed in the spatial imaging measurements.

In velocity map imaging mode ($U_f = -11.35$ kV) the transverse velocity distribution was mapped onto the detector, which is shown as the second inset in Figure 4.4 a. The velocity spread was similar in both dimensions. With the simulated magnification factor of $m_v = 0.9$ for velocity mapping and a simulated electron time of flight of 4.1 ns an energy spread of $\sigma_E = 0.1$ eV was obtained. This agrees well with the previously reported value $\sigma_E = 0.13$ eV [130].

In order to characterize the electron beam further simulations and measurements at various focusing voltages U_f were performed. The spatial and velocity distribution of the electrons in x and y dimension could be retrieved from the experiment, but the corresponding values in z dimension had to be simulated. Electric fields were calculated using finite-element methods (COMSOL Multiphysics) and the electron trajectories in these fields were simulated using ASTRA [131]. The initial spatial distribution at the cathode was taken from the measurements described above. Together with a Fermi Dirac distribution for the one-photon emission, this led to the emittance values of $\epsilon_x = 0.026\ \pi\,\mathrm{mrad\,mm}$ and $\epsilon_y = 0.010\ \pi\,\mathrm{mrad\,mm}$, and the energy spread in z-direction of $\sigma_{E_z} = 0.2$ eV. Fitting the emittance to the transverse velocity distributions retrieved from VMI mode, while keeping σ_{E_z} constant, resulted in $\epsilon_x = 0.029\ \pi\,\mathrm{mrad\,mm}$ and $\epsilon_y = 0.012\ \pi\,\mathrm{mrad\,mm}$, in good agreement with the values obtained from the Fermi Dirac distribution. Using the fitted input parameters, the overall dependence of the electron beam spot size at the detector on the focusing voltage was simulated. The results are depicted by the magenta and cyan lines in Figure 4.4 a and are, again, in good agreement with the experimental results. This indicates that also the simulated σ_{E_z} was sensible. Due to the good agreement between experiment and simulation it is possible to deduce properties of the electron beam from the simulations, including size, coherence length and pulse duration, for its whole propagation. The coherence length $L_c = \hbar\,\sigma_x/(m_0\,c\,\epsilon)$, with the electron mass m_0 and the speed of light c, was determined using ASTRA [131]. At the sample position (11 cm downstream from the cathode) L_c was deduced to be 3 nm in x-dimension and 1.2 nm in y-dimension. The pulse duration at this position was simulated to be 1.4 ps.

Figure 4.4 b shows the spot sizes for 2×10^5 electrons per pulse, where space charges had a significant effect. For the detection of 2×10^5 electrons per pulse in Figure 4.4 b, the detector voltage had to be reduced and single electron detection was not possible. This implies that Figure 4.4 a and b are only qualitatively comparable. A stronger asymmetry in velocity map imaging mode was observed than above. This could not be reproduced using a cylindrical symmetry in electric fields and initial velocities, which was a good approximation in the simulations for few electrons. Using finite-element simulations it was possible to qualitatively determine the origin of the asymmetry in the velocity map imaging mode, but a full simulation of all 3D trajectories for 2×10^5 electrons was not possible due to too high computational cost. Simulations for few electrons showed that the trajectories of the electrons far off the central axis of the spectrometer were disturbed by the asymmetry of the electric field due to the opening in the electrodes, see inset in Figure 4.2. This became more pronounced when space charges lead to a significant broadening of the electron distribution. In the case of 2×10^5 electrons per pulse the radial distribution between the cathode and the focusing electrode was increased by an order of magnitude compared to the few electron case. This lead to a larger magnification factor in vertical direction in velocity map imaging mode and, therefore, contributed to the asymmetry in the detector image. Secondly, the space charge effect itself lead to an asymmetry in the velocity distribution, if the electron spot was asymmetric. For an ellipsoid with homogeneous charge density, the velocity in the direction of the shorter

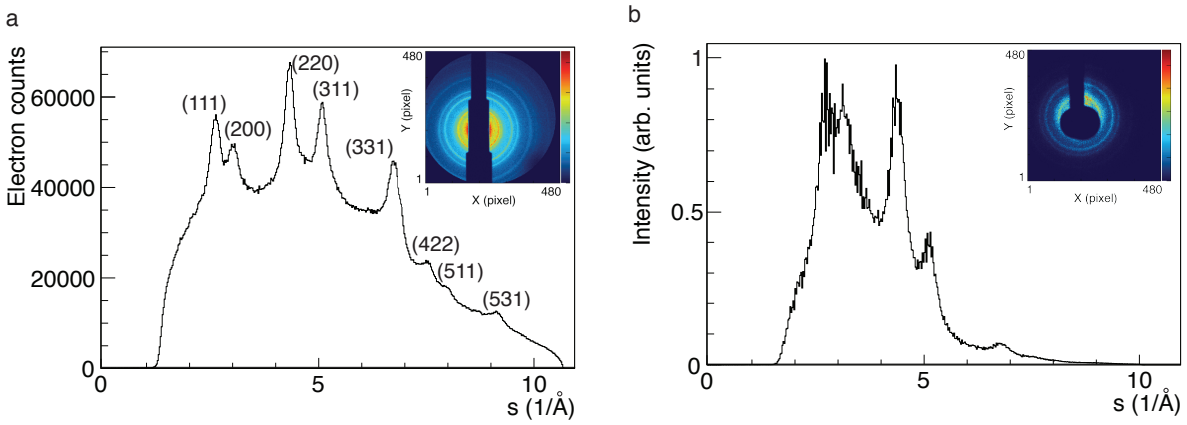

Figure 4.5: Radial scattering intensity for aluminum for (a) 10^3 and (b) 10^6 electrons per pulse. Peaks are labeled with Miller indices (hkl). The insets show the corresponding diffraction patterns.

axis is higher [132]. In our case, the velocity distribution along y direction was larger, as the size of the cloud is smaller in this dimension. Simulating similar electron densities in smaller, but asymmetric volumes showed an asymmetric velocity distribution as well. The velocity was higher in the direction of the smaller expansion, corresponding to the y direction in the experiment. Both effects resulted in the vertical broadening of the electron pulse in velocity-mapping mode.
Simulations in cylindrical symmetry (ASTRA) for one million electrons per pulse provided an approximate value for the pulse duration at the sample position of 60 ps. Albeit this was much longer than in the case of a few electrons/pulse, it is sufficiently short for the diffractive imaging of aligned and oriented molecules, which we can routinely create and control for hundreds of picoseconds [42, 128].

4.3.4 Diffraction off aluminum

A thin polycrystalline aluminum sample was used to test the electron-optical properties of the generated electron pulses, for instance, its coherence length and spatial resolution. The inset in Figure 4.5 a shows a diffraction pattern for 10^3 electrons per pulse averaged over 10^6 pulses, i. e., about 15 min at 1 kHz. The electron beam was focused on the detector, which resulted in a nearly collimated beam at the position of the sample. The typical diffraction rings of a polycrystalline sample were observed [14]. The corresponding radial distribution as a function of momentum transfer s is plotted in Figure 4.5 a. The peaks can be assigned to the allowed face-centered cubic crystal structure reflections for aluminum and the corresponding Miller indices (hkl) are used to label the peaks [14].
The inset in Figure 4.5 b shows a diffraction pattern averaged over 10^3 pulses ($\sim$1 s) with 10^6 electrons per pulse. A 6-mm-wide beam stop was used, but the MCP voltage still had to be reduced to avoid damaging the detector due to many electrons scattered to small

s. Reducing the MCP voltage reduces the gain of the detector system, i. e., the signal on the camera per impinging electron. With this lower gain single, or a few, electrons could not be detected anymore. Therefore, the peak intensities in Figure 4.5 a and b cannot be compared quantitatively. Diffraction peaks are still visible in Figure 4.5 b, except for the largest s where the electron number and the gain were too small. This implies that the transverse coherence of the electron pulses were larger than 234 pm, while approximately 1 nm was expected from simulations. The spatial resolution of the imaging experiment was better than 234 pm, the interatomic distance corresponding to the (111) reflection in the diffraction pattern of aluminum. The restriction in resolution due to the lower detector gain will not occur in the envisioned gas-phase experiments, as the sample density will be much smaller. Thus, single-electron detection will also be possible for large electron numbers per pulse.

4.3.5 Conclusion and outlook for electron source

Using the implemented spectrometer it was possible to experimentally obtain the emittance, i. e., the initial transverse spatial and velocity distributions of the electrons. The combination with simulations allowed for the deduction of further values, such as the coherence length and pulse duration of the propagated electron pulses. Compared to other sources with time resolutions on the order of 1 ps or below [19, 20], our setup did produce electron pulses with 1.5 ps duration for few electrons/pulse. More importantly, our table-top setup allows for a stable production of $> 10^6$ electrons/pulse at a repetition rate of 1 kHz with an estimated pulse durations of 60 ps. Nevertheless, due to the negligible cross-sections radiation damage can be neglected even on these long timescales. For the prototypical 2,5-diiodobenzonitrile molecule the effective electron-impact-ionization cross section is about 10^{-16} cm^2, whereas the effective elastic-scattering cross section is 10^{-15} cm^2. For 10^6 electrons per pulse, a molecular density of 10^8 cm^{-3}, and an interaction volume of 5×10^{-6} cm^3 the signal on the detector of electrons elastically scattered off an already destroyed molecule is $S^D \approx 0.5 \cdot S^D_{elastic} \cdot S^D_{ionized} = 0.5 \cdot 5 \times 10^{-3} \cdot 5 \times 10^{-4} = 1.25 \times 10^{-6}$ per shot [36]. This corresponds to a fraction of $P^D = S^D / S^D_{elastic} = 2.5 \times 10^{-4}$ electrons scattered off damaged molecules per elastically-scattered signal electron. Thus, radiation damage is not relevant in these experiments. Importantly, it is much smaller than in similar x-ray-diffraction experiments, where radiation damage was not necessarily negligible, but could be reduced by increasing the x-ray beam diameter [36].

The current setup could be improved by increasing the acceleration fields: This would simultaneously increase the electron number for the same laser power and lead to a smaller emittance and, thus, an increased coherence length of the electron beam. The time resolution could either be improved through a more compact design and stronger electric fields [119] or by combining the setup with an RF cavity for appropriate phase-space rotation for temporal focusing [113, 117, 133].

In conclusion, a new source for picosecond time-resolved electron diffraction experiments with the need for large numbers of electrons was described. It will allow, for instance, the

investigation of dilute samples of controlled gas-phase molecules [48]. Moreover, enabled by its velocity map imaging spectrometer geometry, the setup allowed to characterize the electron beam properties, e. g., the spatial and velocity distributions of the electrons. The focusing and coherence properties of the electron pulses were determined through both, simulations and diffraction experiments of aluminum-foil samples, to be sufficient for the envisioned atomically resolved controlled molecule diffractive imaging.

4.4 Further improvements and characterization

4.4.1 Background reduction

This section provides an analysis of the setup-related background signal and its reduction in comparison to the expected signal for diffraction experiments on DIBN in chapter 5. As discussed in subsection 4.3.1 the amount of scattered electrons is expected to be on the order of S_{elastic} of $5 \cdot 10^{-9}$ per electron. For 10^6 electrons per pulse this would yield $S_{\text{elastic, shot}} = 0.005$ per shot for DIBN. For experiments the noise due to background has to be low enough to allow for a detection of the small signal $S_{\text{elastic, shot}}$. A significant part of the background in diffraction experiments on controlled molecules was estimated to consist of the scattering signal from helium in the molecular beam. The effect of scattering due to this background gas cannot be avoided completely for experiments on molecules seeded in atomic gas. It is implemented in simulations in subsection 2.3.2. As discussed therein, the amount of helium can be reduced by deflection to allow for a signal-to-noise suitable for diffraction experiments on DIBN.
As preparation for the diffraction experiments with low scattering signal, further background sources were studied that were not related to the molecular beam. These were investigated in the electron source setup discussed above (section 4.3) by blocking the direct electron beam and introducing no sample into the beam path.
A high background signal was observed for a wavelength of 265 nm of the electron-generation laser: With 10^6 electrons per pulse in the blocked direct beam, the total background count was approximately $S_{\text{bg, shot}} = 120$ electrons per shot, which is 4 orders of magnitude higher than the expected scattering signal $S_{\text{elastic, shot}} = 0.005$ per shot for DIBN for the same electron number. In order to realize a suitable signal-to-noise this background had to be reduced. Two possible sources for the background were investigated to define the necessary steps for background reduction. The background could originate from scattering off rest gas in the chamber $S_{\text{rest-gas}}$ or from a background signal inherent to the electron gun apparatus S_{setup}.
The rest gas in the chamber without sample was considered to be mostly nitrogen. The scattering signal off nitrogen at a chamber pressure on the order of 10^{-10} mbar (pressure in experiments in chapter 5 without gas sample) was estimated from corresponding scattering cross sections and the electron flight path distances. It was close to the expected scattering signal off the molecule $S_{\text{elastic, shot}}$ and therefore much lower than the measured $S_{\text{bg, shot}}$. It was also tested experimentally if the rest gas scattering was responsible for the high

background level. Nitrogen gas was leaked into the chamber to increase the pressure from $9 \cdot 10^{-9}$ mbar to $4 \cdot 10^{-7}$ mbar. No increase of signal on the detector was observed for this pressure increase. It was deduced that rest gas scattering was not contributing with a significant part to the large background signal $S_{bg,\,shot}$.
The other possible source is the setup-related background summarized as S_{setup}. It contained photons, which probably originated from light scattering off laser windows and metallic surfaces in the vacuum chamber. It also included background-electrons, which could be parts of the electron beam being scattered off the beam block and electrons that are generated within the electron gun apart from the direct electron beam.
The ratio of photons and background-electrons was examined by varying electric fields within the test chamber. The cathode was operated at positive voltages to not accelerate any electrons towards the detector by the small electric field produced by the detector. In this case, the background – now only photons – was reduced but signals with a similar order of magnitude remained. Therefore, it was deduced that the background consisted of both photons and electrons to similar parts. Several approaches for the reduction of S_{setup} are discussed in the following. They included shielding, temporal gating and change of laser wavelength.
In order to reduce the background by shielding the detector from the background's source, the point of origin of S_{setup} had to be determined. Aluminum foil was used as shielding material. It was installed in the chamber to block all pathways for background-electrons and photons without cutting the electron beam path. This did not reduce the S_{setup}. Blocking the cathode-anode hole lead to a significant reduction of S_{setup}. The background therefore most likely passed the electrode-hole region and could originate from scattering of light or electrons from cathode or electrode edges. The origin of S_{setup} could not be determined to full conclusion and the detector could not be shielded from it without blocking the electron beam path. Therefore, the background had to be reduced by other means.
The temporal structure of S_{setup} was studied to determine if the background could be reduced by gating the detector on the electron beam signal. A fast high-voltage switch (Behlke) was used to switch the detector on for 150 ns with varying time delay. The count rates per shot as a function of timing between electron generation laser and detector gate are depicted in Figure 4.6 for an electron energy of 15 keV. In order to illustrate the ratio of signal $S_{\text{elastic, shot}}$ to background S_{setup} the measured signals were scaled to accord with the experimental conditions at 10^6 electrons per pulse. S_{setup} was measured for an electron number of $2 \cdot 10^5$ per pulse with the direct electron beam blocked. It was scaled linearly to a background corresponding to 10^6 electrons per pulse (violet curve). The direct electron pulse was recorded for a few electrons per pulse. It was scaled to the expected signal for 10^6 electrons per pulse, which is $S_{\text{elastic,shot}} = 0.005$ per shot (black curve). The expected signal is much lower than the background and had to be magnified by a factor of $4 \cdot 10^4$ for illustration (red curve). S_{setup} consisted of photons and background electrons as discussed above. The different arrival times are depicted in Figure 4.6 as blue-shaded (photons) and green-shaded (background-electrons) area. It has to be noted that the duration of

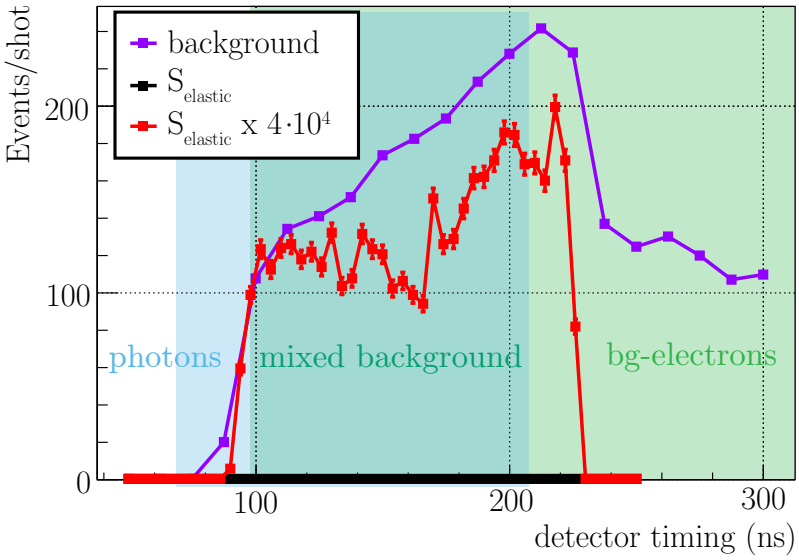

Figure 4.6: Event counts per shot for background (violet) and expected electron scattering (black) as a function of detector timing with 266 nm light for electron generation and the Behlke switch. Background and scattering signal are scaled to correspond to electron pulses with 10^6 electrons per pulse. For illustration the scattering signal is magnified by a factor of $4 \cdot 10^4$ (red). The shaded areas depict the composition of the background as a function of time: photons (blue), background electrons (green) and mixed background.

the detector signal was determined both by the original signal and the switch's opening time of 150 ns. The temporal profiles showed that background-electrons, photons and electron beam overlapped in time. Comparing the violet and red curve in Figure 4.6, it was observed that the expected signal was at least $4 \cdot 10^4$ times lower than S_{setup} at any point in time. The measured background level would not allow for the necessary signal-to-noise by detector gating alone.

Background reduction by more than three orders of magnitude was achieved by the combination of laser setup change and detector gating. At first, the photon background was reduced by changing the wavelength for electron generation. The remaining background-electrons were cut off by gating the detector on the electrons using a switch with a shorter fall time.

The used MCP was sensitive to $\lambda = 265\,\text{nm}$ light, but the detection efficiency reduced by approximately one order of magnitude for 400 nm light [134]. Moreover, the lower photon energy of 3.1 eV for 400 nm had an additional advantage. With a lower energy scattered light was expected to generate less charged particles from metal surfaces within the vacuum chamber. Therefore, the laser setup was changed in order to use 400 nm light for the generation of the electrons. At $\lambda = 400\,\text{nm}$ the electrons were then produced by a two-photon process. For an acceleration voltage of 15 kV the necessary 10^6 electrons per pulse could still be achieved without damaging the cathode (subsection 4.4.3). As

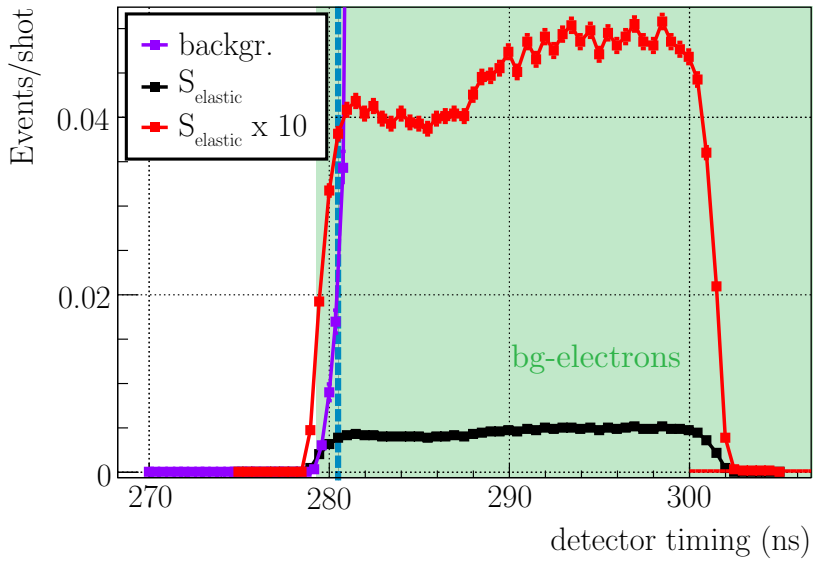

Figure 4.7: Event counts per shot for background (violet) and expected electron scattering (black) as a function of detector timing with 400 nm light for electron generation and the fast Photek switch. Background and scattering signal correspond to electron pulses with 10^6 electrons per pulse. For illustration the scattering signal is magnified by a factor of 10 (red). The choice of timing for a diffraction experiment is depicted by the blue line.

a higher laser intensity was necessary for the two-photon effect the actual reduction of S_{setup} depended on the power level. Using 400 nm light, the resulting total background amounted to 60 electrons per shot for the generation of 10^6 electrons per pulse for similar conditions as before. This was a reduction by a factor of 2 compared to 266 nm light.

The final reduction of S_{setup} relative to $S_{\text{elastic, shot}}$ was realized by gating the detector. The time-dependence of the electron beam and the remaining S_{setup} after change of wavelength are compared in Figure 4.7 for an electron energy of 15 keV. A different type of switch (Photek) with a shorter fall time was installed to improve the cut-off. The MCP was turned on for a duration of 30 ns. The expected scattering signal $S_{\text{elastic, shot}}$ for DIBN was deduced from measurements of the direct beam (black curve). For illustration this signal was multiplied by a factor of 10 (red curve). S_{setup} was detected with the direct electron beam blocked and pulses containing 10^6 electrons (violet curve).

There was no significant background before the electron beam, so the photon background of S_{setup} was suppressed by at least 4 orders of magnitude. This implied either a larger difference in detection efficiency between the two wavelengths than provided by the company (one order of magnitude) or that the early part of S_{setup} was not only photons. It could have been photons that then generated electrons close to the detector. This process would have been reduced due the lower energy of the photons. The suppression of the early signal was a significant improvement in comparison to the data shown in Figure 4.6 as it allowed for gating the detector on the direct electron beam and cut-off S_{setup} to a

level comparable to the expected scattering signal $S_{\text{elastic, shot}}$.
The remaining background most likely originated from electrons as it arrived during a few ns after the electron pulse. Photons would arrive earlier and ions much later. For an experiment with optimized signal-to-noise ratio, one would measure at the first few ns of the detector signal originating from $S_{\text{elastic, shot}}$ (marked as blue line in Figure 4.7). Using the fast high voltage switch it was possible to reduce the background to $S_{\text{setup, shot}} = 0.04$ per shot with a slightly reduced detection efficiency for $S_{\text{elastic, shot}}$ of $q = 0.004/0.005 = 0.8$. The expected scattering signal $S_{\text{elastic, shot}} = 0.004$ per shot was one order of magnitude smaller than the background $S_{\text{setup, shot}} = 0.04$. This is illustrated by $S_{\text{elastic, shot}} \times 10$ and $S_{\text{setup, shot}}$ crossing close to the timing for measurement (blue line).
In conclusion, the apparatus inherent background per shot $S_{\text{setup, shot}}$ was significantly reduced, but was still ten times higher than the signal. For diffraction experiments on DIBN in chapter 5 the background could be subtracted by reference measurements, but it had to be ensured that the statistical noise due to background was not larger than the signal. The fluctuation of the noise was estimated with the square-root of the total background. Assuming the ratio of $S_{\text{elastic, shot}}/S_{\text{setup, shot}} = 0.1$, the signal-to-noise ratio can be estimated. For scattering event numbers of $S = 10$ per bin, the background would approximately be $B = 100$. The according error due to background noise $\Delta B = \sqrt{B} = 10 = S$ would be similar to the signal. Therefore, the achieved background level was assumed to allow for recording of diffraction patterns if $S > 10$ per bin, so that the signal-to-noise ratio $SNR > 1$. From the radial plots in Figure 2.5 c,d a signal modulation amplitude for DIBN of $S \approx 1000$ entries per bin is calculated for $s \approx 3 \cdot 10^{10}/\text{m}$. Therefore the experimental parameters assumed for the simulations in Figure 2.5 c allow for a signal that is significantly higher than the noise due to $S_{\text{setup, shot}}$.

4.4.2 Spot size and coherence of the electron beam

For alignment experiments the electron spot at the interaction point has to have a similar or smaller size than the alignment laser. Otherwise the fraction of isotropically distributed molecules in the probed volume would be too large. As schematic overview of the geometry is depicted in Figure 2.7. The alignment laser RMS spot size is on the order of 20 to 100 µm to achieve the peak intensities necessary for alignment (section 3.2 and chapter 6). Simulations with ASTRA [131] in cylindrical symmetry were used to predict the necessary voltage U_f for focusing an electron beam with 10^6 per pulse accordingly. It is to note that these simulations are only used to deduce a qualitative behavior. The asymmetry due to electrode form and electron pulse could not treated (section 4.3).
Figure 4.8 a depicts the simulated electron spot size σ_x as a function of the electron bunch's distance from the cathode for $U_f = -13.3$, -13.5 and -13.7 kV with a constant voltage on the cathode $U_c = -15$ kV. For illustration the distance corresponding to the electron gun size (grey area), sample position (6.5 cm) and detector (24.3 cm) are marked. The simulated electron beam contained 10^6 electrons per pulse. It was assumed cylindrically symmetric around the flight axis. By increasing U_f the focus strength increased. The

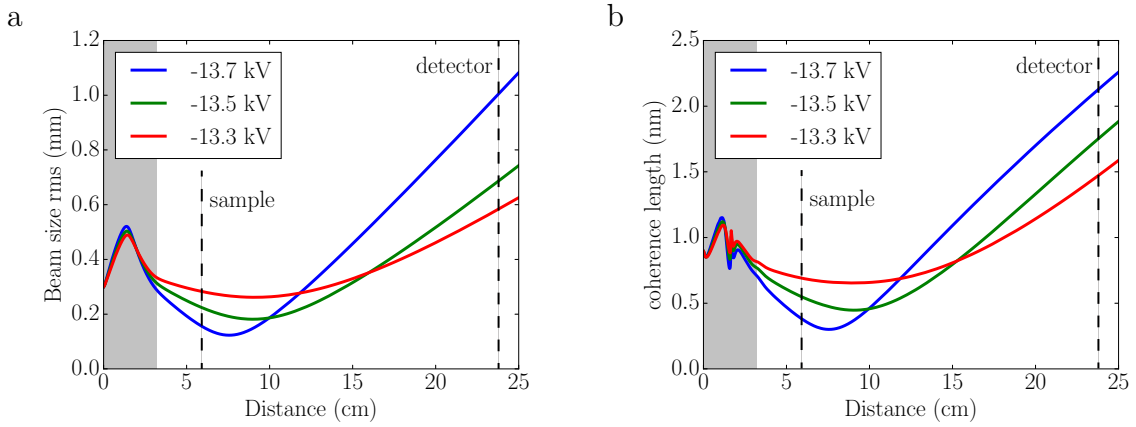

Figure 4.8: Simulation of an electron beam containing 10^6 electrons per pulse for a cathode voltage of 15 kV. The electron beam size rms (a) and the transverse coherence length (b) are depicted as a function of the electron pulse's distance to the cathode. The sample and detector position are indicated. The grey shaded area depicts the electron gun from the cathode to the end of the grounded electrode. The colors correspond to the focusing voltages $U_f = -13.3$, -13.5 and -13.7 kV.

focus moved closer to the sample and the focus size was decreased. The electron spot could be focused down to $\approx 100\,\mu$m with two drawbacks: Firstly, the spot size on the detector increased, as shown in Figure 4.8 a. Secondly, the transverse coherence length L_c (equation 4.4) was reduced. L_c is depicted for the same simulation as a function of the distance to the cathode in Figure 4.8 b. It depends linearly on the spot size, if the emittance is constant. Both – broadening of the electron beam and loss of coherence – can lead to a broadening of the intensity structures on the detector and reduce the contrast [115].

The effect of broadening as a function of focusing voltage U_f was studied experimentally observing the diffraction signal off the aluminum sample with an acceleration voltage of $U_c = -20$ kV. In Figure 4.9 a the radial sum of the scattering intensity for 10^3 electrons is shown as a function of s. Peaks are labeled with Miller indices (hkl). The same experiment was conducted with 10^6 electrons per pulse, depicted in Figure 4.9 b. For experiments with high electron numbers the detector voltage had to be reduced and the detection efficiency was not linear anymore (section 4.3). For better illustration of the low signal parts for high s, the intensity is depicted on a logarithmic scale. The colors correspond to different focusing voltages. For $U_f = -17.6$ and -17.733 kV the focus was close to the detector, $U_f = -18$ kV corresponded to a focus between sample and detector, for -18.266 kV the focus is close to the sample. The voltages and colors correspond to the ones in Figure 4.8 for the 1.3 times higher acceleration voltage of -20 kV.

For analysis of the data the background was subtracted. It decreased approximately exponentially with s and exponential function was fitted to the background intensity I_B in the raw data for $s < 6 \times 10^{10}/\text{m}$. In this s regime the peaks (220) and (311) were observable

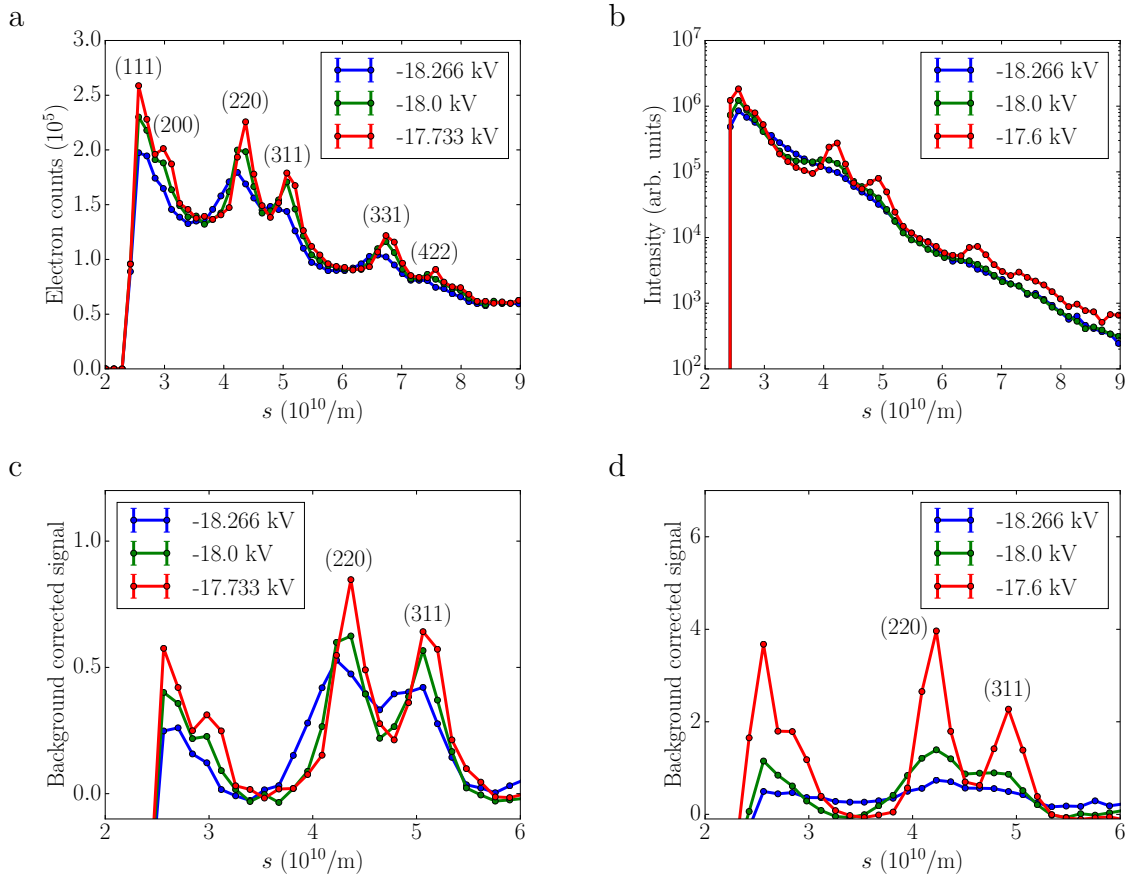

Figure 4.9: Radial scattering intensity for aluminum at 20 keV with (a) 10^3 and (b) 10^6 electrons per pulse. For 10^6 electrons per pulse, the electron counts are depicted on logarithmic scale for illustration. Different focusing voltages are color-coded. The data was background corrected for $s < 6 \cdot 10^{10}$/m and is plotted accordingly in (c) for 10^3 and in (d) for 10^6 electrons per pulse. Peaks are labeled with Miller indices (hkl).

in all measurements and could be compared. The exponential function had to be adapted for each curve as I_B changed as a function of focusing voltage. The background corrected signal was calculated by $I_{\text{corrected}} = (I_{\text{raw}} - I_B)/I_B$ analogous to the modified scattering intensity in equation 2.25. It is depicted for 10^3 electrons per pulse in Figure 4.9 c and for 10^6 in Figure 4.9 d. Fitting a Gaussian distribution with width σ for each of the peaks the broadening was quantified for (220) and (311). With 10^3 electrons per pulse the width increased by a factor of $f_\sigma = 1.7$ for the tested voltage difference. For 10^6 electrons per pulse the broadening was larger with $f_\sigma = 2.3$. The increase in σ for 10^6 electrons per pulse impedes the determination of the peak positions and hence to retrieve structural information. This larger increase in σ was attributed to space charge effects that lead to a larger electron spot size on the detector and a possible decrease in coherence. The reduction of coherence is less probable to be the reason as the simulated coherence length of ≈ 250 pm (Figure 4.8 b) is still larger than the examined interatomic distances of aluminum

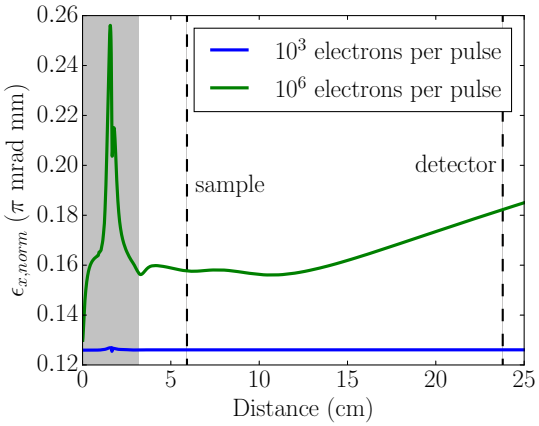

Figure 4.10: Normalized transverse emittance for electron beams containing 10^3 and 10^6 electrons per pulse, respectively. Due to the effect of space charges the emittance increases for higher electron numbers.

($\approx 200\,\mathrm{pm}$). Due to the inaccuracy of the simulations, it cannot be ruled out completely. Another effect was observed for 10^3 electrons per pulse, shown in Figure 4.9 c for $U_f = -18.266\,\mathrm{kV}$. The peaks were shifted towards smaller s, although the experiments were conducted on one day under identical conditions like laser field and sample position. Such a shift could be due to different background, which was ruled out as the background had been adapted and subtracted for each of the curves. The change would correspond to a scaling of s by $\approx 2\%$. A scaling of s could either imply a higher electron energy (400 eV) or a shorter distance between sample and detector (a few mm). An increase by 400 eV in electron energy at the sample was not possible as all electrons start from the cathode with a defined potential of -20 kV and pass the aluminum sample that was fixed in a metal holder on ground potential. Thus, the electrons had the same energy of 20 keV independent of the focusing field. Space charges could not induce an energy change of 400 eV as only 10^3 electrons per pulse were used. Moreover, they would only lead to a broadening, but not a shift. The change in Schottky potential due to the different field strength at the cathode would be expected to lead to a broadening, and not an energy shift of 400 eV. Scaling the distance would correspond to the detector being ≈ 4 mm closer to the sample. The sample was not moved during the measurement and possible unevenness of the sample could not explain a distance variation on the order of mm. Hence it was not clear where the shift of the diffraction peaks originated from. A reason left to examine would be, if the different electron trajectories after the sample due to changed focusing voltage U_f or stray fields could induce the shift. The latter is be avoided in the final setup in chapter 5 by the implementation of a grounded μ-metal shielding around the electron flight path.
In summary it was observed that if the electron beam was focused on the detector, the aluminum diffraction rings were well visible for both electron numbers (Figure 4.5). In the case of 10^3 electrons per pulse, the peaks broadened for higher focusing voltages, but

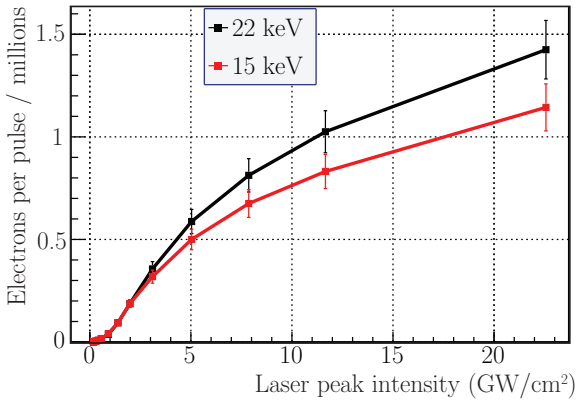

Figure 4.11: Electron number as a function of laser peak intensity for 15 keV (red) and 22 keV (black) electron energy. The central laser wavelength was 400 nm.

were still observable. In the case of 10^6 electrons per pulse the peaks washed out for the highest tested focusing voltage. The reason for this difference were space charge effects: they lead to a larger electron spot on the detector and also to a lower coherence length. From simulations in Figure 4.8 the electron beam size increases by a factor of ≈ 1.6 while the coherence length is still smaller than the atomic distances in aluminum. Thus, in the case of aluminum, the broadening of the electron beam is expected to mostly contribute. In contrast, for experiments on DIBN with a I-I distance of 700 pm the coherence will become more important.

The decrease in coherence length for a similar electron beam focus for different electron numbers originates from an increase in emittance due to space charges. The simulated normalized transverse emittance is depicted in Figure 4.10 for pulses containing 10^3 and 10^6 electrons. The emittance is increased for high electron numbers. In contrast to pulses with low electron number, the emittance also changes throughout the flight path due to space charge interactions. As discussed in section 4.3 this simulation only illustrates the qualitative behavior, as the simulations in cylindrical symmetry do not allow for a quantitative description for large electron numbers, where the asymmetry of the setup is of higher relevance.

4.4.3 Electron energy increase

The setup was further improved to allow for higher electron energies and hence higher acceleration fields. This increased the achievable electrons per pulse. The electron number per pulse is plotted as a function of laser peak intensity in Figure 4.11 for 15 keV and 22 keV electrons. Laser light with a central wavelength of 400 nm and an estimated pulse duration of 370 fs was used to produce the electrons. The electron number increased in a non-linear way with the employed intensity as expected for the two-photon electron emission [111, 112]. More electrons could be produced for higher acceleration fields as

shown for 22 keV in Figure 4.11. The higher extraction field lowered the potential barrier that the electrons had to pass during emission (equation 4.1) [112]. Moreover, the higher electric field lead to a faster electron emission, which reduced the effect of mirror charges and space charges at the cathode. This could also attribute to the higher electron number achieved [112, 116]. With regard to diffraction experiments, the shorter propagation time was expected to reduce energy and temporal spread [135].

4.4.4 Implications for experiments on controlled molecules

The presented measurements have important implications for diffraction experiments on aligned molecules: The largest possible extraction field should be used. It will increase the maximal electron number. Moreover, the shorter propagation time would reduce the spread of the electron beam in space and energy. There are, however, limitations to the increase of the electron energy: The electron gun's insulation setup was designed for cathode voltages up to −30 kV. Moreover, higher electron energies will lead to diffraction rings with smaller radii on the detector. In order to not block the inner-most diffraction ring, which exhibits the largest total scattering signal, the increase in energy is limited by the beam block if the distance between sample and detector remains unchanged. Smaller beam block diameters would be possible in the case of higher electron energies, as the electron beam broadening due to space charge is reduced [135]. The electron energy should be chosen in a way that the first diffraction ring for the sample molecule is larger than the smallest possible beam block.
Then, the experiments should start with an isotropic sample and with the electron beam focused on the detector. This approach ensures that coherence length is the largest and that the electron spot size on the detector is as small as possible. Both lead to a sharp diffraction pattern. Working with one defined focusing voltage will also avoid the shift of diffraction peaks observed for high focusing voltages.
In order to improve the coherence at the desired electron spot size of 100 µm the emittance would need to be decreased. This could be realized by optimizing the emission conditions. Decreasing the laser spot size would decrease the size of the electron beam and hence the emittance at the cathode (equation 4.5). At the same time space effects due to the higher density would increase and lead to a degradation of the emittance. In analogy to section 4.2, the pulse duration could be increased to keep the electron density constant. Reducing the laser spot size for electron generation and increasing its duration might also decrease the electron spot size on the detector.
The electron beam size would be adapted while monitoring the broadening of the diffraction pattern due to electron beam spot size and coherence decrease. Starting with the electron beam focused on the detector, U_f is changed to move the focus closer to the sample as far as the diffraction structure is still visible on the detector. In a final step the alignment laser and electron spot then have to be overlapped in size and position at the interaction point.

5 Toward electron diffraction off controlled molecules

This chapter describes the steps that were undertaken toward electron diffraction experiments on aligned gas-phase molecules. The molecular beam apparatus that prepared the molecules as a state-selected and aligned sample (chapter 3) was combined with the developed electron source (chapter 4). In the first section the complete experimental setup and its parts are described. Then, gas-phase diffraction off a non-supersonic gas jet is presented. This was used for comparison of experimental diffraction data for gas-phase samples with the diffraction simulations in chapter 2. In the following, the preparation of controlled 2,5-diiodobenzonitrile (DIBN) molecules as a sample for electron diffraction is discussed. It includes the spatial alignment achieved and deflection by electrostatic fields. For the diffraction experiments electron, laser, and molecular beam needed to be overlapped. Measurements for spatial overlap monitoring are discussed. Finally, electron diffraction data off an isotropic sample of DIBN is presented, which did, however, not show significant signal above noise.

5.1 Experimental setup

The setup for electron diffraction experiments on controlled molecules is depicted in Figure 5.1. With supersonic expansion from a pulsed Even-Lavie valve it was possible to produce a cold sample of molecules with an internal temperature of typically 1 K [100, 136]. This was an important requisite both for deflection and alignment of molecules as it ensured a relatively high population of molecules in low-rotational-energy states (chapter 3). The DIBN molecules (yellow line) were seeded in helium with backing pressures of about 100 bar. The maximal employed repetition rate of the source was 500 Hz. The relatively high repetition rate increased statistics in experiments (chapter 3).
The molecular beam proceeded through three skimmers and the deflector to the interaction region. The skimmers allowed for skimming of the gas-jet in accordance with the Mach disk [137] to allow for a cold and collimated molecular beam. Moreover, the skimmers formed two differential pumping stages. On the one hand, the resulting lower pressures reduced collisions with the rest-gas and hence heating of the molecular beam. On the other hand the low pressure in the detection chamber minimized scattering off background gas

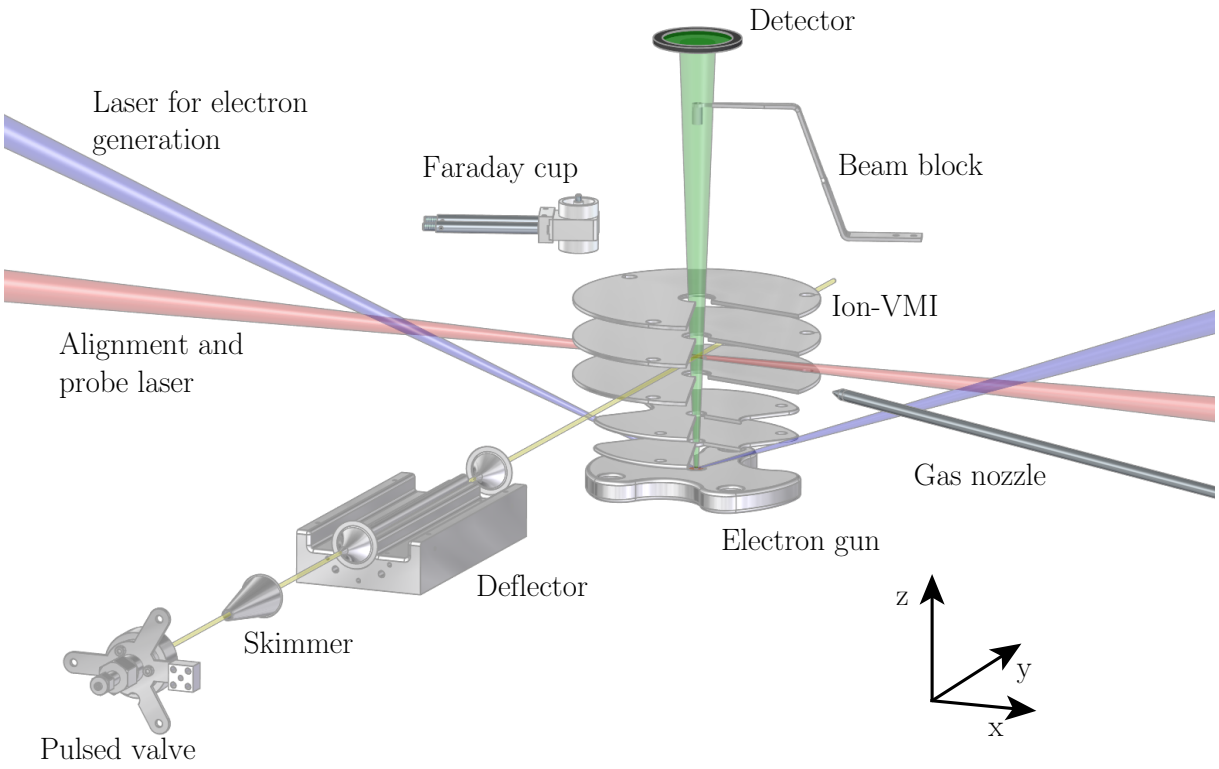

Figure 5.1: The experimental setup of the electron source in combination with the controlled molecules apparatus is depicted. The molecular beam was provided by a pulsed valve. The gas-jet passed three skimmers, two of which were used for differential pumping. After the deflector the molecular beam entered the detection chamber. Alignment laser (red) and electron beam (green) intersected the molecular beam (yellow) perpendicular to each other. A laser with central wavelength of 400 nm was used to generate the electron pulses from a copper cathode. The electrons were accelerated and focused by electric fields created by the electrodes of the electron gun. In order to measure the electron number achieved per pulse a Faraday cup could be introduced into the electron beam path. Similarly, a beam block could be moved in front of the detector to block the direct electron beam for diffraction experiments. Probe laser and ion-VMI were used for the determination of the molecules' spatial orientation. An additional test gas nozzle could be moved to the interaction point.

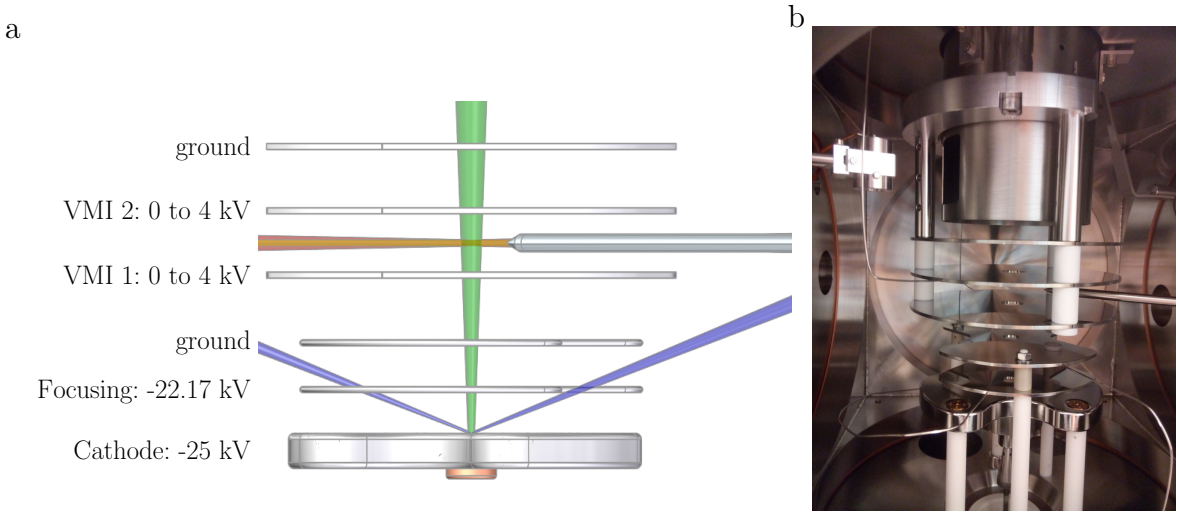

Figure 5.2: The electrode configuration of the electron source and the ion-VMI are depicted (a). Typical voltages applied to the electron source are shown for an electron beam at 25 keV focused on the detector. The ion-VMI consisted of a repeller plate (VMI 1), an extractor plate (VMI 2) and an electrode on ground potential. The photograph (b) depicts the detection chamber setup including insulators, holders, connections and μ-metal shielding.

during diffraction experiments. When the valve was running, the pressure in the detection chamber was on the order of 10^{-9} mbar.

Within the deflector, strong inhomogeneous electric fields were created to deflect the molecules according to their dipole moment [48, 72]. Particles without a dipole moment, like helium, were not deflected. The molecules in high-field seeking states were deflected towards positive z-direction as described in chapter 3. In contrast to the ionization laser, which was used for selection in chapter 3, the electron beam (green) would still probe all of the particles as it was passing the molecular beam along z. The setup was changed to allow for selecting parts of the molecular beam by geometrical means: The last skimmer before the interaction region was movable and allowed for cutting unwanted parts of the molecular beam. This enabled the selection of molecules for probing by the electron beam.

Two laser pulses with a central wavelength of 800 nm were used for alignment and strong field ionization. Both originated from the same laser system as in chapter 3. The alignment laser spectrum was shaped in a saw-tooth form with a rise time of $d_{\text{align}} = 610\,\text{ps}$. The focus size was $\sigma_y = 18.0\,\mu\text{m}$ and $\sigma_z = 11.6\,\mu\text{m}$ and was increased for some experiments by a factor of 2 in z. With a pulse energy of 7 mJ peak intensities were on the order of $I_0 = 10^{12}\,\text{W/cm}^2$. The probe laser had a slightly smaller focus size and could be compressed to $d_{\text{probe}} = 30\,\text{fs}$ (FWHM). The peak intensity obtained was $I_0 = 2.6 \cdot 10^{14}\,\text{W/cm}^2$.

The detection chamber was re-designed from the setups in chapter 3 and chapter 4 to combine electron diffraction experiments with laser alignment and ion-detection (Figure 5.1 and Figure 5.2). Electrons were created at the cathode by laser pulses (blue) with a central

wavelength of 400 nm. Electric fields generated by the electrode configuration discussed in chapter 4 were used to accelerate and focus the electron beam. The highest voltage tested on the cathode was $U_c = -25\,\mathrm{kV}$. The electron beam (green) crossed the molecular beam perpendicular to the alignment laser (red). All three beams had to be overlapped at the interaction point ≈ 65 mm from the cathode.

A spectrometer was mounted in line with the electron gun and is denoted ion-VMI in the following. The electrode configuration with the applied voltages is depicted in Figure 5.2 a. For the voltages shown the electron beam was focused on the detector and experiments with an electron energy of 25 keV could be performed. The ion-VMI was operated at voltages up to 4 kV at the repeller plate (VMI 1). The setup could be used in spatial imaging or velocity imaging mode by changing the voltages on the extractor plate (VMI 2). It was possible to run the ion-VMI while the electron gun was operating and no aberration of the VMI images was observed. After strong field ionization by the probe laser the ion-VMI was used for the detection of the molecules' spatial orientation. Running the ion-VMI in spatial imaging mode allowed the overlap between molecular beam, electron beam and laser to be determined as discussed in subsection 5.4.1. For electron diffraction experiments the ion-VMI was turned off to avoid a variation of electron energy in the interaction region due to the potential of the ion-VMI electrodes.

The electron number per pulse was measured with a Faraday cup with a 5 mm aperture (Dreebit), that was connected to an electrometer as in chapter 4. The electron beam block was a steel pod with a diameter of 4 mm. It was moved into the direct electron beam for diffraction experiments. Insulators, wiring and the μ-metal shield along the drift region between ion-VMI and detector are shown in the photograph in Figure 5.2 b. The μ-metal shield reduced effects of electric and magnetic stray fields that would disturb the electron diffraction pattern. All materials and the connectors were chosen for ultra-high vacuum. With the pulsed valve off, the pressure in the detection chamber was $5 \cdot 10^{-10}\,\mathrm{mbar}$.

For calibration experiments on gaseous samples an additional gas nozzle was installed. It consisted of a 6 mm steel tube, which was narrowed for the last $\approx 7\,\mathrm{mm}$ down to an outer diameter of 0.5 mm at the tip. The gas could be let into the chamber through a hole in the tip with a diameter of $d_{\mathrm{nozzle}} = 36\,\mu\mathrm{m}$. If moved to the interaction point, this source generated gaseous samples for electron diffraction with densities on the order of 10^{11} to 10^{12} particles/cm^3 depending on the pressure applied within the 6 mm-tube. During experiments the pressure in the chamber was not allowed to exceed 10^6 mbar as the MCP could not be operated at higher pressures. The corresponding maximal stagnation pressure in the 6 mm-tube was between 10 and 100 mbar. The Knudsen number $Kn = \frac{\lambda}{d_{\mathrm{nozzle}}}$ was calculated for the above experimental conditions and the particle mean free path λ of argon to be on the order of 0.1 [138, 139]. Under these conditions the flow was not effusive, but no supersonic expansion occurred either. In this intermediate regime no rotationally cold beam was expected. On the one hand, the resulting sample was warm in comparison to the molecular beam and not suited for alignment experiments. On the other hand, the increase of density by three orders of magnitude compared to the controlled sample (chapter 3) allowed for fast calibration on atomic gases and test experiments on isotropic

molecular samples. For running the ion-VMI the gas nozzle needed to be pulled out of the electrode region, as otherwise it disturbed the electric field significantly. With the ion-VMI on ground potential diffraction experiments using the gas nozzle could be performed.
The distance between interaction region and detector was 178(2) mm, which varied as a function of molecular beam and laser position in z dimension. Electron diffraction experiments require for a high dynamic range of the detector due to the fast signal decrease with s. The detector (same as in section 4.3) consisted of a Z-stack MCP (Photonis), a phosphor screen (P46) and a CMOS camera (Optronis CamRecord CL600x2), which was linked to an analysis computer. The detection system allowed for single-shot readout at 1 kHz and a computer software was used for online analysis at the same rate (section 3.2). The detector was sensitive to single electrons. The shots could be integrated over an arbitrary time, which implied a very high dynamic range. The pixel size of the recorded image corresponded to 88 µm on the detector. The detection efficiency for electrons at 25 keV was approximately 60% for the MCP. When the detector was switched, further signal reduction could be observed. In tests of the direct electron beam, the efficiency of the switched detector was between the efficiency without switching and an additional 60% (in total an efficiency of 36%) depending on the detector settings like offset voltage and timing. This additional decrease was partly attributed to the restricted sensitivity of the CMOS sensor of the camera when the light spots on the phosphor screen became less bright in dependence of detector gate timing and voltage.
The center of the detector was more sensitive, which was revealed by recording of cosmic background radiation with long integration times (several hours) without switching the detector voltages. The signal decreased for larger radii. The increased sensitivity at the center could originate from former experiments: The direct electron beam and more electrons in diffraction experiments arrived at small radii section 4.3. If the detector was not damaged, this increased the detection gain, which was observed experimentally. A detector gain map as a function of radius was deduced from the cosmic background radiation signal. The detection efficiency could be different for cosmic radiation than for electrons. Moreover, it was observed to change, if the detector was switched. Therefore, the cosmic radiation signal was only an approximation to the detector gain map for electrons.

5.2 Diffraction tests on gaseous samples

The setup was tested with gaseous samples from the gas nozzle. These tests were used to ensure the quality of the electron beam with gas-phase samples and allowed for comparison of experiment and simulation. For this calibration no alignment was necessary, but a high particle density was desirable to increase the signal. Moreover, pure samples without seed gas were favorable. A gas-jet of sulfur-hexafluoride (SF_6) generated by the gas nozzle fulfilled these requirements. Helium and argon were used to study scattering off atomic gases. An according gas line was attached to the 6 mm tube and the nozzle tip was moved to the interaction point.

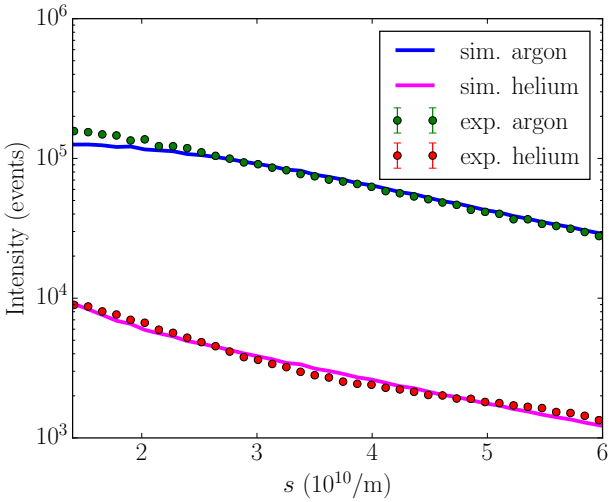

Figure 5.3: The total scattering intensity is shown as a function of s. Normalized experimental and simulated data is depicted for argon and helium. The intensity is plotted on logarithmic scale to allow for a comparison of helium and argon.

5.2.1 Total scattering intensities

Atomic scattering intensities were quantitatively compared to the simulated diffraction patterns. Figure 5.3 depicts the radial sum of scattering intensities for helium and argon as a function of s [1]. Measurements were performed for different electron numbers, averaging times and pressures and then normalized to the following parameters of argon: The number of electrons $N_e = 5 \cdot 10^5$ per pulse, the estimated interaction length $l = 1\,\text{mm}$, the experimental repetition rate $r = 1000\,\text{Hz}$ and the averaging time $t = 200\,\text{s}$. The corresponding gas density of argon at the interaction point depended on the distance of nozzle to electron beam, which was on the order of a few 100 µm and the flow dynamics of the gas. Therefore, the exact relation between density at interaction point and measured pressure could vary and remained an adjustable parameter. The experimental data was corrected for the detector gain, which varied with the radius (section 5.1). The simulation was scaled using the experimental parameters with an adjusted ratio between density at the interaction point to pressure. Simulation and experimental data for argon agreed well for $s > 3 \cdot 10^{10}/\text{m}$ as depicted in Figure 5.3. The discrepancy for low s will be discussed below.

The experimental data for helium was normalized and the simulation adapted in gas density. Simulation and experiment were in very good agreement as illustrated in Figure 5.3. Assuming the measured pressure was related to the density at the interaction point in the same way as for argon, the stagnation for the helium simulation pressure was 1.25 times

[1] The signal was simulated as discussed in chapter 2 taking into account the corresponding solid angle for each pixel. The experimental and simulated signal of each pixel was assigned to a radius. The sum for each radius is then plotted after binning. The radius was transferred to s.

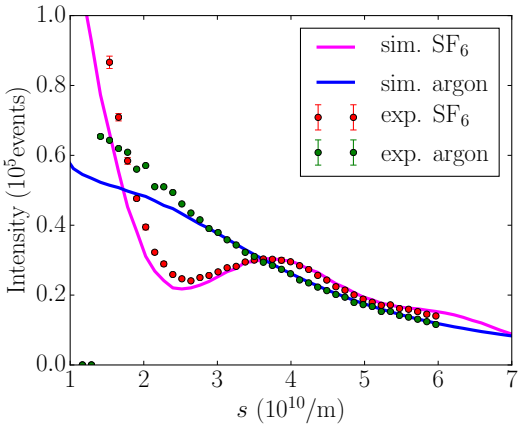

Figure 5.4: The total scattering intensity for SF_6 and argon is depicted as as function of s. Experimental data and the according simulations are shown.

higher than the measured one. This difference was within the accuracy of the pressure measurement, taking into account the type of gauge (Pfeiffer IKR 270) and the different flow dynamics at the gas nozzle in dependence of atom size. In contrast to the argon measurement, there was no discrepancy for low s values in helium. There are, however, oscillations with a small amplitude and a period of $\Delta s \approx 4 \cdot 10^{10}$/m. These probably originated from water, nitrogen or other contamination within the gas line.
In order to examine the simulation of molecular samples, sulfur hexafluoride (SF_6) was used as gaseous sample. The measurements were performed again for several electron numbers, gas densities and averages and then normalized. The simulated and experimental scattering intensity are depicted in Figure 5.4 in comparison to argon. The depicted errors of the experimental data were the standard error of the mean for several averaged measurements. This included possible variations due to different electron numbers, instabilities of the system and statistical errors. The relatively small error bars show that these differences were small. The scattering intensity included a modulation due to the molecular scattering contribution. It was visible in the total scattering intensity as suggested by simulations (subsection 2.3.4).
For $s < 3 \cdot 10^{10}$/m the simulated scattering intensity was lower than the experimental intensity. The difference was similar in the case of argon, which implies a systematic underestimation of the atomic scattering intensity for low s. As the helium measurements agreed better to simulations, the discrepancy depended on the atomic number Z of the sample. This contradicts the notion that an imperfect detector gain map is responsible for the observed difference. It is more likely that the discrepancy can be attributed to the modeling used in simulations in chapter 2. The approximations in the simulations (chapter 2) did not take into account finite coherence, vibrations of the molecule, chemical bonding effects or scattering interferences between three atoms of a molecule. These effects would broaden or shift the diffraction pattern, but not increase the signal for low s in atomic scattering. In contrast, the modeling of elastic and inelastic scattering factors

have an influence on the signal amplitude (chapter 2). The first Born approximation and hence the Mott-formula used are only valid for low Z [57, 62, 63]. This could explain the observation that for helium (low Z) simulations and experiments accord well, while for argon and SF_6 they only accord for high s. Moreover, the inelastic scattering has a large contribution for small scattering angles [140]. It could therefore be considered that the inelastic contribution was underestimated for larger atoms at the electron energies used. Therefore, the failure of Born approximation and the inelastic scattering are the most probable reasons to explain the discrepancy for low s. Their effect would accord with the observation that the simulations fit more accurately for helium. In both cases the inaccuracy was reported to be on the order of some % [63, 64] and are therefore equally probable to cause the observed discrepancy. This experimental data could be used to further improve the simulations with respect to modeling of elastic and inelastic scattering.

5.2.2 Modified scattering intensity and bond length determination for SF_6

Information on the structure of SF_6 was retrieved from the modified scattering intensity by comparing experiment and simulation. For both – simulations and experiment – the modified scattering intensity was calculated using the argon scattering intensity I_{argon} as I_b in equation 2.25:

$$s \cdot M(s) = s \cdot \frac{I_{\mathrm{SF_6}} - I_{\mathrm{argon}}}{I_{\mathrm{argon}}} \tag{5.1}$$

The resulting signal as a function of s is depicted in Figure 5.5 a. Simulation and experiment are close to each other for the whole s-regime. The discrepancy in the total scattering intensity for low s was suppressed as it originated from a systematic error in the atomic scattering intensity, which mostly cancelled out in equation 5.1.
In order to consider the error due to discrepancy in the determination of the bond length, the systematic error was estimated. From the difference between simulation and experiment in Figure 5.4 it was deduced that

$$\Delta M = \left(\frac{I_{\mathrm{SF_6}} - I_{\mathrm{argon}}}{I_{\mathrm{argon}}}\right)^{\mathrm{exp}} - \left(\frac{I_{\mathrm{SF_6}} - I_{\mathrm{argon}}}{I_{\mathrm{argon}}}\right)^{\mathrm{sim}}. \tag{5.2}$$

With

$$(I_{\mathrm{SF_6}} - I_{\mathrm{argon}})^{\mathrm{exp}} - (I_{\mathrm{SF_6}} - I_{\mathrm{argon}})^{\mathrm{sim}} \ll I_{\mathrm{argon}}^{\mathrm{exp}} - I_{\mathrm{argon}}^{\mathrm{sim}} \tag{5.3}$$

one can write

$$I_{\mathrm{mol}} \approx (I_{\mathrm{SF_6}} - I_{\mathrm{argon}})^{\mathrm{exp}} \approx (I_{\mathrm{SF_6}} - I_{\mathrm{argon}})^{\mathrm{sim}} \tag{5.4}$$

and it follows

$$\Delta M \approx I_{\mathrm{mol}}/I_{\mathrm{argon}}^{\mathrm{exp}} - I_{\mathrm{mol}}/I_{\mathrm{argon}}^{\mathrm{sim}}. \tag{5.5}$$

ΔM was included in Figure 5.5 a by adding it to the statistical error. The dominating error depended on the s-value: the systematic errors were larger for $s < 3 \cdot 10^{10}/\mathrm{m}$ and

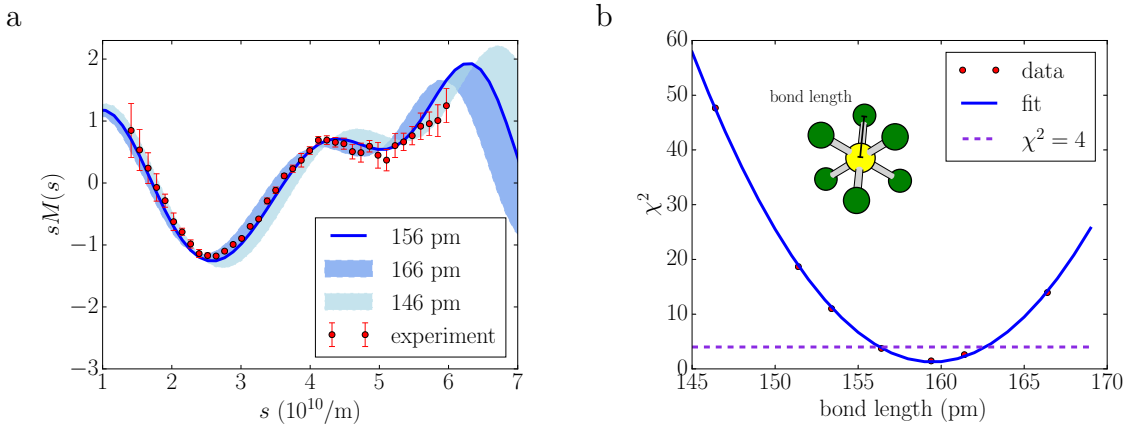

Figure 5.5: The modified scattering intensity $sM(s)$ using argon as background is calculated from the intensities (a). In comparison to the experimental data simulations for different bond lengths are depicted. χ^2 was calculated as a function of bond length and the distribution was fitted by a quadratic function (b). The dashed violet line shows $\chi^2 = 4$. The S-F bond length is illustrated as inset.

statistical errors for $s > 4 \cdot 10^{10}/\mathrm{m}$. For $2.5 \cdot 10^{10}/\mathrm{m} < s < 4.5 \cdot 10^{10}/\mathrm{m}$ both errors types were relatively small, which lead to smaller error bars in this regime in Figure 5.5 a.
The oscillation of $sM(s)$ encoded the structure of the molecule. In comparison of experiment to simulation it was possible to retrieve the bond length $r_{\text{S-F}}$, which is depicted as inset in Figure 5.5 b. Simulations for various bond lengths were compared to the experimental data, three of which are depicted in Figure 5.5 a. The experimental data was very close to the simulation for the literature value of $r_{\text{S-F}} \approx 156\,\mathrm{pm}$ [141], which could be seen from the agreement in position of maxima and minima. If significantly different bond lengths were simulated (± 10 pm in Figure 5.5 a), it became visible directly from the position of extreme points, that the bond length did not agree.
In order to determine the bond length and the according precision the reduced χ^2 value was calculated for several bond lengths (Figure 5.5 b). The quality of the fit for a bond length was given by

$$\chi^2 = \frac{1}{N-1} \sum_{i=1}^{N} \frac{(M_{\text{exp},i} - M_{\text{sim},i})^2}{\sigma_i^2} \tag{5.6}$$

for N samples with the errors σ_i including statistical and systematic errors. It has to be noted that this is an extension of the normal statistical usage of χ^2 as systematic errors were included. A quadratic fit was used to approximate the data points retrieved from simulations by equation 5.6 and is shown in Figure 5.5 b. The minimum of the fit gives the best estimated bond length, which was $r_{\text{S-F}} = 160\,\mathrm{pm}$ with $\chi^2 = 1.3$. This was close to the optimal value for a least-square fit of $\chi^2 = 1$.
The confidence level, which describes the reliability of a result, was used to determine the precision of the bond length determination. Relations between confidence level and χ^2 were

deduced from tabulated values [142]. In order to achieve a confidence level of $2\sigma \hat{=} 95.45\,\%$ the fit had to reach $\chi^2 = 4$ indicated by violet line in Figure 5.5 b. The corresponding bond lengths were $156\,\text{pm} < r_{\text{S-F}} < 164\,\text{pm}$. Therefore, with a probability 95.45 % the retrieved bond length was $r_{\text{S-F}} = 160 \pm 4\,\text{pm}$, which was close to the equilibrium value of $r_{\text{S-F}} = 155.68(6)\,\text{pm}$ [141]. This agreement confirmed that the experimental parameters like camera calibration and distance between interaction region and detector were good. Moreover, the modulation due to molecular-scattering interference was not significantly broadened. This meant that the coherence length of the electron beam was larger than the bond length of SF_6.
The comparison of experiment and simulation illustrated that our simulations could be used to predict diffraction intensities quantitatively. The total scattering intensity could be simulated with limitations, but still allowing for a reasonable prediction of signal to noise for most of the diffraction pattern. The structure determination in comparison to simulation is expected to work well as the simulation of the modified scattering intensity was in agreement with the experiment.

5.3 Molecular beam of controlled 2,5-diiodobenzonitrile

5.3.1 Beam of 2,5-diiodobenzonitrile seeded in helium

The pulsed valve was used to provide a molecular beam of DIBN seeded in 90 bar of helium. DIBN has a permanent dipole moment of $\mu = 3.817$ D, which allowed for deflection of DIBN in strong inhomogeneous electric fields [67]. Moreover, DIBN exhibits an anisotropy in its polarizability, which enabled alignment by intense laser light [67]. Both deflection and alignment of DIBN have been shown in combination with x-ray diffraction [36]. With a melting point of DIBN of 170 °C at standard pressure the sample needed to be heated. The valve was operated at temperatures between 160 °C and 190 °C for the experiments within this chapter.
The composition of the molecular beam at the interaction region was determined by recording of a time-of-flight spectrum. The sample was ionized by strong field ionization and the fragments were recorded using the ion-VMI spectrometer and the MCP-detector coupled to an oscilloscope. The signal on the oscilloscope is plotted as a function of mass-to-charge ratio in Figure 5.6. The largest mass-to-charge ratio was assigned to the parent ion $DIBN^+$. Smaller fragments of DIBN could be found for smaller mass-to-charge values. The ion signal assigned to indole and aniline originated from former experiments on the same apparatus. The I^+ signal was used for recording of molecular beam profiles and the determination of the degree of alignment.
The I^+ signal was also used to estimate the amount of sample within the interaction region in the direct, undeflected beam. The ionization volume was determined by the ionization laser focus size and was on the order of $10^{-6}\,\text{cm}^3$. At a valve temperature of 190 °C, 50 to 200 I^+ ions were detected per shot. Taking into account the detection efficiency and under the assumptions that the laser ionizes all the molecules in this volume and that one I^+ ion

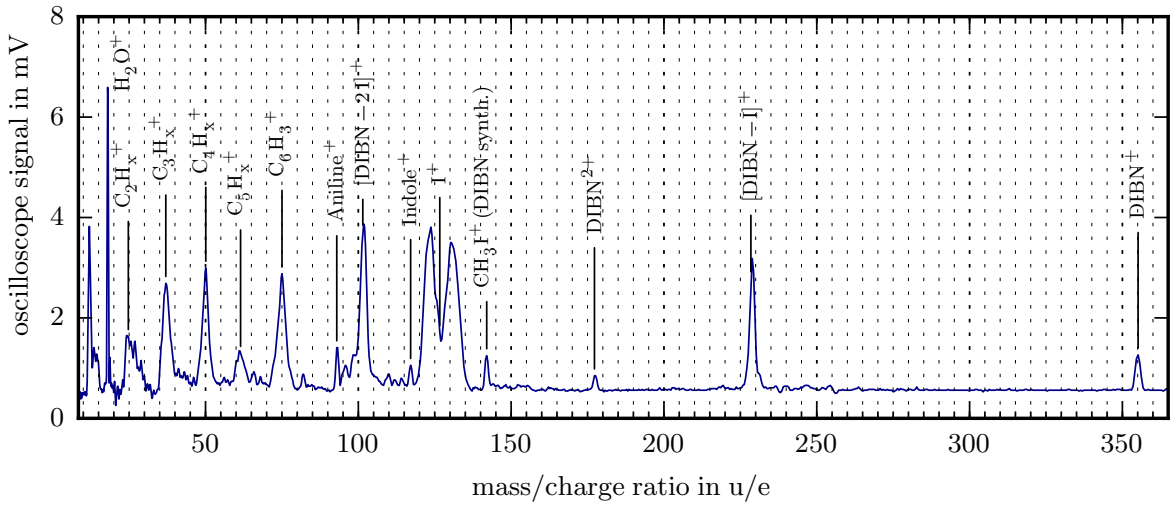

Figure 5.6: Time-of-flight spectrum after ionization for DIBN seeded in helium. The signal is depicted as a function of mass-charge-ratio. The peaks are assigned to the corresponding fragments.

per molecule is detected, the amount of sample in the interaction region was $1.4 \cdot 10^8/\text{cm}^3$ to $6 \cdot 10^8/\text{cm}^3$. This provided an estimation for the molecular number density. It was close, but slightly lower than the expected signal in the undeflected molecular beam of $10^9/\text{cm}^3$. The difference could be explained by the fact that not all of the molecules were ionized. During experiments at 190 °C, the plunger of the Even-Lavie valve magnetized within a few hours. Moreover, the capton gaskets had to be replaced, which could be attributed to the sample damaging the gaskets at the relatively high temperature. Both effects were not expected as the Even-Lavie valve (High Temperature unmounted valve by Even Lavie) is designed for temperature up to 250 °C and was used with DIBN before [36]. The gaskets were exchanged every few days, but the plunger could not be replaced within the framework of this thesis due to long delivery times. The resulting leaks lead to a higher pressure in the source chamber. This increased the molecular beam temperature and could compromise the operation of the valve if the leaking rate in the source chamber increased beyond the pumping capacity. Therefore, the temperature of the Even-Lavie valve had to be reduced to 160 °C. The amount of sample in the interaction volume decreased to $3 \cdot 10^7/\text{cm}^3$ to $1.3 \cdot 10^8/\text{cm}^3$, which did not provide enough sample to record diffraction patterns of DIBN within 12 hours of measurement time, as discussed below.

5.3.2 Electrostatic deflection

Electrostatic deflection of DIBN was employed to select molecules in low rotational quantum states as in reference 36 and to optimize the background subtraction for electron diffraction experiments. Density profiles of the molecular beam were measured in order to study the effect of deflection and optimize it. The ionization laser was scanned by moving its

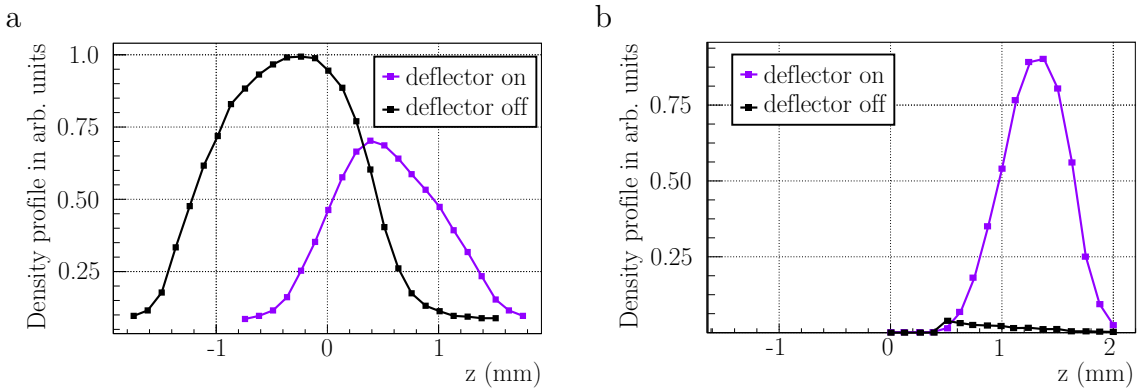

Figure 5.7: The density profile of DIBN is depicted as a function of laser position in z. Deflection lead to a shift of the molecular beam (a). If the skimmer behind the deflector was moved towards the deflected part, the undeflected part of the beam could be cut (b).

focusing lens in z dimension (see Figure 5.1 for the coordinate system) and the number of I^+ ions was recorded. The density profile was first measured without deflection fields and the last skimmer in-line with the deflector. This was the direct undeflected molecular beam depicted in black in Figure 5.7 a. For deflection of the DIBN molecules a voltage of 12 kV were applied to the deflector rod and the last skimmer was moved upward by 0.5 mm. The deflected molecular beam is depicted in violet in Figure 5.7 a. The molecular beam was shifted to higher z-values and broadened due to deflection. As the molecular beam was skimmed behind the deflector only parts of the deflected molecular beam were probed.

The DIBN molecules could be separated from helium, which possesses no permanent dipole moment and was therefore not deflected. The last skimmer was moved in positive z-direction to ≈ 1 mm until the undeflected beam and the helium beam were blocked. Only deflected molecules could pass into the interaction region. Figure 5.7 b depicts the resulting density profiles as a function of laser position along z. In black the molecular density is shown for the deflector turned off. The violet curve corresponds to the deflected molecular beam with a width of $\sigma_z = 280\,\mu$m. Turning off the deflector, the amount of molecules in the beam was reduced by a factor of 26 for background measurement, which was determined by comparing the respective areas of the graphs in Figure 5.7 b. The density profiles in Figure 5.7 a and b are given in arbitrary units. They are only quantitatively comparable within each respective figure, but not from Figure 5.7 a to Figure 5.7 b as the experimental conditions like molecular beam density were different between measurements for the two figures.

Besides a reduction of helium, deflection allowed for a well-defined subtraction of scattering from background. Diffraction data could be recorded for the molecules in the deflected beam. Then the deflector was switched off, the molecules did not arrive at the interaction region anymore and background data was collected. The amount of helium in the detection chamber was unchanged, as helium was not deflected. A fast alternation between the two

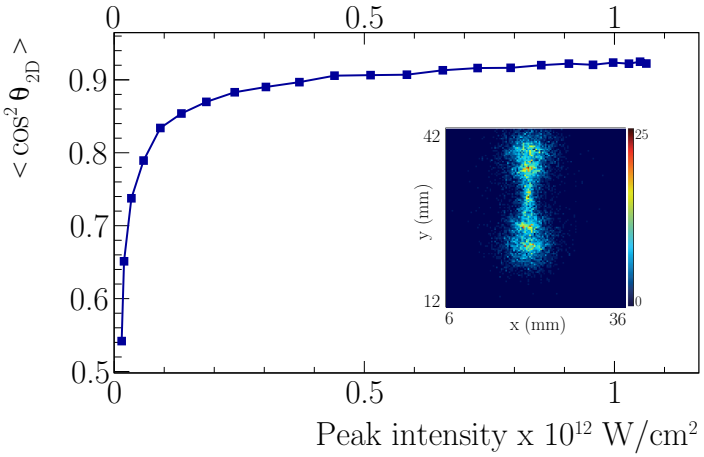

Figure 5.8: The degree of alignment of DIBN was measured as a function of alignment laser peak intensity. The inset shows the relevant part of the detector image in VMI mode for the maximal intensity. The corresponding degree of alignment is $\langle \cos^2 \theta_{2D} \rangle = 0.922$

modes ensured similar experimental conditions of diffraction and background measurement as it avoided changes due to longterm drifts. Additionally, as discussed in chapter 3, the molecules in low rotational energy states exhibit a higher dipole moment and were deflected more. Therefore, a higher degree of alignment could be achieved in the most deflected part of the beam.

5.3.3 Alignment

For the planned diffraction experiments on controlled molecules discussed in section 2.3 the candidate molecule DIBN had to be laser aligned [36]. The laser pulse used (chapter 3 and section 5.1) allowed for aligning DIBN close to the adiabatic regime [36]. The spatial orientation was probed by Coulomb explosion after strong-field ionization using the probe laser. The I^+ was recorded by the ion-VMI spectrometer in velocity map imaging mode (chapter 3). A corresponding 2D image is shown as inset in Figure 5.8. The offset in y on the detector depicts the molecular beam velocity relative to the symmetry axis of the spectrometer. The two ring segments corresponded to two ionization channels for I^+. The inner ring, i.e. ions with lower velocity, originated from an Coulomb explosion with a singly charged phenyl ring. The outer ring, corresponding to a doubly charged phenyl ring, lead to a larger axial recoil of I^+. With higher recoil the direction of the velocity agreed better with the C-I bond direction. Therefore, the angular distribution of the outer ring-segment was assumed to represent the molecule's spatial orientation more accurately, as discussed in section 3.2.
The degree of alignment $\langle \cos^2 \theta_{2D} \rangle$ was determined from the outer ring. It increased with the laser peak intensity as depicted in Figure 5.8. The maximal degree of alignment $\langle \cos^2 \theta_{2D} \rangle = 0.922$ was achieved for a peak intensity of $I_0 \approx 10^{12}\,\mathrm{W/cm^2}$ (inset in Figure 5.8).

This degree of alignment would lead to a strong enhancement of contrast in an electron diffraction pattern and would allow for 3D-reconstruction as discussed in chapter 2. Some alignment of $\langle \cos^2 \theta_{2D} \rangle \approx 0.8$ could be achieved for a laser intensity of $I_0 \approx 10^{11} \mathrm{W/cm^2}$, which would still yield a weaker anisotropy in the diffraction pattern as illustrated in Figure 2.6.

5.4 Overlap between electron beam, laser and molecular beam

Electron beam, laser and molecular beam had to be overlapped in space and time for diffraction experiments on aligned molecules. The importance of good overlap between alignment laser and electron beam to maximize the amount of aligned molecules in the probed volume is illustrated in Figure 2.7. In the experiment, the laser was first overlapped with the molecular beam. This was possible by recording of density profiles and by maximization of the ion signal in dependence of laser focus position, valve position and valve timing. Then the electrons had to be overlapped with molecular beam and laser to ensure the overlap of all three beams. Spatial overlap was determined by combining electron impact ionization with the spatial imaging mode of the ion-VMI spectrometer as discussed in subsection 5.4.1 . Temporal overlap is discussed in subsection 6.1.2.

5.4.1 Electron impact ionization for spatial overlap

Electrons that inelastically scatter off atoms or molecules can ionize the atom or molecule if the electron energy exceeds the ionization potential (typically tens of eV). This is called electron impact ionization. The corresponding cross sections are comparatively low for energies in the tens of kV regime, but were observable in the presented setup for electron pulses with electron numbers of 10^6 electrons per pulse. The electron beam was used to ionize helium in the molecular beam. The He^+ ions were accelerated by the ion-VMI toward the MCP detector that was gated to their arrival time.
The electron impact ionization was employed for monitoring the overlap of electron beam with molecular beam and alignment laser. Spatial distributions of ions generated by the electron beam and by the alignment laser were compared. The ion-VMI spectrometer was used in spatial mode, in which the spatial distribution of the ions at the interaction point was mapped on to detector. The 2D image for electron impact ionization of He^+ is depicted in Figure 5.9 a and for alignment laser ionization (I^+) in Figure 5.9 b. The same detector section is depicted in both images. As the spectrometer was operated with the same voltages, both images correspond to the same region at the interaction point. The ion signal could be related to the spatial distribution of the respective beams at the interaction point with the calibration factor of spatial imaging $m_s = 3.78$. A reference bar of 0.7 mm at the interaction point is plotted as inset in Figure 5.9.
For the image in Figure 5.9 a, the electron beam's focus was on the detector. The inferred

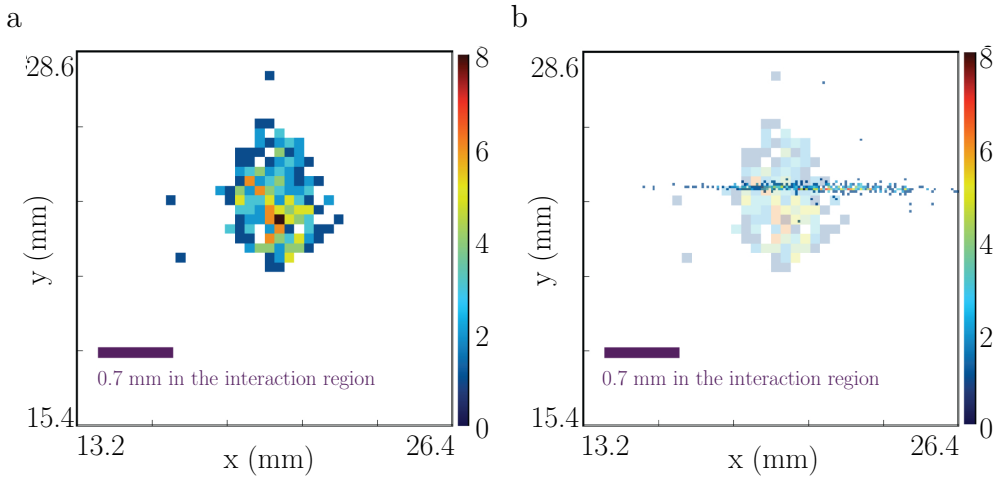

Figure 5.9: Spatial imaging of ions created by electron impact ionization (a) and by the alignment laser (b). The electron impact ionization signal is depicted in the background of (b) to illustrate the spatial overlap. The bar indicates a length of 0,7 mm at the interaction region.

RMS sizes of the electron beam at the interaction point were $\sigma_x = 222$ µm and $\sigma_y = 317$ µm. The asymmetry of the electron beam originated from the electron beam's asymmetry at the cathode and the asymmetry of the electrodes (chapter 4).
The alignment laser created 0.04 I^+ ions per pulse and the 2D image for spatial imaging is shown in Figure 5.9 b. The laser propagation direction is in x direction, which lead to the elongated ion signal. If the ion images overlap on the detector, they were also expected to overlap at the interaction region in x and y dimension. The electron beam propagated in the z direction, which ensured complete overlap with the laser in z. For illustration of the overlap, the electron impact ionization signal is depicted in the background of Figure 5.9 b. The comparison of the two signals allowed the laser and electron beam positioning to be monitored. From Figure 5.9 b it became obvious that the beams were partly overlapped. The electron beam was slightly off the laser and molecular beam center, which could be adapted by correcting the beam pointing.
The molecular beam and the electron beam were overlapped by monitoring the spatial imaging signal. After optimization, the electron pulses containing $9(2) \cdot 10^5$ electrons produced 0.01 He^+ per shot. For a comparison to theoretical cross sections, literature values for electron impact ionization cross sections were retrieved for electron energies up to $T = 10$ keV[2]. The energy of the electron at the interaction point within the ion-VMI was $T \approx 27$ keV (electron source acceleration and ion-VMI potential). The available data was extrapolated to this energy by

$$\sigma_{\text{helium}} = A \cdot \log(T \cdot B)/T \tag{5.7}$$

[2]http://www.nist.gov/pml/data/ionization/

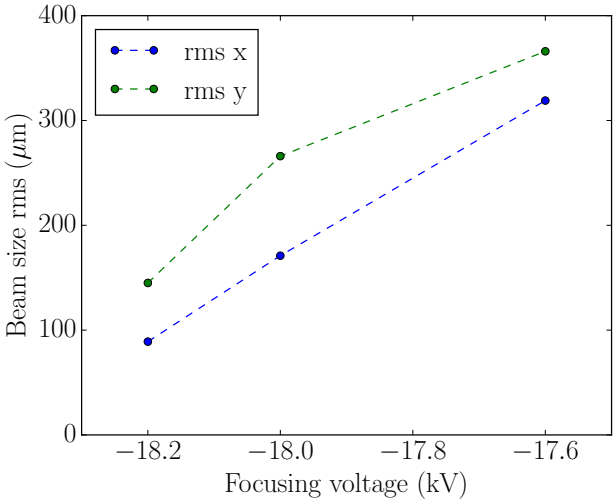

Figure 5.10: The RMS of the electron beam size at the interaction region is plotted as a function of the focusing voltage.

with fit parameters A and B [143]. The resulting total cross section was $\sigma_{\text{helium}}(27\,\text{keV}) = 8.4(8) \cdot 10^{-19}\text{cm}^2$. From the pressure inlet in the experiment, the helium density $n_{\text{helium}} = 1.5(5) \cdot 10^{12}/\text{cm}^3$ over an interaction of length $l = 1.0(3)\,\text{mm}$ was estimated. Considering the detection efficiency 0.04(2) ions were expected per shot. Therefore, experimentally measured signal of $0.01\,\text{He}^+$ per shot was on the estimated order of magnitude. The missing factor of 4 could be attributed to the inaccurate approximation of a constant helium density for the interaction volume length.

In order to spatially overlap the electron beam with the alignment laser the position and the sizes needed to be matched. Figure 5.9 b shows that the electron beam was significantly larger than the laser focus, which signified that the sample probed in diffraction experiments would contain a large fraction of unaligned molecules. As discussed in subsection 2.3.3, this would lead to a local loss in contrast and the anisotropy would reduce. It was therefore necessary to either increase the laser size or reduce the electron beam size at the sample. Increasing the laser focus implied a loss of alignment and is discussed in subsection 6.1.3.

Adjusting the electron focus position was possible by changing the focusing voltage U_f of the electron source. Corresponding simulations for the cylinder-symmetric case were discussed in chapter 4. The spatial imaging mode of the ion-VMI could be used to experimentally monitor the electron spot size at the interaction sample as a function of focusing voltage. The RMS of the electron beam size σ_x and σ_y is depicted in Figure 5.10 for different U_f with a constant $U_c = -20\,\text{kV}$. As the focusing voltage was changed to move the electron focus closer to the sample, the electron spot size decreased as expected from simulations. A size of $\sigma_x \approx 100\,\mu\text{m}$ and $\sigma_y \approx 150\,\mu\text{m}$ was reached for $U_f = -18.2\,\text{kV}$.

Comparing the measurements in Figure 4.4 and Figure 5.10 it could be observed that the asymmetry of the electron pulse is turned in x and y between cathode and interaction

point. The spatial imaging mode in Figure 4.4 showed that the electron beam was larger in x at cathode, while Figure 5.10 illustrated that it was larger in y at the interaction point. In order to better match the size of the electron beam with the laser in Figure 5.9 b, it would be profitable to turn the ratio of electron beam spot size in x and y. This was important with respect to possible setup improvements as discussed in subsection 6.2.1.
For diffraction experiments it remains to simultaneously ensure coherence of the electron beam and a small spot size on the detector. Considering data plotted in Figure 4.9, the electron beam properties were not good enough to image aluminum at $U_f = -18.2\,\mathrm{kV}$. Therefore the voltage change should be accompanied by a decrease of electron source size and an increase of electron acceleration fields. Furthermore, the electron beam could be refocused after the interaction point (chapter 6). The method discussed here would allow for monitoring of the electron beam size at the interaction region, while performing these changes.

5.5 Toward electron diffraction off 2,5-diiodobenzonitrile

Diffraction experiments were performed on DIBN seeded in helium with electrons at 25 keV. The valve was operated at 250 Hz and with the reduced temperature of 160 °C as discussed in section 5.3. For the first experiments, the molecules were not aligned. Overlap between molecular beam and electrons was achieved by optimizing the electron impact ionization signal of He^+ ions as discussed in subsection 5.4.1. In order to ensure coherence at the sample and the smallest possible electron spot on the detector, the electron beam was focused on the detector. As discussed in section 4.4 this was the most suitable operation mode for detecting a first diffraction signal. According to the deflection profiles in Figure 5.7 the skimmer was moved towards the deflected part for reduction of helium and to allow for background subtraction.
Diffraction data was recorded with the deflector switched on and off in iterations of 10 minutes. This made it possible to record data for the molecular sample (deflector on) and background (deflector off) under similar experimental conditions. Subtracting the deflector-off measurement from the deflector-on measurement was expected to yield a scattering intensity originating only from deflected DIBN molecules. The measurement was run over night for 14 hours and is shown as radial plot in Figure 5.11. It was expected to show a scattering intensity close to the simulated total scattering intensity of DIBN, which is shown for comparison in Figure 5.11. The simulation was scaled to agree with the experimental data at its maximum value ($s \approx 2 \cdot 10^{10}/\mathrm{m}$). The first minimum of the experimental data was at the correct s-value compared to the simulation, but the observed modulation was on the same order as the error bars and therefore not significant. Moreover, the measured signal oscillated around the zero-line. This implied that the background contained a similar amount of counts as the data recorded with molecular beam. In summary, the diffraction off DIBN was not proven as the recorded data did not contain molecular scattering signal beyond the noise level.

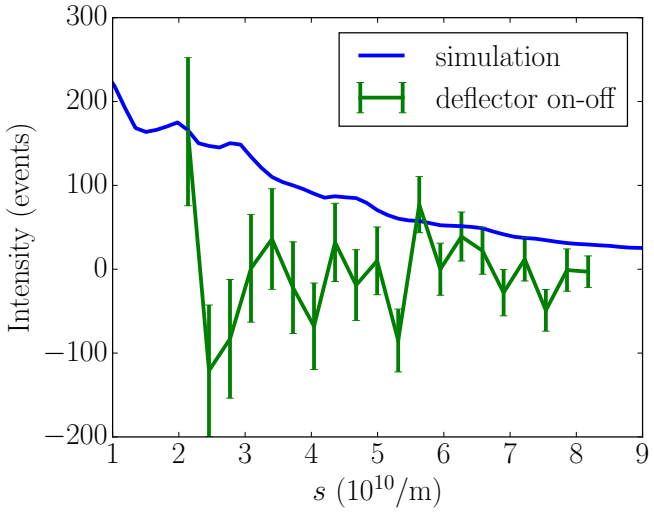

Figure 5.11: Diffraction off DIBN in helium. The radial plot of measurements with deflector off is subtracted from measurements with deflector on. For comparison the simulated total scattering intensity is depicted.

In order to find the reason for the lack of signal the experimental parameters were compared to the ones assumed in simulation: From simulations it was predicted that the molecular structure was detectable for an electron number $N_e = 10^6$ per pulse, a molecular density $n = 10^8$ molecules/cm^3, an interaction length $l = 100\,\mu$m, a repetition rate $r = 500$ Hz and the averaging time $t = 12$ hours (subsection 2.3.2). In the experiment, the electron number was achieved. The valve repetition rate in the experiment was lower by a factor of two to reduce magnetization of the plunger. Another factor of two was lost in repetition rate due to the alternation between diffraction and background measurements. The interaction length was longer ($\mathrm{FWHM_{mol}} = 0.7$ mm) as the full molecular beam could be probed for diffraction of isotropic samples. The deflection allowed the helium to be reduced. The difference in deflected to not-deflected molecules at the interaction point was a factor of 26 (Figure 5.7 b). Therefore, the simulated helium suppression by a factor of 10 was assumed to be reasonable. All parameters except the molecular density were comparable to the simulation parameters in Figure 2.5.

The reason for the missing signal was attributed to a reduced molecular density due to the malfunction of the pulsed valve. The pulsed valve had to be operated at lower temperatures, which provided one order of magnitude lower densities than expected (subsection 5.3.1). Moreover, after approximately two hours the valve started to leak and the molecular beam heated. With a warm molecular beam the deflection was reduced and the molecules did not arrive at the interaction point anymore. The signal level for deflector on and off became the same. The available time with signal at a reduced density was not enough to achieve a diffraction pattern, as depicted in Figure 5.11. The repair of the valve was attempted by exchanging the valve's gaskets, repeated demagnetization of the plunger, reduced valve

temperature and lower repetition rate. Despite these efforts the malfunction of the valve remains an open problem.
Alternatively, diffraction data of the direct beam without deflection was recorded. The retrieval of signal modulations was not possible beyond statistical errors due to the high helium background and the reduced molecular density. It was therefore deduced that the approach of background subtraction by deflector on-off measurements was more suitable. It is expected to work with a fully functioning valve. The electron diffraction pattern of the isotropic sample would then serve as a starting point for experiments on aligned molecules.

6 Conclusions and Outlook

In the framework of this thesis major steps were undertaken toward the realization of electron diffraction imaging off state-selected and strongly aligned gas-phase molecules. Time-resolved electron diffraction allows structural dynamics to be studied on the atomic level. The state and spatial control of the molecules enhances the information that can be retrieved by diffraction experiments.
Simulations of diffraction patterns were used to determine feasible experiments. In comparison to experiments the simulated diffraction patterns were employed for data analysis with respect to the molecular structure. Both parts – electron source and a beam of controlled molecules – were set-up and tested experimentally with a strong focus on their applicability to the combined experiment. The molecules could be spatially controlled at higher repetition rates than before. This was crucial in respect to electron diffraction experiments on controlled molecules, which exhibit a low signal strength. The high degree of alignment, which was enhanced by selecting molecules in low rotational and vibrational states would allow for the retrieval of 3D-information from diffraction patterns. The electron source was designed to address the requirements of the controlled molecules apparatus: electron number, beam size, coherence, pulse duration, and background were characterized in simulation and experiment. Finally, the challenge of combining both setups was met. This included the implementation of the electron source, the laser beams for alignment and probing, an ion spectrometer, and several characterizing tools within one chamber that could be attached to the controlled molecules beam apparatus. Diffraction experiments on isotropic gas-phase samples from a gas nozzle and the agreement between simulation and experiment confirmed that it was possible to retrieve the bond length of the SF_6 molecule. The electron gun was tested to be suitable for isotropic samples and predictions on its application to aligned samples were provided. Preparatory steps were taken toward electron diffraction of controlled molecules, which included background subtraction by deflection, alignment and spatial overlap. First diffraction data was recorded but information on the molecular structure could not be obtained due to lack of signal, which was caused by technical malfunction of the pulsed valve.
On the basis of the capabilities of the built experimental setups and the gathered information a diffraction pattern for controlled DIBN can be predicted. The steps toward the corresponding experiment are described in the following including temporal overlap and the simulated diffraction pattern that is expected. Furthermore, an outlook is given on possible improvements of the setup and the diffraction experiments that could then be

realized. Subsequently, the prospects of time-resolved experiments are discussed.

6.1 Prospect on electron diffraction off aligned 2,5-diiodobenzonitrile

6.1.1 Coherence and spatial overlap

As discussed in subsection 5.4.1 the spatial overlap between electrons and alignment laser can be directly monitored in the present setup. The electron beam size at the sample was found to be significantly larger than the laser at the interaction point. Adapting the alignment laser and electron beam size at the interaction point to each other implies increasing the laser or decreasing the electron spot size, or both.
As strong alignment of molecules demands laser intensities on the order of tens of $\mathrm{GW/cm^2}$, the laser size is limited by the available laser power. With the present laser system a peak intensity of $7 \cdot 10^{10}\,\mathrm{W/cm^2}$ would be achievable for an laser focus with $\sigma = 100\,\mu\mathrm{m}$ in both dimensions and a reduced pulse duration of 150 ps. According to Figure 5.8 the molecules would then be aligned with $\langle \cos^2 \theta_{2D} \rangle = 0.8$. Here a linear increase of the degree of alignment with shorter pulse duration and hence higher intensity is assumed, which is only an approximation [42, 144]. The simulated diffraction patterns for $\langle \cos^2 \theta_{2D} \rangle = 0.8$ still exhibits an observable anisotropy and increase in contrast (subsection 2.3.3).
The electron beam size at the interaction point could be reduced to $\sigma = 100\,\mu\mathrm{m}$ by changing the electrostatic focusing until the spatial imaging of ions created by laser and electron beam will show overlap as described in subsection 5.4.1. The drawback of the decrease in electron beam size at the interaction point is twofold. Experiments on aluminum showed that the structure determination became difficult with the electron beam focused at the sample. The coherence length at the sample decreases and the electron spot on the detector broadens as discussed in subsection 4.4.2. Simulations showed a decrease of coherence length below the size of the DIBN molecule (I-I distance = 700 pm). However, partial coherence could suffice to record the structure [115, 145]. The exact limit of focusing at the interaction point for DIBN could be determined from monitoring the isotropic diffraction pattern while changing the focusing voltage. In combination with monitoring the spatial overlap as described in subsection 5.4.1 this would yield the optimal configuration for diffraction experiments on aligned molecules.

6.1.2 Outlook on temporal overlap

When spatial overlap is achieved, the beams have to be overlapped in time. For temporal overlap with the electron pulse the laser pulse duration should not be shorter than the simulated electron pulse duration of 60 ps at the sample position. This would be fulfilled for alignment experiments close to the adiabatic regime, for which the alignment laser pulse typically has a duration on the order of 100 ps.

For a rough overlap in time between laser and electron pulse, flight times of generated electrons could be compared in simulation and experiment. According to simulations (SIMION) the electron flight time from the interaction point to the detector was t_{gun}=1.9 ns for 25 keV electrons from the gun. The laser at the interaction region could be used to produce electrons by ionization of the molecular sample. If these were accelerated by the ion-VMI in electron detection mode their time of flight from the interaction point to the detector was simulated to be t_{laser}=7.2 ns. The corresponding times could be measured and then compared to the values from simulation. The time difference should be equal to $t_{\mathrm{laser}} - t_{\mathrm{gun}}$=5.3 ns, which could be achieved by adapting the laser beam path.
Then, laser and electron beam could be overlapped in time using photoionization-induced lensing effects [146]. The laser produces a cloud of charges at the interaction point by ionization. The separation of positive ions and ejected electrons can create an electric field that disturbs the undiffracted electron beam. If the ionization laser arrives at the interaction point at the same time or a few ps earlier than the electrons, the electron pulse's deforms [146]. This would be visible on the detector. In order to reach a high charge density both probe and alignment laser should be used for ionization. The gas nozzle in the detection chamber could also be used to introduce an easily ionizable gas. Moreover, an intense laser pulse can have a direct effect on the electron beam through its ponderomotive potential [147]. Both approaches allow for temporal overlap and also for the determination of time-zero for pump-probe experiments.
In a final step the fine adjustment of timing can be performed by optimizing the effect of alignment on the diffraction pattern. If the alignment laser and electron beam are overlapped in an optimal way, the anisotropy in the diffraction pattern will be maximal [23, 35, 38, 148].

6.1.3 Predicted diffraction pattern

The measurements within chapter 5 provide the foundation for the following predicted diffraction pattern. For a realistic prediction the degree of alignment, overlap and amount of helium have to be considered.
Matching the laser and electron spot size to $\sigma = 100$ in perpendicular geometry, would still lead to unaligned molecules being probed by the electron beam, because the molecular beam is larger. The width of the deflected molecular beam cut out by the skimmer was $\sigma_z = 277\,\mu\mathrm{m}$. Considering the overlap scheme in Figure 2.7 a the amount of aligned molecules within the probed volume would be 36%. For typical molecular beams the amount of helium is estimated to be 2000 times higher than molecules (subsection 2.3.2). Particles like helium, which exhibits no permanent dipole moment, can be depleted by electrostatic deflection as discussed in chapter 3. A depletion factor of 10 for helium was estimated from the measured reduction of undeflected molecules in section 5.3. Therefore, approximately 200 times more helium than molecules arrive at the interaction point.
The expected scattering signal was simulated for a molecular density of $10^8/\mathrm{cm}^3$ an averaging time of 12 hours and a repetition rate of 250 Hz. With the discussed overlap of

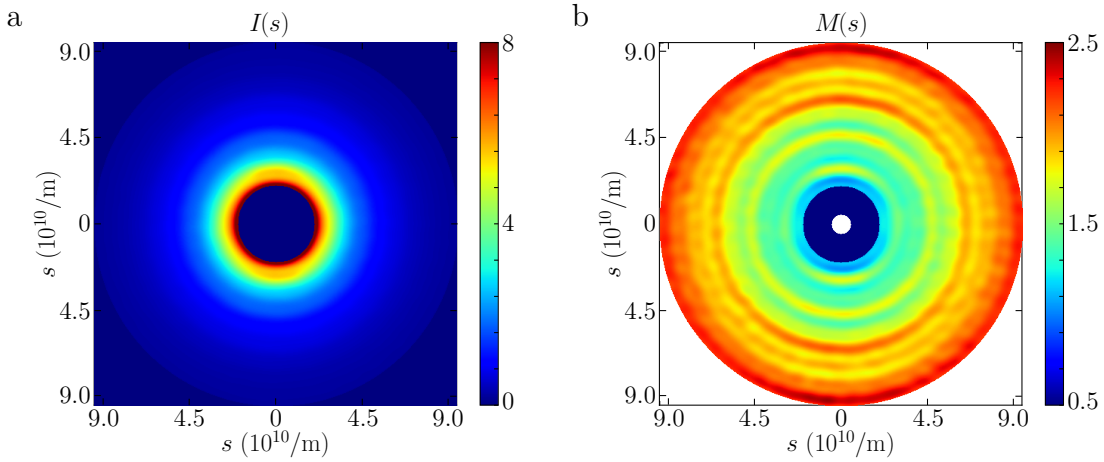

Figure 6.1: The total scattering intensity of DIBN seeded in helium is plotted for 200 times more helium in the beam than molecules (a). The helium intensity is used as background scattering intensity I_b for the calculation of the modified scattering intensity $M'(s) = I_{\text{dibn}}/I_{\text{helium}}$ (b). 36% of the probed molecules are aligned and the degree of alignment is $\langle \cos^2 \theta_{2D} \rangle = 0.8$.

electrons and laser pulse $\langle \cos^2 \theta_{2D} \rangle = 0.8$ would be expected. The resulting total scattering intensity is plotted in Figure 6.1 a for the achieved overlap, and the helium-to-molecule ratio that was discussed above. Treating helium as background, a variation of the modified scattering intensity $M'(s) = I_{dibn}/I_{helium}$ was calculated as discussed in chapter 2 and is shown in Figure 6.1 b. Both intensities are depicted for an s-range that corresponded to the detector image for an electron energy of 25 keV.
The structures originating from the molecular scattering intensity would be visible. The contrast is weakly increased due to alignment. The diffraction experiment of aligned DIBN would serve as a starting point for further development. In order to increase contrast and anisotropy the setup could be altered as discussed in section 6.2. The method could then be extended to other molecules and to time-resolved electron diffraction of controlled molecules.

6.2 Possible setup alterations

The major challenges for the electron diffraction experiments on controlled molecules with the present setup are signal-to-noise, and overlap restrictions of electrons with aligned molecules. Some possible alterations of the setup could be performed to optimize these aspects. Moreover, further experimental characterization of the electron pulse concerning pulse duration and coherence, which do not rely on electron-trajectory simulations, would be desirable.

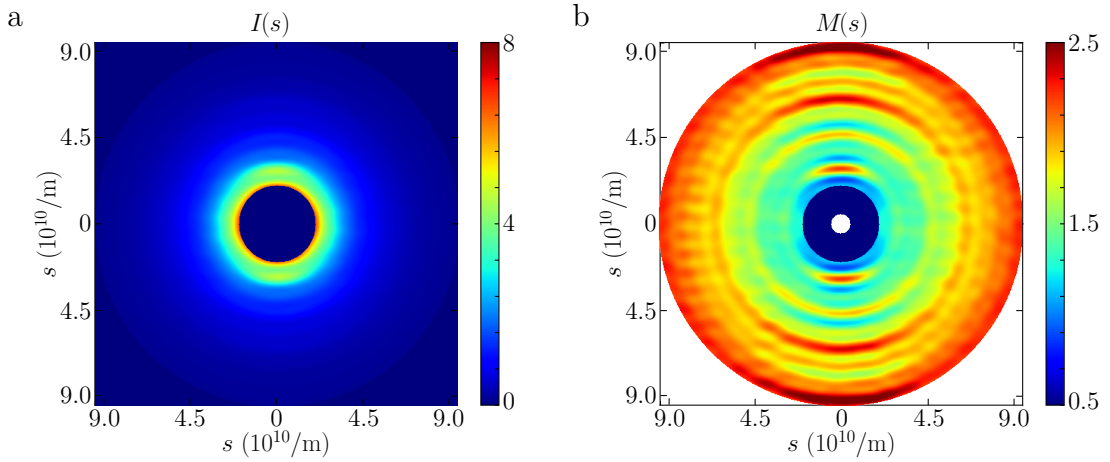

Figure 6.2: The total intensity (a) and the modified scattering intensity (b) after the suggested overlap optimization (see text). 50% of the probed molecules are aligned and the degree of alignment is $\langle \cos^2 \theta_{2D} \rangle = 0.9$.

6.2.1 Overlap improvement

Laser and molecular beam size as well as shape at the interaction point could be adapted to correspond closer with the electron pulse. Cutting the molecular beam in the direction of the electron's flight axis would reduce the number of probed not-aligned molecules depicted in Figure 2.7 a. A disadvantage of this technique would be the loss of molecular density at the interaction point that would result from selecting outer parts of the molecular beam, where the density is lower. Another possibility would be to deform the laser focus of the alignment laser to be larger in direction of the electron beam and to increase its overall size. In order to still reach strong alignment this approach requires a higher laser pulse energy or lower laser pulse durations.

From the perspective of the electron beam size, it is in principle possible to reduce it to a similar size of the alignment laser at the cost of broadening of the diffraction pattern. To counteract this effect additional electrodes (for example the ion-VMI in Figure 5.1) could be used to re-focus the electron beam after the interaction point. This would lead to a smaller electron spot size at the detector. Moreover, the asymmetry of the electron pulse at the interaction point should be turned to adapt the electron spot shape to the laser focus shape (Figure 5.9 b). This would be possible by using a laser pulse with an elliptically formed spatial profile to generate the electrons. A telescope with cylinder lenses could be implemented to achieve such a laser profile.

The larger extension of the electron beam would then accord with the propagation direction of the laser beam. In this dimension the laser focus is large (x in Figure 5.9 b) and more of the aligned molecules would be probed. If necessary, the loss of coherence could be addressed by using a smaller spot size and longer pulse durations of the laser generating the electrons, less electrons or higher acceleration fields (section 4.4).

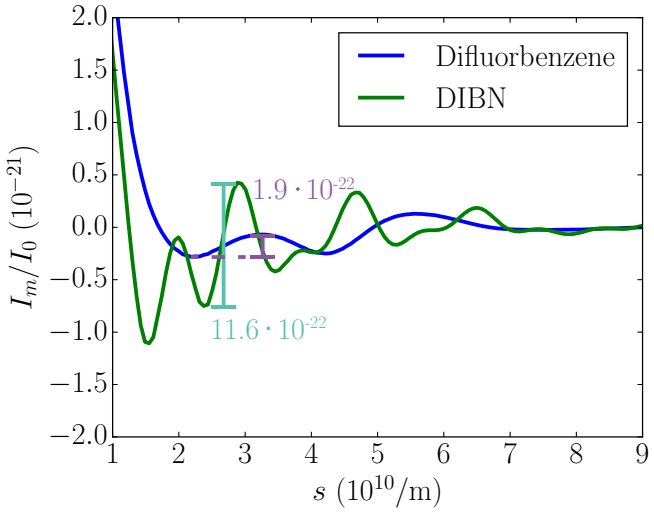

Figure 6.3: Molecular scattering intensity for an isotropic sample of DIBN and Difluorbenzene. The comparison of oscillation shows the necessary increase in signal.

Further diffraction patterns were simulated (Figure 6.2) on the foundation of these overlap improvements and taking into account the higher energy (10 mJ) provided by a new laser system that was recently installed. The laser properties could be changed to a spot size of $\sigma_y = 70\,\mu\mathrm{m}$ and $\sigma_z = 100\,\mu\mathrm{m}$ with a FWHM pulse duration of $d_L = 60\,\mathrm{ps}$ yielding a peak intensity of $4 \cdot 10^{11}\mathrm{W/cm^2}$. According to Figure 5.8 this would lead to an aligned sample of DIBN with $\langle \cos^2 \theta_{2D} \rangle = 0.9$. The electron pulse would need to be shaped at the interaction point to $\sigma_x = 140\,\mu\mathrm{m}$ and $\sigma_y = 70\,\mu\mathrm{m}$ by changing the laser spot on the cathode. Adjusting the skimmer position after the deflector would allow for a molecular beam width of $\sigma_z = 200\,\mu\mathrm{m}$ and a ratio of 50% aligned molecules in the probed volume. The according scattering intensities $I(s)$ and $M'(s)$ for the same repetition rates and densities as above are depicted in Figure 6.2. Compared to the predicted diffraction pattern in Figure 6.1 contrast and anisotropy are expected to be significantly enhanced by the suggested setup alterations.

6.2.2 Signal-to-noise

For experiments on arbitrary molecules that do not necessarily contain heavy atoms like iodine, the signal-to-noise ratio has to be improved. As an illustration of the reduction of signal due to smaller atoms the molecular scattering off difluorbenzene (DIF) is compared to DIBN in Figure 6.3. The modulation that encodes information of the molecular structure is considerably smaller. For $s \approx 3 \cdot 10^{10}/\mathrm{m}$ the amplitude is $11.6 \cdot 10^{-22}$ for DIBN and $1.9 \cdot 10^{-22}$ for DIF (Figure 6.3). The relative signal reduction could be described by $S_{\mathrm{DIF}} = S_{\mathrm{DIBN}}/6$.
The noise would originate from scattering of helium in the molecular beam and from the electron gun background (subsection 4.4.1). Both types of noise will not change with a

different molecule. If the noise is assumed to scale with the square-root of the total signal one can estimate the necessary increase in averaging a to achieve the same signal-to-noise ratio SNR as for DIBN:

$$SNR = \frac{S_{\mathrm{DIBN}}}{\sqrt{S_{tot}}} \tag{6.1}$$

and

$$SNR' = \frac{a \cdot S_{\mathrm{DIF}}}{\sqrt{a \cdot S_{\mathrm{tot}}}} = \frac{a \cdot S_{\mathrm{DIBN}}/6}{\sqrt{a \cdot S_{tot}}} \tag{6.2}$$

are set equal:

$$\frac{S_{\mathrm{DIBN}}}{\sqrt{S_{\mathrm{tot}}}} = \frac{a \cdot S_{\mathrm{DIBN}}/6}{\sqrt{a \cdot S_{\mathrm{tot}}}} \iff \frac{a/6}{\sqrt{a}} = 1 \iff a = 36 \tag{6.3}$$

For a diffraction pattern of DIF with a similar signal-to-noise as depicted in Figure 2.5 c,d 36 times longer integration time would be needed, i.e. one month for one diffraction pattern, which is not a reasonable time scale for experiments to be stable and operational. From the above estimation it becomes obvious that the signal-to-noise ratio is essential in electron diffraction experiments on controlled molecules. This can either be improved by background reduction or by increasing the signal per second.
The noise in the predictions above is mainly caused by helium. A larger deflection would aid in cutting away the helium. Recent developments allow an increased deflection that could yield a better separation [149].
An increase in repetition rate of the experiment would improve the signal-to-noise further. The generation of electrons does not require high energy pulses. Therefore, a low-energy but high repetition rate laser system could be used to generate electron pulses at a high repetition rate. One example of such a source is an ultrashort pulsed electron gun with few electrons per pulse and a MHz repetition rate [150]. The source repetition rate could be increased through cw molecular beams. This was realized experimentally by using small diameter seeding gas nozzles or buffer gas cells [151–153]. Finally, it has been suggested to align molecules by a cw laser beam, for which an according intracavity laser system is currently developed and tested [154].
Another way to increase the signal would by to increase the electron number per pulse. This could be realized without reducing the coherence by larger acceleration fields or longer laser pulses for electron generation.

6.2.3 Measurement tools for coherence length and pulse duration

There have been far-reaching achievements in characterization of ultrashort electron pulses for time-resolved diffraction experiments [24, 113, 155]. The characterization of the electron pulse with respect to coherence length and pulse duration is important for the improvement of the presented electron source with respect to time-resolved electron diffraction experiments on controlled molecules as discussed in chapter 4.
The coherence length at the sample position could be determined by a deduction of the pattern broadening on the detector [120, 156]. Moreover, TEM grids at the interaction point

could be employed to measure the coherence at the sample position [157]. In combination, these approaches could be used to study the effect of electron spot size broadening and decrease of coherence [115]. This would aid the understanding of measurements in subsection 4.4.2. and allow for a determination of the optimal electron pulse with respect to coherence at the sample and electron spot size at the detector.
For the present setup the electron pulse duration was simulated, which yielded an approximate value. Measurements of the exact electron pulse duration would allow for an according adaptation of the alignment laser duration, which is a prerequisite for optimized temporal overlap [38]. In order to determine the time-zero and the pulse duration of the electron beam the same methods could be employed as for temporal overlap determination (subsection 6.1.2). They are based on molecular alignment, the ponderomotive potential and photoionization-induced lensing [38, 146–148]. It also has been shown that streaking by electric fields could be used to determine the electron pulse duration [18, 158]. The photoionization-induced lensing method could be realized with the present setup without any changes and is therefore favorable.

6.3 Improvements of simulation and analysis of diffraction patterns

In this thesis, simulations of electron diffraction patterns have been used for feasibility tests as well as for the analysis of the measured diffraction patterns. The comparison to experimental data indicated that the modeling was in good agreement for the modified scattering intensity, but the total scattering intensity did not agree for low s and high Z (section 5.2). This will become more significant for experiments with molecules like DIBN containing high-Z atoms like iodine, as an inaccuracy in bond length determination on the order of % would be expected [63]. The atomic scattering factors could be calculated including the phase shift, for example by partial waves approach [17]. If the discrepancy in total scattering intensity persists, it would be reasonable to assume that the inelastic scattering was underestimated for low s. The Bethe modification [66] could be used to describe the transformation between lab frame and center-of-mass system, which is necessary in inelastic scattering. It is especially important for small s ($s < 2 \cdot 10^{10}/\mathrm{m}$ for 40 keV electrons) [66], which is close to the s regime, where the discrepancy between experimental data and simulation was observed in section 5.2. For further improvement of the modeling of inelastic electron scattering one could include correlation effects as discussed in [65]. For energies above 40 keV and small angles, relativistic effects become relevant and could be implemented by reference 64, where an expression for the integral inelastic cross section was derived by assuming the electron-electron interaction to be coulombic. The difference between non-relativistic and relativistic treatment can amount up to 15% for 40 keV electrons [64] and is therefore estimated to be on the order of % for the 25 keV electrons produced in the present setup.
Another possible advancement in simulation of electron diffraction patterns would be to

include the finite sizes of electron beam and sample. Also the effect of transverse and longitudinal partial coherence could be implemented [115]. Both are expected to lead to a broadening of peaks in the scattering intensity. For the experiments on SF_6, described in chapter 5, they were not relevant as the coherence length was larger than the molecule and the electron beam was focused on the detector. In contrast to these experiments on SF_6, the broadening is expected to become visible for experiments on molecules with larger atoms, and with the electron beam focused at the sample.

Within this thesis only experimental data was used to determine $sM(s)$. Then, $sM(s)$ only oscillates around zero, if the background gas scattering intensity I_b was similar to the atoms of the molecule. This will not be the achieved for the analysis of DIBN with the helium scattering as I_b (Figure 2.5). The retrieval of the radial distribution function would need to be adapted for this effect. For large s and low Z the agreement with simulation were good enough to solve this issue by using the according I_b from simulation. If the corresponding correction proves difficult, I_b could be calculated by a fit to the experimental data in combination with theory [17, 70]. Instead of comparing the experimental modified scattering intensity $sM(s)$ to the simulated one, one could retrieve the radial distribution function from the experimental $sM(s)$. The approach employed in literature [70] includes an exponential or polynomial fit to the total scattering intensity in order to determine $sM(s)$. The zero-crossings are adjusted to the theoretical predicted points and the radial distribution curve may then be derived from $sM(s)$ via a Fourier sine transform [70].

In the case of electron diffraction off aligned molecules, the signal from an isotropic sample can be used as a reference [38]. As discussed in subsection 2.3.3 diffraction data of aligned molecules would allow for phase-retrieval algorithms and 3D reconstruction of the molecular structure [33, 34, 38, 39]. For time-resolved electron diffraction data, the analysis would treat the diffraction pattern of the original state as reference pattern. By subtraction, it would then be possible to monitor the changes induced by the dynamics [70].

6.4 Outlook on time-resolved experiments

Electron diffraction can resolve atomic structures and the here presented setup provided a time resolution of approximately 60 ps, which allows for the investigation of chemical relevant molecular dynamics as isomerization [7] or protein folding [159]. In order to follow dynamics of single nuclei and electrons within the molecule better time resolution is necessary [160]. In general, shorter electron pulsed could be achieved by RF-compression [117] or by compact electron sources [113, 118–120]. If electron pulses of sub-ps duration are used, velocity mismatch of pump-laser and electron pulse has to be taken into account for gas-phase diffraction experiments. This could be realized by tilted wave-fronts of the laser or an adapted angle between electron and laser pulse propagation direction [161, 162]. A different approach for improved time-resolution employed the streaking technique, which was originally developed for electron pulse duration measurement [158]. A long electron pulse scatters off the molecules. It is then deflected by switched electric fields. The

time evolution can then be mapped on to the position on the detector, which provides time-resolved diffraction data [163].
Time-resolved experiments will enhance the importance of signal-to-noise. If a dynamical process is triggered, not all of the molecules follow the same structure-evolution with time. Therefore, statistics would have to be improved or quantum control mechanisms could be applied to follow well-defined transformation paths [164].

6.5 Conclusion

Samples of gas-phase molecules were state-selected and aligned as preparation for imaging experiments (chapter 3). Due to this control the information retrieved from electron diffraction data would be increased (chapter 2). An electron source (chapter 4) was developed allowing for a suitable signal-to-noise ratio for electron diffraction experiments on controlled DIBN molecules. Characterization of the electron beam properties like spot size and coherence was performed by experiments and electron trajectory simulations. Diffraction data of gaseous test samples illustrated the agreement between diffraction simulation and experiment. First steps toward electron diffraction off aligned DIBN were undertaken including alignment and deflection of DIBN, spatial overlap monitoring and first attempts at recording diffraction data off DIBN (chapter 5).
The provided simulations and measurements were used to discuss improvements that address overlap, coherence, signal-to-noise ratio and adaptations of the modeling employed for simulation. Moreover, setup alterations were suggested for meeting the requirements of time-resolved electron diffraction experiments on controlled molecules (chapter 6).
The discussed developments aimed at the investigation of molecular structure and its changes with time. Electron diffraction is sensitive to both nuclei and electron distribution within the molecule due to Coulomb interaction. Alternative methods for molecular imaging probe different aspects of the dynamics. X-ray diffraction is sensitive the electron distributions of a molecule [36]. Probing the photo-electrons after ionization can also provide information on molecular structure [12, 126, 165]. The control mechanisms discussed within this thesis enhance the information gained from all these imaging techniques [12, 36]. In order to retrieve a complete picture of a chosen molecular dynamics one could combine the gained information. On the one hand the information retrieved by one technique could assist the other method's analysis. On the other hand different aspects of the physics are probed and the gained information would complement each other.
From studying molecular dynamics within in a well-controlled sample, as it was approached in this work, one could unravel the fundamental processes that occur in molecular systems. One would then approach larger systems and add complexity by adapting the environment. Eventually the physical understanding that started from a quantum level in small molecular systems would meet the bio-chemical insight that scientists have achieved for larger systems. The combined knowledge would allow for controlling dynamics and design of molecules and materials. Again, human kind will have imaged and controlled nature to learn from it.

Bibliography

[1] R. Croteau, E. Davis, K. Ringer, and M. Wildung, Naturwissenschaften **92**, 563 (2005).

[2] L. Calabrese and A. B. Fleischer, Am J Med **108**, 487 (2000).

[3] G. H. Krause and E. Weis, Annu. Rev. Plant Physiol. Plant Mol. Biol. **42**, 313 (1991).

[4] G. D. Scholes, G. R. Fleming, A. Olaya-Castro, and R. van Grondelle, Nat. Chem. **3**, 763 (2011).

[5] S. W. Hell, Science **316**, 1483 (2007).

[6] K. Takayanagi, J. Vac. Sci. Technol. A **3**, 1502 (1985).

[7] B. C. Dian, J. R. Clarkson, and T. S. Zwier, Science **303**, 1169 (2004).

[8] J. M. Bakker, L. M. Aleese, G. Meijer, and G. von Helden, Phys. Rev. Lett. **91**, 203003 (2003).

[9] D. J. Flannigan and A. H. Zewail, Acc. Chem. Res. **45**, 1828 (2012).

[10] M. Meckel, D. Comtois, D. Zeidler, A. Staudte, D. Pavicic, H. C. Bandulet, H. Pepin, J. C. Kieffer, R. Dörner, D. M. Villeneuve, and P. B. Corkum, Science **320**, 1478 (2008).

[11] O. Geßner, A. M. D. Lee, J. P. Shaffer, H. Reisler, S. V. Levchenko, A. I. Krylov, J. G. Underwood, H. Shi, A. L. L. East, D. M. Wardlaw, E. t. H. Chrysostom, C. C. Hayden, and A. Stolow, Science **311**, 219 (2006).

[12] L. Holmegaard, J. L. Hansen, L. Kalhøj, S. L. Kragh, H. Stapelfeldt, F. Filsinger, J. Küpper, G. Meijer, D. Dimitrovski, M. Abu-samha, C. P. J. Martiny, and L. B. Madsen, Nat. Phys. **6**, 428 (2010), arXiv:1003.4634 [physics] .

[13] J. Hansen, H. Stapelfeldt, D. Dimitrovski, M. Abu-Samha, C. Martiny, and L. Madsen, Phys. Rev. Lett. **106**, 073001 (2011).

[14] L. Germer, Phys. Rev. **56**, 58 (1939).

[15] K. Lonsdale, Proc. Royal Soc. London A **123**, 494 (1929).

[16] A. Yonath, Annu. Rev. Biophys. Biomol. Struct. **31**, 257 (2002).

[17] I. Hargittai and M. Hargittai, *Stereochemical Applications of Gas-Phase Electron Diffraction* (VCH Verlagsgesellschaft, Weinheim, Germany, 1988).

[18] J. C. Williamson, J. M. Cao, H. Ihee, H. Frey, and A. H. Zewail, Nature **386**, 159 (1997).

[19] H. Ihee, V. Lobastov, U. Gomez, B. Goodson, R. Srinivasan, C. Ruan, and A. H. Zewail, Science **291**, 458 (2001).

[20] B. J. Siwick, J. R. Dwyer, R. E. Jordan, and R. J. D. Miller, Science **302**, 1382 (2003).

[21] H. N. Chapman, A. Barty, M. J. Bogan, S. Boutet, S. Frank, S. P. Hau-Riege, S. Marchesini, B. W. Woods, S. Bajt, W. H. Benner, L. W. A., E. Plönjes, M. Kuhlmann, R. Treusch, S. Düsterer, T. Tschentscher, J. R. Schneider, E. Spiller, T. Möller, C. Bostedt, M. Hoener, D. A. Shapiro, K. O. Hodgson, D. van der Spoel, F. Burmeister, M. Bergh, C. Caleman, G. Huldt, M. M. Seibert, F. R. N. C. Maia, R. W. Lee, A. Szöke, N. Timneanu, and J. Hajdu, Nat. Phys. **2**, 839 (2006).

[22] J. C. H. Spence, U. Weierstall, and H. N. Chapman, Rep. Prog. Phys. **75**, 102601 (2012).

[23] A. Barty, J. Küpper, and H. N. Chapman, Annu. Rev. Phys. Chem. **64**, 415 (2013).

[24] R. J. D. Miller, R. Ernstorfer, M. Harb, M. Gao, C. T. Hebeisen, H. Jean-Ruel, C. Lu, G. Moriena, and G. Sciaini, Acta Crystallogr A **66**, 137 (2010).

[25] M. Bargheer, N. Zhavoronkov, Y. Gritsai, J. C. Woo, D. S. Kim, M. Woerner, and T. Elsaesser, Science **306**, 1771 (2004).

[26] S. Manz, A. Casandruc, D. Zhang, Y. Zhong, R. A. Loch, A. Marx, T. Hasegawa, L. C. Liu, S. Bayesteh, H. Delsim-Hashemi, M. Hoffmann, M. Felber, M. Hachmann, F. Mayet, J. Hirscht, S. Keskin, M. Hada, S. W. Epp, K. Flöttmann, and R. J. D. Miller, Faraday Disc. **177**, 467 (2015).

[27] S. P. Weathersby, G. Brown, M. Centurion, T. F. Chase, R. Coffee, J. Corbett, J. P. Eichner, J. C. Frisch, A. R. Fry, M. Gühr, N. Hartmann, C. Hast, R. Hettel, R. K. Jobe, E. N. Jongewaard, J. R. Lewandowski, R. K. Li, A. M. Lindenberg, I. Makasyuk, J. E. May, D. McCormick, M. N. Nguyen, A. H. Reid, X. Shen, K. Sokolowski-Tinten, T. Vecchione, S. L. Vetter, J. Wu, J. Yang, H. A. Dürr, and X. J. Wang, Review of Scientific Instruments **86**, 073702 (2015).

[28] S. Kneip, C. McGuffey, J. L. Martins, S. F. Martins, C. Bellei, V. Chvykov, F. Dollar, R. Fonseca, C. Huntington, G. Kalintchenko, A. Maksimchuk, S. P. D. Mangles, T. Matsuoka, S. R. Nagel, C. A. J. Palmer, J. Schreiber, K. T. Phuoc, A. G. R. Thomas, V. Yanovsky, L. O. Silva, K. Krushelnick, and Z. Najmudin, Nat. Phys. **6**, 980 (2011).

[29] M. M. Seibert, T. Ekeberg, F. R. N. C. Maia, M. Svenda, J. Andreasson, O. Jönsson, D. Odić, B. Iwan, A. Rocker, D. Westphal, M. Hantke, D. P. Deponte, A. Barty, J. Schulz, L. Gumprecht, N. Coppola, A. Aquila, M. Liang, T. A. White, A. Martin, C. Caleman, S. Stern, C. Abergel, V. Seltzer, J.-M. Claverie, C. Bostedt, J. D. Bozek, S. Boutet, A. A. Miahnahri, M. Messerschmidt, J. Krzywinski, G. Williams, K. O. Hodgson, M. J. Bogan, C. Y. Hampton, R. G. Sierra, D. Starodub, I. Andersson, S. Bajt, M. Barthelmess, J. C. H. Spence, P. Fromme, U. Weierstall, R. Kirian, M. Hunter, R. B. Doak, S. Marchesini, S. P. Hau-Riege, M. Frank, R. L. Shoeman, L. Lomb, S. W. Epp, R. Hartmann, D. Rolles, A. Rudenko, C. Schmidt, L. Foucar, N. Kimmel, P. Holl, B. Rudek, B. Erk, A. Hömke, C. Reich, D. Pietschner, G. Weidenspointner, L. Strüder, G. Hauser, H. Gorke, J. Ullrich, I. Schlichting, S. Herrmann, G. Schaller, F. Schopper, H. Soltau, K.-U. Kühnel, R. Andritschke, C.-D. Schröter, F. Krasniqi, M. Bott, S. Schorb, D. Rupp, M. Adolph, T. Gorkhover, H. Hirsemann, G. Potdevin, H. Graafsma, B. Nilsson, H. N. Chapman, and J. Hajdu, Nature **470**, 78 (2011).

[30] H. N. Chapman, A. Barty, S. Marchesini, A. Noy, S. P. Hau-Riege, C. Cui, M. R. Howells, R. Rosen, H. He, J. C. H. Spence, U. Weierstall, T. Beetz, C. Jacobsen, and D. Shapiro, J. Opt. Soc. Am. A **23**, 1179 (2006).

[31] K. Ayyer, O. M. Yefanov, D. Oberthür, S. Roy-Chowdhury, L. Galli, V. Mariani, S. Basu, J. Coe, C. E. Conrad, R. Fromme, A. Schaffer, K. Dörner, D. James, C. Kupitz, M. Metz, G. Nelson, P. L. Xavier, K. R. Beyerlein, M. Schmidt, I. Sarrou, J. C. H. Spence, U. Weierstall, T. A. White, J.-H. Yang, Y. Zhao, M. Liang, A. Aquila, M. S. Hunter, J. S. Robinson, J. E. Koglin, S. Boutet, P. Fromme, A. Barty, and H. N. Chapman, Nature **530**, 202 (2016).

[32] S. Ryu, R. Stratt, and P. Weber, J. Phys. Chem. A **107**, 6622 (2003).

[33] J. C. H. Spence and R. B. Doak, Phys. Rev. Lett. **92**, 198102 (2004).

[34] S. Pabst, P. J. Ho, and R. Santra, Phys. Rev. A **81**, 043425 (2010).

[35] F. Filsinger, G. Meijer, H. Stapelfeldt, H. Chapman, and J. Küpper, Phys. Chem. Chem. Phys. **13**, 2076 (2011).

[36] J. Küpper, S. Stern, L. Holmegaard, F. Filsinger, A. Rouzée, A. Rudenko, P. Johnsson, A. V. Martin, M. Adolph, A. Aquila, S. Bajt, A. Barty, C. Bostedt, J. Bozek, C. Caleman, R. Coffee, N. Coppola, T. Delmas, S. Epp, B. Erk, L. Foucar, T. Gorkhover,

L. Gumprecht, A. Hartmann, R. Hartmann, G. Hauser, P. Holl, A. Hömke, N. Kimmel, F. Krasniqi, K.-U. Kühnel, J. Maurer, M. Messerschmidt, R. Moshammer, C. Reich, B. Rudek, R. Santra, I. Schlichting, C. Schmidt, S. Schorb, J. Schulz, H. Soltau, J. C. H. Spence, D. Starodub, L. Strüder, J. Thøgersen, M. J. J. Vrakking, G. Weidenspointner, T. A. White, C. Wunderer, G. Meijer, J. Ullrich, H. Stapelfeldt, D. Rolles, and H. N. Chapman, Phys. Rev. Lett. **112**, 083002 (2014), arXiv:1307.4577 [physics] .

[37] S. Stern, L. Holmegaard, F. Filsinger, A. Rouzee, A. Rudenko, P. Johnsson, A. V. Martin, A. Barty, C. Bostedt, J. Bozek, R. Coffee, S. Epp, B. Erk, L. Foucar, R. Hartmann, N. Kimmel, K.-U. Kühnel, J. Maurer, M. Messerschmidt, B. Rudek, D. Starodub, J. Thøgersen, G. Weidenspointner, T. A. White, H. Stapelfeldt, D. Rolles, H. N. Chapman, and J. Küpper, Faraday Disc. **171**, 393 (2014), arXiv:1403.2553 [physics] .

[38] C. J. Hensley, J. Yang, and M. Centurion, Phys. Rev. Lett. **109**, 133202 (2012).

[39] J. Yang, V. Makhija, V. Kumarappan, and M. Centurion, Struct. Dyn. **1**, 044101 (2014).

[40] O. Stern, Z. Phys. **39**, 751 (1926).

[41] J. H. Nielsen, P. Simesen, C. Z. Bisgaard, H. Stapelfeldt, F. Filsinger, B. Friedrich, G. Meijer, and J. Küpper, Phys. Chem. Chem. Phys. **13**, 18971 (2011), arXiv:1105.2413 [physics] .

[42] S. Trippel, T. Mullins, N. L. M. Müller, J. S. Kienitz, J. J. Omiste, H. Stapelfeldt, R. González-Férez, and J. Küpper, Phys. Rev. A **89**, 051401(R) (2014), arXiv:1401.6897 [quant-ph] .

[43] D. A. Horke, Y.-P. Chang, K. Długołęcki, and J. Küpper, Angew. Chem. Int. Ed. **53**, 11965 (2014), arXiv:1407.2056 [physics] .

[44] F. Filsinger, J. Küpper, G. Meijer, J. L. Hansen, J. Maurer, J. H. Nielsen, L. Holmegaard, and H. Stapelfeldt, Angew. Chem. Int. Ed. **48**, 6900 (2009).

[45] T. Kierspel, D. A. Horke, Y.-P. Chang, and J. Küpper, Chem. Phys. Lett. **591**, 130 (2014), arXiv:1312.4417 [physics] .

[46] F. Filsinger, U. Erlekam, G. von Helden, J. Küpper, and G. Meijer, Phys. Rev. Lett. **100**, 133003 (2008), arXiv:0802.2795 [physics] .

[47] S. Trippel, Y.-P. Chang, S. Stern, T. Mullins, L. Holmegaard, and J. Küpper, Phys. Rev. A **86**, 033202 (2012), arXiv:1208.4935 [physics] .

[48] Y.-P. Chang, D. Horke, S. Trippel, and J. Küpper, Int. Rev. Phys. Chem. **34**, 557 (2015), arXiv:1505.05632 [physics] .

[49] H. Stapelfeldt and T. Seideman, Rev. Mod. Phys. **75**, 543 (2003).

[50] L. Holmegaard, J. H. Nielsen, I. Nevo, H. Stapelfeldt, F. Filsinger, J. Küpper, and G. Meijer, Phys. Rev. Lett. **102**, 023001 (2009), arXiv:0810.2307 [physics.chem-ph] .

[51] O. Ghafur, A. Rouzee, A. Gijsbertsen, W. K. Siu, S. Stolte, and M. J. J. Vrakking, Nat. Phys. **5**, 289 (2009).

[52] P. M. Kraus, D. Baykusheva, and H. J. Wörner, Phys. Rev. Lett. **113**, 023001 (2014), arXiv:1311.3923 [physics.chem-ph] .

[53] S. Trippel, T. Mullins, N. L. M. Müller, J. S. Kienitz, R. González-Férez, and J. Küpper, Phys. Rev. Lett. **114**, 103003 (2015), arXiv:1409.2836 [physics] .

[54] V. Kumarappan, C. Z. Bisgaard, S. S. Viftrup, L. Holmegaard, and H. Stapelfeldt, J. Chem. Phys. **125**, 194309 (2006).

[55] A. A. Ischenko and S. A. Aseyev, *Time-Resolved Electron Diffraction: For Chemistry, Biology and Materials Science*, Advances in Imaging and Electron Physics, Vol. 184 (Elsevier, Amsterdam, 2014).

[56] J. Sakurai, *Modern Quantum Mechanics* (Addison-Wesley Publishing Company, Reading, Massachusetts, 1994).

[57] T.-Y. Wu and T. Ohmura, *Quantum Theory of Scattering* (Prentice-Hall Inc., 1962).

[58] J. Ewbank, L. Schäfer, and A. Ischenko, J. Mol. Struct. **524**, 1 (2000).

[59] R. Glauber and V. Schomaker, Phys. Rev. **89**, 667 (1953).

[60] D. Van Dyck, H. Lichte, and J. Spence, Ultramicroscopy **81**, 187 (2000).

[61] F. Zhou, Ultramicroscopy **92**, 293 (2002).

[62] R. A. Bonham and H. L. Cox, J. Chem. Phys. **47**, 3508 (1967).

[63] V. Schomaker and R. Glauber, Nature **170**, 290 (1952).

[64] A. Yates, Chem. Phys. Lett. **6**, 49 (1970).

[65] L. S. Bartell and R. M. J. Gavin, J. Am. Chem. Soc. **86**, 3493 (1964).

[66] C. Tavard and R. A. Bonham, J. Chem. Phys. **50**, 1736 (1969).

[67] S. Stern, *Controlled Molecules for X-ray Diffraction Experiments at Free-Electron Lasers*, Dissertation, Universität Hamburg, Hamburg, Germany (2013).

[68] D. Peng, Ren and Whelan, Acta Cryst. A **52**, 257 (1996).

[69] Ross, Fink, Hilderbrandt, Wang, and Smith, Int. Tables for Cryst. **C**, 389 (2006).

[70] H. Ihee, B.M. Goodson, R. Srinivasan, V.A. Lobastov, A.H. Zewail, J. Phys. Chem. A **106**, 4087 (2002).

[71] J. Yang and M. Centurion, Struct. Chem. **26**, 1513 (2015).

[72] F. Filsinger, J. Küpper, G. Meijer, L. Holmegaard, J. H. Nielsen, I. Nevo, J. L. Hansen, and H. Stapelfeldt, J. Chem. Phys. **131**, 064309 (2009), arXiv:0903.5413 [physics] .

[73] B. Friedrich and D. Herschbach, Phys. Rev. Lett. **74**, 4623 (1995).

[74] B. Friedrich and D. R. Herschbach, Nature **353**, 412 (1991).

[75] B. Friedrich and D. Herschbach, J. Chem. Phys. **111**, 6157 (1999).

[76] H. J. Loesch and A. Remscheid, J. Chem. Phys. **93**, 4779 (1990).

[77] J. J. Larsen, K. Hald, N. Bjerre, H. Stapelfeldt, and T. Seideman, Phys. Rev. Lett. **85**, 2470 (2000).

[78] I. Nevo, L. Holmegaard, J. H. Nielsen, J. L. Hansen, H. Stapelfeldt, F. Filsinger, G. Meijer, and J. Küpper, Phys. Chem. Chem. Phys. **11**, 9912 (2009), arXiv:0906.2971 [physics] .

[79] J. Bulthuis, J. Möller, and H. J. Loesch, J. Phys. Chem. A **101**, 7684 (1997).

[80] J. H. Nielsen, H. Stapelfeldt, J. Küpper, B. Friedrich, J. J. Omiste, and R. González-Férez, Phys. Rev. Lett. **108**, 193001 (2012), arXiv:1204.2685 [physics.chem-ph] .

[81] S. Putzke, F. Filsinger, H. Haak, J. Küpper, and G. Meijer, Phys. Chem. Chem. Phys. **13**, 18962 (2011), arXiv:1103.5080 [physics] .

[82] H. Kallmann and F. Reiche, Z. Phys. **6**, 352 (1921).

[83] N. F. Ramsey, *Molecular Beams*, The International Series of Monographs on Physics (Oxford University Press, London, GB, 1956) reprinted in *Oxford Classic Texts in the Physical Sciences* (2005).

[84] Y.-P. Chang, F. Filsinger, B. Sartakov, and J. Küpper, Comp. Phys. Comm. **185**, 339 (2014), arXiv:1308.4076 [physics] .

[85] A. T. J. B. Eppink and D. H. Parker, Rev. Sci. Instrum. **68**, 3477 (1997).

[86] M. N. R. Ashfold, N. H. Nahler, A. J. Orr-Ewing, O. P. J. Vieuxmaire, R. L. Toomes, T. N. Kitsopoulos, I. A. Garcia, D. A. Chestakov, S.-M. Wu, and D. H. Parker, Phys. Chem. Chem. Phys. **8**, 26 (2006).

[87] A. I. Chichinin, K. H. Gericke, S. Kauczok, and C. Maul, Int. Rev. Phys. Chem. **28**, 607 (2009).

[88] M. Stei, J. von Vangerow, R. Otto, A. H. Kelkar, E. Carrascosa, T. Best, and R. Wester, J. Chem. Phys. **138**, 214201 (2013).

[89] H. Stapelfeldt, E. Constant, and P. B. Corkum, Phys. Rev. Lett. **74**, 3780 (1995).

[90] P. R. Brooks, Science **193**, 11 (1976).

[91] B. Friedrich and D. Herschbach, J. Phys. Chem. A **103**, 10280 (1999).

[92] P. Reckenthaeler, M. Centurion, W. Fuss, S. A. Trushin, F. Krausz, and E. E. Fill, Phys. Rev. Lett. **102**, 213001 (2009).

[93] F. Krasniqi, B. Najjari, L. Strüder, D. Rolles, A. Voitkiv, and J. Ullrich, Phys. Rev. A **81**, 033411 (2010).

[94] T. Horio and T. Suzuki, Rev. Sci. Instrum. **80**, 013706 (2009).

[95] X. Ren, V. Makhija, and V. Kumarappan, Phys. Rev. A **85**, 033405 (2012).

[96] D. Irimia, D. Dobrikov, R. Kortekaas, H. Voet, D. A. van den Ende, W. A. Groen, and M. H. M. Janssen, Rev. Sci. Instrum. **80**, 113303 (2009).

[97] E. R. Peterson, C. Buth, D. A. Arms, R. W. Dunford, E. P. Kanter, B. Krässig, E. C. Landahl, S. T. Pratt, R. Santra, S. H. Southworth, and L. Young, Appl. Phys. Lett. **92**, 094106 (2008).

[98] E. Peronne, M. Poulsen, C. Bisgaard, H. Stapelfeldt, and T. Seideman, Phys. Rev. Lett. **91**, 04300 (2003).

[99] A. Rouzee, F. Kelkensberg, W. K. Siu, G. Gademann, R. R. Lucchese, and M. J. J. Vrakking, J. Phys. B **45**, 074016 (2012).

[100] U. Even, J. Jortner, D. Noy, N. Lavie, and N. Cossart-Magos, J. Chem. Phys. **112**, 8068 (2000).

[101] J. J. Larsen, H. Sakai, C. P. Safvan, I. Wendt-Larsen, and H. Stapelfeldt, J. Chem. Phys. **111**, 7774 (1999).

[102] M. D. Poulsen, E. Peronne, H. Stapelfeldt, C. Z. Bisgaard, S. Viftrup, E. Hamilton, and T. Seideman, J. Chem. Phys. **121**, 783 (2004).

[103] O. Dorosh, E. Białkowska-Jaworska, Z. Kisiel, and L. Pszczółkowski, J. Mol. Spec. **246**, 228 (2007).

[104] A. Rouzee, A. Gijsbertsen, O. Ghafur, O. M. Shir, T. Baeck, S. Stolte, and M. J. J. Vrakking, New J. Phys. **11**, 105040 (2009).

[105] A. Landers, T. Weber, I. Ali, A. Cassimi, M. Hattass, O. Jagutzki, A. Nauert, T. Osipov, A. Staudte, M. H. Prior, H. Schmidt-Böcking, C. L. Cocke, and R. Dörner, Phys. Rev. Lett. **87**, 013002 (2001).

[106] R. Velotta, N. Hay, M. Mason, M. Castillejo, and J. Marangos, Phys. Rev. Lett. **87**, 183901 (2001).

[107] A. I. Kuleff and L. S. Cederbaum, Chem. Phys. **338**, 320 (2007).

[108] A. Einstein, Ann. Phys. **322**, 132 (1905).

[109] D. H. Dowell and J. F. Schmerge, Phys. Rev. ST Accel. Beams **12**, 074201 (2009).

[110] C. N. Berglund and W. E. Spicer, Phys. Rev. **136**, A1030 (1964).

[111] J. H. Bechtel, W. Lee Smith, and N. Bloembergen, Phys. Rev. B **15**, 4557 (1977).

[112] P. Musumeci, L. Cultrera, M. Ferrario, D. Filippetto, G. Gatti, M. S. Gutierrez, J. T. Moody, N. Moore, J. B. Rosenzweig, C. M. Scoby, G. Travish, and C. Vicario, Phys. Rev. Lett. **104**, 084801 (2010).

[113] G. Sciaini and R. J. D. Miller, Rep. Prog. Phys. **74**, 096101 (2011).

[114] T. van Oudheusden, E. F. de Jong, W. P. E. M. van der Geer, Op 't Root, O. J. Luiten, and B. J. Siwick, J. Appl. Phys. **102**, 093501 (2007).

[115] A. M. Michalik, E. Y. Sherman, and J. E. Sipe, J. Appl. Phys. **104**, 054905 (2008).

[116] K. L. Jensen, J. Lebowitz, Y. Y. Lau, and J. Luginsland, J. Appl. Phys. **111**, 054917 (2012).

[117] T. van Oudheusden, P. L. E. M. Pasmans, S. B. van der Geer, M. J. de Loos, M. J. van der Wiel, and O. J. Luiten, Phys. Rev. Lett. **105**, 264801 (2010).

[118] P. Musumeci, J. T. Moody, C. M. Scoby, M. S. Gutierrez, H. A. Bender, and N. S. Wilcox, Rev. Sci. Instrum. **81**, 013306 (2010).

[119] M. S. Robinson, P. D. Lane, and D. A. Wann, Rev. Sci. Instrum. **86**, 013109 (2015).

[120] C. Gerbig, A. Senftleben, S. Morgenstern, C. Sarpe, and T. Baumert, New J. Phys. **17**, 043050 (2015).

[121] S. Lahme, C. Kealhofer, F. Krausz, and P. Baum, Struct. Dyn. **1**, 034303 (2014).

[122] M. W. van Mourik, W. J. Engelen, E. J. D. Vredenbregt, and O. J. Luiten, Struct. Dyn. **1**, 034302 (2014).

[123] A. J. McCulloch, D. V. Sheludko, S. D. Saliba, S. C. Bell, M. Junker, K. A. Nugent, and R. E. Scholten, Nat. Phys. **7**, 785 (2011).

[124] M. Gulde, S. Schweda, G. Storeck, M. Maiti, H. K. Yu, A. M. Wodtke, S. Schäfer, and C. Ropers, Science **345**, 200 (2014).

[125] T. Zuo, A. D. Bandrauk, and P. B. Corkum, Chem. Phys. Lett. **259**, 313 (1996).

[126] C. I. Blaga, J. Xu, A. D. DiChiara, E. Sistrunk, K. Zhang, P. Agostini, T. A. Miller, L. F. DiMauro, and C. D. Lin, Nature **483**, 194 (2012).

[127] Y.-P. Chang, K. Długołęcki, J. Küpper, D. Rösch, D. Wild, and S. Willitsch, Science **342**, 98 (2013), arXiv:1308.6538 [physics] .

[128] S. Trippel, T. Mullins, N. L. M. Müller, J. S. Kienitz, K. Długołęcki, and J. Küpper, Mol. Phys. **111**, 1738 (2013), arXiv:1301.1826 [physics.atom-ph] .

[129] A. R. Bainbridge and W. A. Bryan, New J. Phys. **16**, 103031 (2014).

[130] J. R. Maldonado, P. Pianetta, D. H. Dowell, J. Corbett, S. Park, J. Schmerge, A. Trautwein, and W. Clay, Appl. Phys. Lett. **101**, 231103 (2012).

[131] K. Floettmann, "ASTRA, a space charge tracking algorithm (software package)," (1997), `http://www.desy.de/~mpyflo/`.

[132] S. Flügge, *Rechenmethoden der Elektrodynamik*, Aufgaben mit Lösungen (Springer Verlag, 1986).

[133] F. Fu, S. Liu, P. Zhu, D. Xiang, J. Zhang, and J. Cao, Rev. Sci. Instrum. **85**, 083701 (2014).

[134] Photonis, Information provided by company Photonis on their MCP detectors (2015).

[135] B. J. Siwick, J. R. Dwyer, R. E. Jordan, and R. J. D. Miller, J. Appl. Phys. **92**, 1643 (2002).

[136] G. Scoles, *Atomic and Molecular Beam Methods* (Oxford University Press, 1988).

[137] U. Even, Advances in Chemistry **2014**, Article ID 636042 (2014).

[138] E. L. Cussler, *Diffusion: Mass Transfer in Fluid Systems* (Cambridge University Press, 2009).

[139] PfeifferVacuum, "The vacuum technology book," (2008).

[140] B. Fultz and J. M. Howe, *Transmission electron microscopy and diffractometry of materials* (Springer Science and Business Media, 2012).

[141] A. A. Ischenko, J. D. Ewbank, and L. Schäfer, J. Chem. Phys. **98**, 4287 (1994).

[142] M. Abramowitz and I. Stegun, *Handbook of Mathematical Functions* (Dover Publ. Inc. New York, 1965).

[143] W. Lotz, Z. Phys. **206**, 205 (1967).

[144] S. Trippel, private communication, to be published (2016).

[145] J. Clark, X. Huang, R. Harder, and I. Robinson, Nat. Commun. **3** (2012), 10.1038/ncomms1994.

[146] M. Dantus, B. K. Scott, J. C. Williamson, and A. H. Zewail, J. Chem. Phys. **98**, 2782 (1994).

[147] B. J. Siwick, A. A. Green, C. T. Hebeisen, and R. J. D. Miller, Opt. Lett. **30**, 1057 (2005).

[148] J. Yang, J. Beck, C. J. Uiterwaal, and M. Centurion, Nat. Commun. **6**, 8172 (2010).

[149] J. S. Kienitz, Talk at CMI workshop Goslar 2016 and private communication with J. S. Kienitz (2016).

[150] D. Wytrykus, M. Centurion, P. Reckenthaeler, F. Krausz, A. Apolonski, and E. Fill, Appl. Phys. B **96**, 094301309 (2009).

[151] M. Gupta and D. Herschbach, J. Phys. Chem. A **103**, 10670 (1999).

[152] S. E. Maxwell, N. Brahms, R. deCarvalho, D. R. Glenn, J. S. Helton, S. V. Nguyen, D. Patterson, J. Petricka, D. DeMille, and J. M. Doyle, Phys. Rev. Lett. **95**, 173201 (2005).

[153] N. R. Hutzler, H. I. Lu, and J. M. Doyle, Chem. Rev. **112**, 4803 (2012).

[154] B. Deppe, G. Huber, C. Kränkel, and J. Küpper, Opt. Exp. **23**, 28491 (2015), arXiv:1508.03489 [physics] .

[155] R. Srinivasan, V. A. Lobastov, C.-Y. Ruan, and A. H. Zewail, Helv. Chim. Acta. **86**, 1763 (2003).

[156] F. O. Kirchner, S. Lahme, F. Krausz, and P. Baum, New Journal of Physics **15**, 063021 (2013).

[157] R. K. Li, K. G. Roberts, C. M. Scoby, H. To, and P. Musumeci, Phys. Rev. ST Accel. Beams **15**, 090702 (2012).

[158] G. H. Kassier, K. Haupt, N. Erasmus, E. G. Rohwer, H. M. von Bergmann, H. Schwoerer, S. M. M. Coelho, and F. D. Auret, Rev. Sci. Instrum. **81**, 105103 (2010).

[159] A. R. Fersht, PNAS **99**, 14122 (2002).

[160] M. Centurion, J. Phys. B **49**, 062002 (2016).

[161] J. C. Williamson and A. H. Zewail, Chem. Phys. Lett. **209**, 10 (1993).

[162] P. Baum and A. H. Zewail, PNAS **103**, 16105 (2006).

[163] M. Eichberger, N. Erasmus, K. Haupt, G. Kassier, A. von Flotow, J. Demsar, and H. Schwoerer, Appl. Phys. Lett. **102**, 121106 (2013).

[164] H. Rabitz, R. de Vivie-Riedle, M. Motzkus, and K. Kompa, Science **288**, 824 (2000).

[165] R. Boll, D. Anielski, C. Bostedt, J. D. Bozek, L. Christensen, R. Coffee, S. De, P. Decleva, S. W. Epp, B. Erk, L. Foucar, F. Krasniqi, J. Küpper, A. Rouzée, B. Rudek, A. Rudenko, S. Schorb, H. Stapelfeldt, M. Stener, S. Stern, S. Techert, S. Trippel, M. J. J. Vrakking, J. Ullrich, and D. Rolles, Phys. Rev. A **88**, 061402(R) (2013).

Acknowledgements

Within these years of my doctoral work, I enjoyed increasing my knowledge and broadening my horizon. I would like to deeply thank my supervisor, Jochen Küpper, for the opportunity to perform my research work in the Controlled Molecule Imaging group, in such an inspiring environment and with far-reaching possibilities. I am very grateful for Jochen's scientific advise, guidance and the motivating discussions. Moreover, I highly appreciated to learn from him about various other aspects of the work as a scientist.
I would like to thank by second supervisor, Henry Chapman. I treasured his advise and his course within the curriculum of the IMPRS UFAST, which gave me a good point to start my journey in the world of diffraction.
My gratitude goes to Sebastian Trippel, who supervised me at project planning, in the lab, during data analysis and writing. I am very thankful for all of his help and the wide scope of knowledge that he shared with me, reaching from broad experience concerning experiments to a detailed understanding of theory.
The experimental part of this work would not have been possible without Karol Długołęcki. I thank him and the other technicians at CMI and in the Coherent Imaging Division for their great support.
I would like to thank Jens Kienitz for everything. Wether long hours in the lab, fights with LabView, corrections of my thesis or just having coffee. It was amazing that Jens always took the time, when I needed assistance or a discussion partner.
Then I would like to acknowledge all the other students and postdocs who contributed to this work: Terry Mullins, Joss Wiese, Frederik Lauber and Florian Friedrich. A big thank you to Ruth Livingstone for taking over the project and for her comments on my thesis.
Moreover, my gratitude extends to my co-strugglers in diffractive imaging. I would like to thank Stephan Stern for the discussions on diffraction and for CMIdiffract, and Thomas Kierspel for comments on my thesis and all the insight that I gained from discussions with him.
I would like to thank Barbora Vabovič and Irmtraud Kleine for their amazing support.
The team CMI consisted of great people to work with - no matter if 6 or of 30. I thank all of them for pondering science, liters of coffee, afterwork activities, and for being who they are.
This great atmosphere was not only restricted to the CMI group. I felt at home at DESY and in CFEL, within the IMPRS and PHGS. As representatives, I would like to thank Ralf Koehn, Anja Bleidorn, Sonia Utermann, Julia Quante, Stefanie Tepass, the Coherent

Imaging division, the group of Melanie Schnell and the former group of Daniel Rolles.
I would like to acknowledge financial support by the Joachim Herz Stiftung. The value of all the possibilities that were given to me was immense and I thank Eva Ackermann and Jörg Maxton-Küchenmeister for their help.
A big thank you to DESY infrastructure and to the people within it: In particular, Sven Lederer, Ingo Hansen, and Hans-Hinrich Sahling for advise about the photocathode design, Klaus Floettmann for help with ASTRA simulations and Horst Zink and his team in the electronic workshop for their support.
I would like to thank Dwayne Miller, Stuart Hayes, German Sciaini, Kostyantyn Pichugin, Julian Hirscht, Stephanie Manz, Albert Casandruc, Daniel Badali and Kalid Siddiqui for discussions regarding electron diffraction experiments and Masaki Hada for the preparation of the aluminum sample.
I am very grateful for the opportunity provided by Martin Centurion to work with him and his team for two weeks and for the discussions, in which many of my questions about experimental setup and electron diffraction theory were answered. Also, I would like to thank Anatoly Ischenko for his response regarding electron diffraction theory.
Thanks to Clemens Wieck, Matthias Schlaffer and Özgür Sahin, for the great time we had as JHS fellows and with organizing READi. For their amazing support and for sharing the pain and the joy, I would like to thank: Stephanie Besztejan, Nicole Teschmit, Frederike Ahr, Alessandra Picchiotti, Ling Ren, Anne-Laure Calendron, Zeinab Eskandarian, Julian Schweizer, Clemens Weninger, Holger Fleckenstein, Rebecca Boll and Jan Slowik.
I am grateful for my family and friends, whose support during my studies and the doctoral thesis was very important to me.
I would like to deeply thank my dearest Julian for all the good words, the everlasting support, the incredible patience and for his interest in natural sciences.
Finally, I thank the whole scientific community. Amazing science is done all around the globe and I was very happy to have had the chance to contribute my little puzzle piece to the huge endeavor – learning from nature.

List of Publications

1. *Electron gun for diffraction experiments off controlled molecules*
   N.L.M. Müller, S. Trippel, K. Długołęcki, J. Küpper
   Journal of physics B **48**(24), 244001 (2015)

2. *Two-State Wave Packet for Strong Field-Free Molecular Orientation*
   S. Trippel, T. Mullins, N.L.M. Müller, J. S. Kienitz, R. Gonzalez-Ferez, J. Küpper
   Physical review letters **114**(10), 103003 (2015)

3. *Imaging Molecular Structure through Femtosecond Photoelectron Diffraction on Aligned and Oriented Gas-Phase Molecules*
   R. Boll, A. Rouzee, M. Adolph, D. Anielski, A. Aquila, S. Bari, C. Bomme, C. Bostedt, J. D. Bozek, H. N. Chapman, L. Christensen, R. Coffee, N. Coppola, S. De, P. Decleva, S. W. Epp, B. Erk, F. Filsinger, L. Foucar, T. Gorkhover, L. Gumprecht, A. Hömke, L. Holmegaard, P. Johnsson, J. S. Kienitz, T. Kierspel, F. Krasniqi, K.-U. Kühnel, J. Maurer, M. Messerschmidt, R. Moshammer, N. L. M. Müller, B. Rudek, E. Savelyev, I. Schlichting, C. Schmidt, F. Scholz, S. Schorb, J. Schulz, J. Seltmann, M. Stener, S. Stern, S. Techert, J. Thøgersen, S. Trippel, J. Viefhaus, M. Vrakking, H. Stapelfeldt, J. Küpper, J. Ullrich, A. Rudenko and D. Rolles
   Faraday discussions **171**, 57 - 80 (2014)

4. *Strongly driven quantum pendulum of the carbonyl sulfide molecule*
   S. Trippel, T. Mullins, N.L.M. Müller, J. S. Kienitz, J. J. Omiste, H. Stapelfeldt, R. Gonzalez Ferez, J. Küpper
   Physical review A **89**(5), 051401 (2014)

5. *Strongly aligned and oriented molecular samples at a kHz repetition rate*
   S. Trippel, T. Mullins, N.L.M. Müller, J. S. Kienitz, K. Długołęcki, J. Küpper
   Molecular physics **111**(12-13), 1738 (2013)